



저작자표시-비영리-변경금지 2.0 대한민국

이용자는 아래의 조건을 따르는 경우에 한하여 자유롭게

- 이 저작물을 복제, 배포, 전송, 전시, 공연 및 방송할 수 있습니다.

다음과 같은 조건을 따라야 합니다:



저작자표시. 귀하는 원저작자를 표시하여야 합니다.



비영리. 귀하는 이 저작물을 영리 목적으로 이용할 수 없습니다.



변경금지. 귀하는 이 저작물을 개작, 변형 또는 가공할 수 없습니다.

- 귀하는, 이 저작물의 재이용이나 배포의 경우, 이 저작물에 적용된 이용허락조건을 명확하게 나타내어야 합니다.
- 저작권자로부터 별도의 허가를 받으면 이러한 조건들은 적용되지 않습니다.

저작권법에 따른 이용자의 권리는 위의 내용에 의하여 영향을 받지 않습니다.

이것은 [이용허락규약\(Legal Code\)](#)을 이해하기 쉽게 요약한 것입니다.

[Disclaimer](#)

Doctoral Dissertation

Protonics of perovskite electrocatalysts for energy
conversion and storage systems

Junyoung Kim

Department of Energy Engineering
(Energy Engineering)

Graduate School of UNIST

2018

Protonics of perovskite electrocatalysts for energy conversion and storage systems

Junyoung Kim

Department of Energy Engineering
(Energy Engineering)

Graduate School of UNIST

Protonics of perovskite electrocatalysts for energy conversion and storage systems

A dissertation
submitted to the Graduate School of UNIST
in partial fulfillment of the
requirements for the degree of
Doctor of Philosophy

Junyoung Kim

05/30/2018

Approved by

Advisor

Guntae Kim

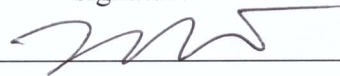
Protonics of perovskite electrocatalysts
for energy conversion and storage systems

Junyoung Kim

This certifies that the dissertation of Junyoung Kim is approved.

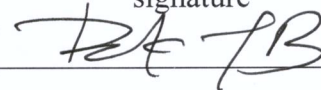
06/15/2018

signature



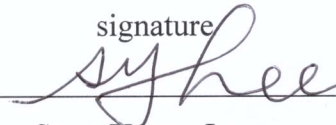
Advisor: Guntae Kim

signature



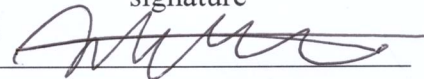
Jong-Beom Baek

signature



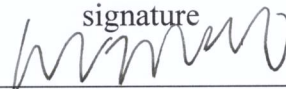
Sang-Young Lee

signature



Hu Young Jeong

signature



Jeeyoung Shin

Abstract

With the exponential growth in energy consumption and with finite fossil fuel resources, environmentally-friendly and sustainable energy conversion and storage (ECS) devices have received great attention from the industrial and academic communities. Ceramic electrochemical cells such as solid oxide fuel cells (SOFCs) and solid oxide electrolysis cells (SOECs), are considered as promising ECS applications because of their high-energy conversion efficiency and low pollutant emission. Solid oxide fuel cells are high-efficiency energy generation devices that convert chemical energy directly into electricity. As a reverse reaction of the fuel cell reaction, the SOEC is a device capable of producing hydrogen without any pollutants by water electrolysis.

Despite these advantages, there are many problems due to the high activation energy of oxygen ion transfer, which requires a very high operating temperature. (e.g., degradation of performance, costly insulation, harsh thermos-cycle environment, slow start-up)

In recent years, protonic ceramic fuel cells (PCFC) using a proton conducting oxide (PCO) as an electrolyte, have been attracting attention to solve the drawbacks of high-temperature operation because the PCOs have shown high ionic conductivity and low activation energy of the H^+ transport compared with the O^{2-} transport. To operate the PCFC efficiently, the PCFC cathode materials should have the property of electrochemical activity not only for O^{2-} and e^- but also for H^+ (so-called triple conducting oxide, TCO). However, due to the difficulties of its characterization, the proton properties of the TCOs are not fully understood yet. In this regard, the characterization of protonics in the TCO is important to understanding applications based on proton conducting oxides.

This paper mainly focuses on the understanding and development of perovskite catalysts for ceramic electrochemical cells. In particular, to solve the problems mentioned above, I have comprehensively investigated the thermodynamic and kinetic properties of the oxygen ion, electron, and proton in the perovskite materials.

I started with basic principles and theory of overall PCFCs and solid oxide ceramic cell in chapter 1, and then my research papers studying solid oxide fuel cell cathode material and protonic ceramic fuel cell for intermediate to low temperature ceramic fuel cells are presented as follows,

1. Effect of Fe Doping on Layered $GdBa_{0.5}Sr_{0.5}Co_{2}O_{5+\delta}$ Perovskite Cathodes for Intermediate Temperature Solid Oxide Fuel Cells
2. Chemically Stable Perovskites as Cathode Materials for Solid Oxide Fuel Cells: La-Doped $Ba_{0.5}Sr_{0.5}Co_{0.8}Fe_{0.2}O_{3-\delta}$
3. Triple-Conducting Layered Perovskites as Cathode Materials for Proton-Conducting Solid Oxide Fuel Cells
4. Hybrid-solid oxide electrolysis cell: A new strategy for efficient hydrogen production
5. The First Observation of Proton Trace in Triple Conducting Oxides: Thermodynamics and Kinetics of Proton

Contents

Chapter 1. Introduction	1
1.1 Motivation and Research Objective	1
1.2. General Introduction	3
1.2.1 The basis of fuel cell and electrolyzer.....	3
1.2.2. Operating principle of ceramic fuel cells	4
1.2.3. Operating principle of ceramic electrolyzer.....	4
1.3. Theoretical Background of ceramic fuel cells.....	5
1.3.1. Performance of ceramic electrochemical cells	5
1.3.2. Thermodynamics of fuel cell	7
1.4. Materials for ceramic electrochemical cells.....	10
1.4.1. Cathode materials for SOFCs.....	10
1.4.2. Cathode materials for PCFCs.....	11
1.4.3. Development of proton conducting oxide for electrolyte material	12
1.4.4. Various type of structures for cathode materials.....	13
Chapter 2. Effect of Fe Doping on Layered $\text{GdBa}_{0.5}\text{Sr}_{0.5}\text{Co}_2\text{O}_{5+\delta}$ Perovskite Cathodes for Intermediate Temperature Solid Oxide Fuel Cells	15
2.1. Introduction.....	15
2.2 Experimental procedure	17
2.3. Results and Discussion.....	19
2.4. Conclusion	29
Chapter 3. Chemically Stable Perovskites as Cathode Materials for Solid Oxide Fuel Cells: La-Doped $\text{Ba}_{0.5}\text{Sr}_{0.5}\text{Co}_{0.8}\text{Fe}_{0.2}\text{O}_{3-\delta}$	30
3.1. Introduction.....	30
3.2. Experimental Section	32
3.3. Results and Discussion.....	34
3.4. Conclusions.....	46
Chapter 4. Triple-Conducting Layered Perovskites as Cathode Materials for Proton-Conducting Solid Oxide Fuel Cells	47
4.1. Introduction.....	47
4.2. Experimental Section	51
4.3. Results and Discussion.....	53
4.4. Conclusion	58

Chapter 5. Hybrid-solid oxide electrolysis cell: A new strategy for efficient hydrogen production	59
5.1. Introduction.....	59
5.2. Experimental Section	63
5.3. Results and discussion	65
5.4. Conclusions.....	71
Chapter 6. The First Observation of Proton Trace in Triple Conducting Oxides: Thermodynamics and Kinetics of Proton	73
6.1. Introduction.....	73
6.2. Experimental Section	75
6.3. Results and Discussion.....	79
6.4. Conclusion	86
List of Publications	87
Acknowledgements	90
References.....	91

List of Figures

Figure 1 Schematic illustration of working principle for protonic ceramic fuel cell.....	1
Figure 2 Schematic illustration of working principle for ceramic fuel cell and ceramic electrolysis cell	3
Figure 3 Graphical representation of all the losses under practical fuel cell operating condition ⁸	6
Figure 4 Schematic illustration of the water formation reaction at the H ⁺ -SOFC cathode using (a) mixed ionic and electronic conductors (O ²⁻ /e ⁻) and (b) a triple conducting oxides (H ⁺ /O ²⁻ /e ⁻)	11
Figure 5 Development of proton conducting electrolyte material.....	12
Figure 6 Unit cell structure of perovskite	13
Figure 7 (a) The structure of layered perovskite unit cell(AA'B ₂ O _{5+d}) and (b) a proposed mechanism for the bulk diffusion of the mobile oxygen species via the pore channels; a zig-zag type trajectory though the CoO plane perpendicular to the PrO plane.....	14
Figure 8. (a) XRD patterns of GdBa _{0.5} Sr _{0.5} Co _{2-x} Fe _x O _{5+δ} (x = 0, 0.5, and 1.0) sintered at various temperatures, (b) observed and calculated XRD profiles and the difference between them for GdBa _{0.5} Sr _{0.5} CoFeO _{5+δ}	19
Figure 9 The in-situ XRD patterns of the GdBa _{0.5} Sr _{0.5} CoFeO _{5+δ} at different temperatures at various temperatures. The inset shows the dependence of temperature on unit cell volume V (Å ³)......	20
Figure 10 XRD patterns of GdBa _{0.5} Sr _{0.5} Co _{2-x} Fe _x O _{5+δ} (x = 0, 0.5, and 1.0)-GDC mixture after sintered at 1273 K in air for 4 h.	21
Figure 11 SEM images showing the microstructure of a single cell (GDC - GdBa _{0.5} Sr _{0.5} Co _{2-x} Fe _x O _{5+δ} / GDC / NiO-GDC): (a) x=0, (b) x=0.5, (c) x=1.0, and the cross section of a single cell: (d) x=1.0.	22
Figure 12 Thermogravimetric data of GdBa _{0.5} Sr _{0.5} Co _{2-x} Fe _x O _{5+δ} (x = 0, 0.5, and 1.0) showing the variation of oxygen loss (%) as a function of temperature.....	23
Figure 13 Electrical conductivities of GdBa _{0.5} Sr _{0.5} Co _{2-x} Fe _x O _{5+δ} (x = 0, 0.5, and 1.0) in a temperature range of 373 to 1023 K in air.....	24
Figure 14 (a) Typical impedance spectra of the symmetrical cells at 873 K, (b) Arrhenius plots of the ASRs for GdBa _{0.5} Sr _{0.5} Co _{2-x} Fe _x O _{5+δ} (x = 0, 0.5, and 1.0), and (c) GBSCF10-yGDC (y = 0, 20, 40, and 50 wt%) symmetrical cells.....	26
Figure 15 I-V curves and corresponding power density curves of single cells (GdBa _{0.5} Sr _{0.5} Co _{2-x} Fe _x O _{5+δ} /GDC/NiO-GDC) under various temperatures: (a) x = 0, (b) x = 0.5, and (c) x = 1.0....	28
Figure 16 Schematic illustration of the perovskite structure state as a function of ionic size	31
Figure 17 a) XRD patterns of the BSCF and LBSCF sintered at 1473K and 1423K, respectively for 12h. b) Observed, calculated XRD profiles and the difference between them for LBSCF. c) XRD patterns of cathode-GDC mixture sintered at 1273 K in air for 4 h. d) Bright-field (BF) TEM image of LBSCF-GDC cathode sintered at 1273K in air for 4h. Inset shows atomic-scale scanning TEM (STEM) high-angle annular dark-field (HAADF) image of LBSCF.	34
Figure 18 Thermogravimetric data of the BSCF and LBSCF presenting a variation of oxygen contents as a function of temperature in air.	35
Figure 19 Electrical conductivity data for the BSCF ^[24] and LBSCF as a function of temperature in air.	36
Figure 20 Scanning electron microscope image of porous a) BSCF-40GDC, b) LBSCF-40GDC composite and c) cross-section of LBSCF-40GDC/GDC/NiO-GDC single cell.	37
Figure 21 a) Impedance spectra and fitted Nyquist plots with BSCF-40GDC and LBSCF-40GDC composite cathode on symmetrical cell measured at 873 K under OCV condition. b) Arrhenius plot of polarization resistance for BSCF-40GDC and LBSCF-40GDC composite cathode.	39
Figure 22 I-V curve and corresponding power density curves of single cell for a) BSCF-40GDC and b) LBSCF-40GDC cathodes in various temperatures.....	40
Figure 23 Tolerance factors (t _f) of the BSCF and LBSCF materials as function of mole fraction for quadrivalence B-site ion from the sum of trivalence and quadrivalence B-site ion. The existing	

region of t_f values for each samples is in colored.....	41
Figure 24 X-ray diffraction patterns for the BSCF and LBSCF re-annealed at 973 K in ambient air; a) and b). CO ₂ durability result of both cathode powders re-annealed at 1173 K in 10 vol% CO ₂ ; c) and d). Peaks of the hexagonal phase and carbonates are marked with a hexagon and asterisk, respectively.	42
Figure 25 a) Oxygen non-stoichiometry and b) electrical conductivities of the BSCF [38] and LBSCF under various $p(\text{O}_2)$ (atm) at 973 K by coulometric titration.	44
Figure 26 Long term stability data for the BSCF-40GDC and LBSCF-40GDC with applying a constant voltage of 0.6 V at 823 K.....	45
Figure 27 Schematic illustration of the water formation reaction at the H ⁺ -SOFC cathode using (a) a mixed ionic and electronic conductors (O ²⁻ /e ⁻) and (b) a triple conducting oxides (H ⁺ /O ²⁻ /e ⁻)	49
Figure 28 (a) The structure of layered perovskite unit cell(AA'B ₂ O _{5+δ}) and (b) a proposed mechanism for the bulk diffusion of the mobile oxygen species via the pore channels based on our previous study ⁵⁸ ; a zig-zag type trajectory though the CoO plane perpendicular to the PrO plane.	50
Figure 29 XRD patterns of (a) NBSCF powder sintered at 1323 K for 12 h, (b) BZCYYb powder sintered at 1673 K for 4 h, and (c) NBSCF–BZCYYb mixture after sintered at 1223K for 24 h.	53
Figure 30 Scanning electron microscope image of (a) porous NBSCF cathode and (b) cross-section of the single cell.....	54
Figure 31 Long term stability data of the single cells (NBSCF/BZCYYb/NiO-BZCYYb) with applying a constant voltage of 0.6 V at 1023 K.....	55
Figure 32 (a) Impedance spectra of the single cell (NBSCF/BZCYYb/NiO-BZCYYb) measured under open-circuit condition and (b) I-V curve and corresponding power density curves of the single cell at various temperatures after 500h stability test.	56
Figure 33 Schematic diagrams of the working principle. (a) Oxygen-SOEC, (b) proton-SOEC, and (c) Hybrid-SOEC system. In the oxygen- and proton-SOEC systems (a and b), even in the presence of steam on both electrodes, the electrochemical reaction for the water-electrolysis can occur at only one electrode. On the contrary, when mixed ion conducting electrolyte is used, the water electrolysis can occur at both at both air and hydrogen electrodes (so-called Hybrid-SOEC operating system), because the electrolyzed ion species (O ²⁻ and H ⁺) can be counter-diffused across the mixed ionic conducting electrolyte. Consequently, in the Hybrid-SOEC system (c), more hydrogen could be generated by allowing simultaneous the oxygen-SOEC and proton-SOEC operation.....	60
Figure 34 X-ray diffraction pattern of BZCYYb-NBSCF composite sintered at 950 °C 4hours.	65
Figure 35 Schematic illustration of the experimental setup employed for the Hybrid-SOEC experiments.	66
Figure 36 I-V curves for a Ni-BZCYYb / BZCYYb / NBSCF-BZCYYb cell. (a) I-V curves in the Hybrid-SOEC system at various temperatures (under 90% H ₂ and 10% steam fed in the hydrogen electrode side and 90% air and 10% steam fed in the air electrode side). (b) I-V curves for comparison of present work and other studies reported in the literature at 700 °C (the performance range of I-V curves for the oxygen-SOEC and proton-SOEC is shaded in green and blue color, respectively). (c) Comparison of the current densities at 700 °C and 1.3 V.	67
Figure 37 I-V curves for a Ni-BZCYYb/BZCYYb/NBSCF-BZCYYb cell under 90% H ₂ and 10% steam fed in the hydrogen electrode side and 90% air and 10% steam fed in the air electrode side (red line, Hybrid-SOEC system), 90% H ₂ and 10% steam fed in the hydrogen electrode side and 100% air fed in the air electrode side (blue line, oxygen-SOEC system), and 100% H ₂ in the hydrogen electrode side and 90% air and 10% steam fed in the air electrode side (green line, proton-SOEC system) at 700 °C.....	68
Figure 38 Stability test of single cell as a Hybrid-SOEC (a) Time-dependence of the cell voltage applied 0.45 A cm ⁻² at 550 °C during Hybrid-electrolysis under 90% H ₂ and 10% steam fed in the hydrogen electrode and 90% air and 10% steam fed in the air electrode. The BZCYYb electrolyte is approximately 20 μm thick and the NBSCF-BZCYYb composite air electrode is around 15 μm thick. (b - d) SEM micrographs of Ni-BZCYYb / BZCYYb / NBSCF-BZCYYb cell as Hybrid-SOEC after stability at 550 °C during over 60 hours; (b) cross-sectional SEM micrograph of the fabricated cell after stability test, with BZCYYb electrolyte supported on Ni-BZCYYb hydrogen	

- electrode, and NBSCF-BZCYYb air electrode; (c) microstructure of interface between NBSCF-BZCYYb and BZCYYb electrolyte; (d) microstructure of interface between Ni-BZCYYb and BZCYYb electrolyte..... 69
- Figure 39 Comparison of the electrochemical performance of water-electrolysis by the Hybrid-SOEC and other representative applications. Polarization curves for the comparison with (a) the PEM-electrolysis using Ir anode and Pt cathode (performance range of the polymer electrolyte membrane (PEM)-electrolysis is colored by blue) and (b) acidified water-electrolysis using Pt, polypyrrole molybdenum sulfide (PPy/MoS_x), molybdenum phosphosulfide (MoP|S), and cobalt phosphide (CoP) catalyst..... 71
- Figure 40 XRD diffraction pattern of (a) PBSCF sintered at 1150 °C for 12 h, (b) PBSCF after steam exposure (10 vol% H₂O containing air) for 100 h at 650 °C, (c) BZCYYb sintered at 1400 °C for 4 h, and (d) a mixture of PBSCF and BZCYYb sintered at 950°C 4h. 75
- Figure 41 (a) Cross-sectional SEM image of PBSCF/BZCYYb/NiO-BZCYYb cell. (b) SEM image of porous PBSCF cathode..... 76
- Figure 42 Surface profile data of the PBSCF pellet after ToF-SIMS measurement. Inset image shows the crater on the PBSCF surface after Cs⁺ beam sputtering. 77
- Figure 43 Schematic illustration of preparation of the D₂O-exchanged PBSCF for the ToF-SIMS measurement..... 79
- Figure 44 Protonic properties of the surface of PBSCF pellet measured by ToF-SIMS. (a) Mass spectrum analysis of a D₂O-exchanged PBSCF around U = 2 and 18. (b-e) Secondary ion mapping images of D⁻ and OD⁻ for the surface of PBSCF pellet before (b, d) and after D₂O (c, e) exchange. 80
- Figure 45 (a) 3D-mapping image of OD⁻ ion intensity in the 50 × 50 μm of the analysis area for D₂O-exchanged PBSCF sample annealed at 350 °C. (b) and (c) Normalized OD⁻ depth profile obtained from D₂O-exchanged PBSCF annealed at a temperature range of 250 ~ 550 °C. The solid lines represent the best fit to the Fick's second law. (d) and (e) Diffusion and kinetics coefficient of proton (D^{*}_H and k^{*}_H) values of the PBSCF sample. (f) Comparison of diffusion coefficients (D^{*}_H) of the PBSCF with other representative MIEC materials: Ba_{0.5}Sr_{0.5}Co_{0.8}Fe_{0.2}O_{3-δ} (BSCF), PrBaCo_{2.0}O_{5+δ} (PBCO), GdBaCo_{2.0}O_{5+δ} (GBCO), La_{0.6}Sr_{0.4}CoO_{3-δ} (LSC), La_{0.6}Sr_{0.4}Co_{0.2}Fe_{0.8}O_{3-δ} (LSCF), and La_{27.15}W_{4.85}O_{55.28}V_{0.73} (LWO). Solid lines in the red and blue circle represent D^{*} values for oxygen ion and proton, respectively. 82
- Figure 46 Proton defect formation of PBSCF measured by the water-uptake properties of TCOs through thermogravimetric analysis (TGA) at 400 °C under dry air and 3 vol% H₂O air. Concentrations are given in unit of [(OH mol concentration)/(PBSCF mol concentration)] 83
- Figure 47 (a) Equilibrium constant of hydration reaction presented in the Arrhenius plot. The slope yields hydration enthalpy (ΔH). (b) ΔH values of various proton-conducting oxides for comparison. 84
- Figure 48 (a) Impedance spectra of the single cell (PBSCF/BZCYYb/NiO-BZCYYb) measured under open-circuit condition. (b) I-V curve and corresponding power density curves of the single cell at various temperatures. (c) Advantages and disadvantages of ceramic fuel cells by operating temperature..... 85

List of Tables

Table 1 Suggested elementary reaction steps and their reaction orders for MIEC and TCO cathode with proton-conducting electrolytes	48
--	----

Chapter 1. Introduction

1.1 Motivation and Research Objective

Among the various type of fuel cells, ceramic fuel cells have been extensively studied as an eco-friendly alternative energy device in the aspect of high energy conversion efficiency and continuous production of the electricity without pollutant emissions. The high operating temperature ($> 800\text{ }^{\circ}\text{C}$) of conventional O^{2-} conducting ceramic fuel cells (solid oxide fuel cells, SOFCs), however, cause serious issues such as chemical inter-diffusion and high thermal stress. In this regard, protonic ceramic fuel cells (PCFCs) (Figure 1) using proton conducting oxides (PCOs) have received great attention as promising candidates for the intermediate to low temperature operation ($400 \sim 800\text{ }^{\circ}\text{C}$) because of its relatively high ionic conductivity and low activation energy for the H^+ transport compared with the O^{2-} transport in the conventional O^{2-} conducting oxides (YSZ, GDC, LSGM, and etc.)¹

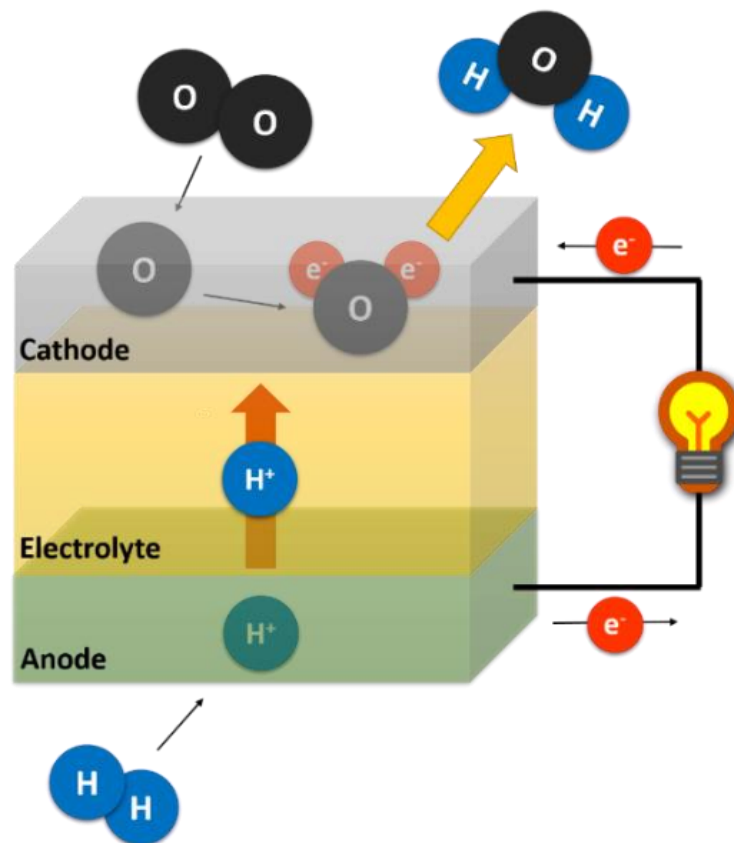


Figure 1 Schematic illustration of working principle for protonic ceramic fuel cell

After the first report of high-temperature proton conductivity in oxide material by Iwahara and co-workers in 1980s, many researchers have been investigated to utilizing the proton motion in solid oxides (so-called, “protonics” combining the proton and electronics) for the efficient PCFC operation. In the early stage of

protonics research, the PCO electrolytes based on barium-zirconates and -cerates have been widely used as electrolyte materials. Among those PCO electrolytes, aliovalent-doped $\text{BaCe}_{1-x}\text{Zr}_x\text{O}_{3-\delta}$ ($0 < x < 1$) demonstrates high proton conductivity with overcoming their major issues such as poor sinterability and low proton conductivity under practical operating conditions.² Recently, a barium zirconate-cerate co-doped with Y and Yb, $\text{BaZr}_{0.1}\text{Ce}_{0.7}\text{Y}_{0.1}\text{Yb}_{0.1}\text{O}_{3-\delta}$ (BZCYYb), is reported with high ionic conductivity ($\sim 0.01 \text{ S cm}^{-1}$) and excellent tolerance to sulfur poisoning and coking.³ However, the wide application of PCFCs is limited because of the cathodic polarization.⁴

Generally, mixed ionic (O^{2-}) and electronic conductors (MIECs) have been used as the cathode material for the conventional SOFC system because of their excellent electron conductivity and catalytic activities for the oxygen reduction reaction (ORR). However, when MIECs are used as PCFC cathodes, the electrochemically active site is limited into the interface between cathode and electrolyte, because the protons should diffuse from the PCO electrolyte to the cathode material in order to generate the electricity. Therefore, triple conducting oxides (TCOs) allowing the simultaneous transport of H^+ , O^{2-} and e^- are required to effectively extend the electrochemically active sites to the entire surface of the cathode.

To increase the electrochemical performance of the TCOs, extensive efforts have been devoted with two primarily different approaches. The first approach is doping various aliovalent elements into pure proton conducting oxides (*i.e.* BZO or BCO) to enhance their electrochemical activity for O^{2-} and e^- . For example, many trivalent ions are doped into the B-site of PCO to increase oxygen-ion kinetics, and O'Hayre group recently reported that transition-metal cations (Co and Fe) doped $\text{BaZr}_x\text{Y}_{1-x}\text{O}_{3-\delta}$ presents great catalytic properties as the PCFC cathode by activating electronic conduction while maintaining protonic property of barium zirconates.⁵ Another approach for the development of TCO is finding MIEC (O^{2-}/e^-) materials having high protophilic properties. Since this approach has advantages that it is already well-studied on the electro-catalytic mechanism of O^{2-} and e^- in MIECs, many researchers have investigated to find protophilic MIECs for high performance PCFCs. Recently, our group reported that a layered perovskite material, $\text{NdBa}_{0.5}\text{Sr}_{0.5}\text{Co}_{1.5}\text{Fe}_{0.5}\text{O}_{5+\delta}$ (NBSCF), shows excellent electrochemical performance with low polarization resistance of $0.081 \Omega \text{ cm}^2$ at $700 \text{ }^\circ\text{C}$ under practical PCFC operating condition. Even though these efforts, the systematic development of TCOs is very difficult because of characterization challenges of protonics in the TCOs, as below reasons.

In order to identify the protonic behavior of PCOs (*i.e.*, H^+ -conducting electrolyte materials), the electromotive force (EMF) method is used through the measurement of open-circuit voltage (OCV) for concentration cells. For the TCOs, However, it is difficult to measure the protonic properties by the EMF method because of their large electron conductivity. In addition, it is very complicated to analyze the thermodynamics and kinetics properties of TCOs, because not only H^+ , but also O^{2-} and e^- are simultaneously affect the cathodic performance of PCFCs. To overcome these complexities of the characterization for protonics in TCOs, it could be an effective candidate to study the proton properties of MIEC materials. The MIECs have been already well-optimized and -studied on their electrochemical reaction mechanism of O^{2-} and e^- in the ceramic fuel cell system in many literatures, therefore, the protonic properties of TCOs can be understood more clearly.

Therefore, my research mainly focuses on the understanding and development of perovskite catalysts for

ceramic electrochemical cells. In particular, to solve the problems mentioned above, I have comprehensively investigated the thermodynamic and kinetic properties of the oxygen ion, electron, and proton in the perovskite materials.

Chapter 1 provides basic operating principle and general theoretical fundamentals for understanding how ceramic electrochemical cells work with state art of the technologies.

In chapter 2, $\text{GdBa}_{0.5}\text{Sr}_{0.5}\text{Co}_{2-x}\text{Fe}_x\text{O}_{5+d}$ layered perovskite oxides have been studied as a promising cathode material for IT-SOFCs.

In chapter 3, it is reported that the remarkable enhancement of the phase stability and electrochemical performance of La^{3+} doped BSCF by a strategic approach.

In chapter 4, an excellent anode-supported H^+ -SOFC material system using a triple conducting ($\text{H}^+/\text{O}^{2-}/\text{e}^-$) oxide (TCO) as a cathode material for H^+ -SOFCs are reported

In chapter 5, a new finding in exploring a SOEC based on a mixed-ion conductor that can transport both oxygen ion and proton at the same time, which is denoted as “Hybrid-SOEC” is demonstrated

In chapter 6, the observation of proton trace in triple conducting oxides are reported.

1.2. General Introduction

1.2.1 The basis of fuel cell and electrolyzer

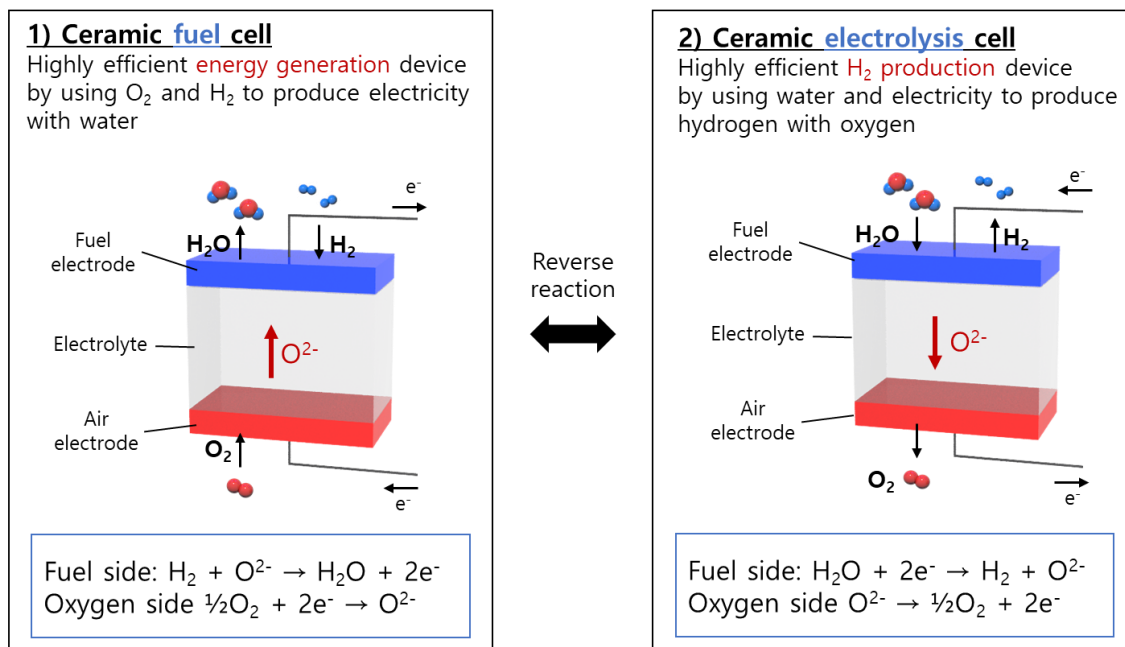


Figure 2 Schematic illustration of working principle for ceramic fuel cell and ceramic electrolysis cell

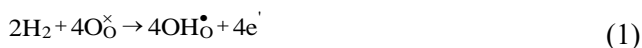
With exponential growth in energy consumption and with finite fossil fuel resources, the necessity for high efficiency energy conversion devices is increasing. Fuel cells are energy production devices that convert directly

from chemical energy to electrical energy. Among those fuel cells, ceramic fuel cells (CFCs) have attracted attention because of their high energy conversion efficiencies, low pollutant emissions, efficient reclamation of waste heat, and excellent fuel flexibility. (Figure 2)

Meanwhile, water-electrolysis cells are electrochemical hydrogen production devices having a reverse reaction of a fuel cell reaction. In a water-electrolysis cell, hydrogen is produced from the hydrogen electrode through electrolysis from water, and oxygen is produced from the air electrode. Solid oxide electrolysis cells (SOECs) are considered as a promising water-electrolysis system because high-temperature water electrolysis based on ceramic electrolytic cells (CECs) is much more efficient because of their advantages for the water splitting both thermodynamically and kinetically.

1.2.2. Operating principle of ceramic fuel cells

Ceramic fuel cells can be classified into two types depending on the type of oxide electrolyte: (1) solid oxide fuel cell having oxygen ion conducting electrolyte materials, (2) Protonic ceramic fuel cell having proton conducting electrolyte materials. Proton-conducting oxides are ideally suited for the electrolytes because of the low activation energy and high ionic conductivity at intermediate temperatures. In addition, protonic ceramic fuel cells (PCFCs) can avoid water formation, and thus dilution of the fuel, on the anode side during operation because water will form on the cathode side of the cell, which can lead to higher fuel utilization and greater Nernst potential of SOFCs. In the H^+ -SOFC system, mobile protons can be incorporated at the anode by forming a covalent bond between the lattice oxygen and proton which originates from the dissociated water. This mobile proton transfer through the dense electrolyte to the cathode. The overall half reactions at the anode and cathode could be expressed as Equation. (1) and (2), respectively:



Oxygen anions produced at the cathode travel to the anode through the oxygen-ion conducting electrolyte. If hydrogen is used as a fuel with oxygen as an oxidant, water and two electrons are the products at anode permanently as long as fuel and oxygen continue to be supplied.⁶

1.2.3. Operating principle of ceramic electrolyzer

Oxygen-SOEC is one of the most promising candidate for the high temperature water electrolysis. In this system, the hydrogen is produced from the water-electrolysis reaction at the hydrogen electrode side. As an

electrolyte material, yttria-stabilized zirconia (YSZ) is conventionally used because the YSZ exhibits sufficient pure oxygen ion conductivity at high temperatures ($> 800\text{ }^{\circ}\text{C}$). Despite the benefits of high temperature operation, however, wide application of the oxygen-SOEC has been inhibited because of critical issues (*e.g.*, poor long-term cell stability, interlayer diffusion, fabrication and materials problems).

For these reasons, proton-SOECs using proton conducting oxides (PCOs) as electrolyte materials have acquired much interests because of their intermediate to low temperature operation. In the proton-SOEC system, the proton is generated by water electrolysis at the air electrode and this proton permeates through the pure proton-conducting electrolyte, and the permeated proton reacts with electrons to produce hydrogen at the hydrogen electrode. Recently, extensive efforts have been devoted to developing the PCOs based on barium-zirconates (BZO) and barium-cerates (BCO) to improve their chemical stability and proton conductivity. Among those PCOs, aliovalent-doped $\text{BaCe}_{1-x}\text{Zr}_x\text{O}_{3-\delta}$ ($0 < x < 1$) have demonstrated high proton conductivity and successfully eliminated major issues such as poor sinterability and low proton conductivity.⁷

1.3. Theoretical Background of ceramic fuel cells

1.3.1. Performance of ceramic electrochemical cells⁸

The performance of the fuel cell device can be summarized by the current-voltage characteristic graph. The current-voltage (*i-V*) curve, shows the voltage output of the fuel cell for a given current output. An ideal fuel cell would supply any amount of current (as long as it is supplied with sufficient fuel), while maintaining a constant voltage determined by thermodynamics. However, the actual voltage output of a fuel cell under real system is less than the ideal thermodynamically expected voltage. Additionally, the more current that is drawn from a real fuel cell, the lower the voltage output of the cell, limiting the total power that can be delivered. The power (*P*) delivered by a fuel cell is given by the product of current and voltage.⁸

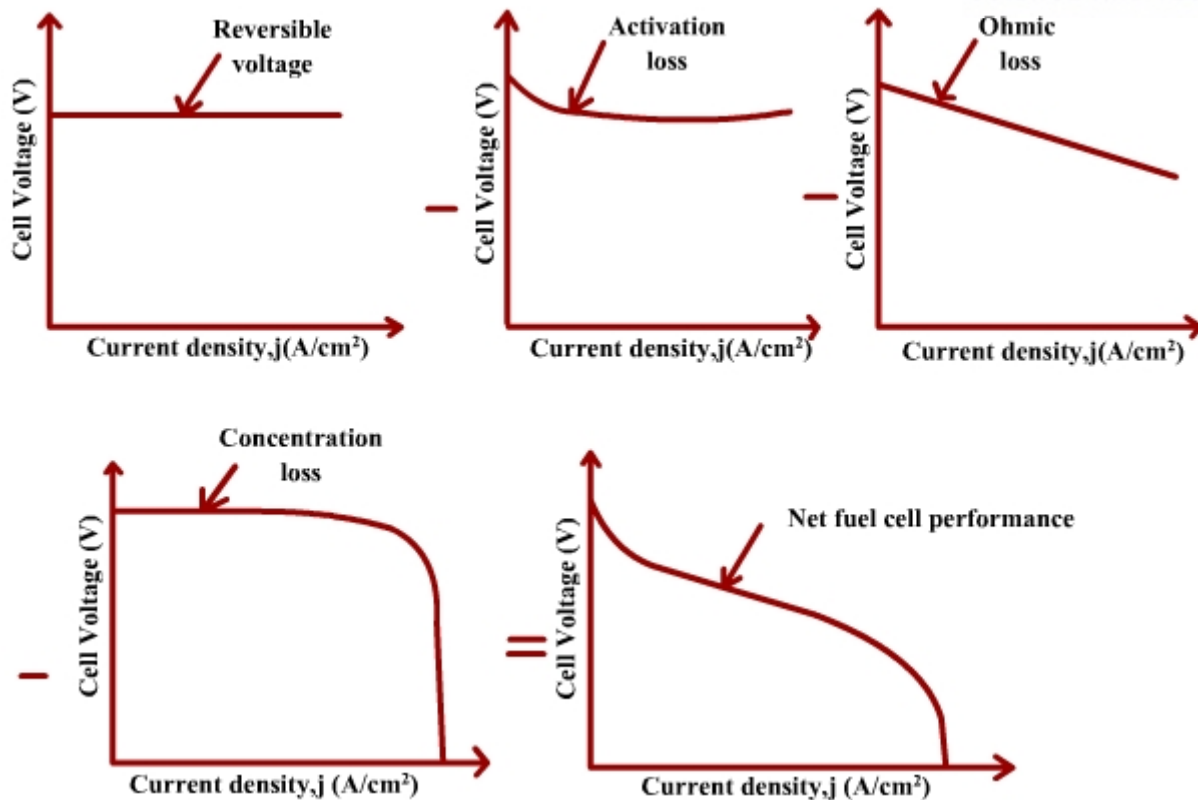


Figure 3 Graphical representation of all the losses under practical fuel cell operating condition ⁸

A typical current-voltage (i-V) curve obtained in SOFC is indicated as shown in Figure 3. The important factors to sign in this graph of cell voltage against current density are (1) the lower open circuit voltage compared to the theoretical value, (2) the rapid initial drop in voltage, (3) the slow, linear voltage drop in the intermediate current region, and (4) the fast voltage drop at higher current density. There are different kinds of polarization losses in fuel cell systems and are comprised of three contributions caused by the following factors;

- Kinetics of the electrochemical reaction (activation polarization)
- Internal electrical and ionic resistances (ohmic polarization)
- Limitations in mass transport (concentration polarization)

The activation polarization is basically associated to the rate determining step, charge transfer or the surface exchange reactions in the electrode. For the electrode reaction to be occurred, the activation polarization can be understood as the overvoltage consumed to provide the activation energy for the redox reactions in the electrode. The relationship between current density i and activation polarization can be expressed by the Butler-Volmer equation,

$$i = i_0 \left[\exp\left(\frac{(1-\alpha)nF\eta_{Act}}{RT}\right) - \exp\left(\frac{-\alpha nF\eta_{Act}}{RT}\right) \right]$$

where i_0 , α , η are the exchange current density, charge transfer coefficient, the overpotential, respectively

When the irreversibility is small, above can be written as the Tafel equation:

$$\eta_{Act} = a \pm b \log i$$

where a and b are constants and b is called the Tafel slope, indicating the catalytic activity. The ohmic polarization (*i.e.*, iR drop) is associated to the contact resistance between the components of cell. It also contains ionic electronic resistances in the electrodes, resistance in the electrolyte, interfacial resistance between the electrodes and electrolyte, and wire resistance in the external circuit. Concentration polarization depends on the concentration of reactants on the surface of the electrode as fuel and oxidant are used. If the reactants can not be provided quickly enough to maintain the rate of electrode reaction, depletion of the reactants will result in concentration polarization. The concentration polarization can be expressed as

$$\eta_{con} = \frac{RT}{nF} \ln\left(1 - \frac{i}{i_l}\right)$$

where i_l is the limiting current when the electrode reaction is completely governed by mass transfer. The total polarization of the fuel cell system is the sum of three principal polarizations as, ⁸

$$\eta_{Total} = \eta_{Act} + \eta_{Ohm} + \eta_{Con}$$

1.3.2. Thermodynamics of fuel cell

SOFC is an electrochemical device that directly converts Gibbs free enthalpy of combustion reaction by consuming fuel and oxidant gas to electricity. The 1st and the 2nd law of thermodynamics allow the description of a reversible fuel cell, meanwhile the 2nd law governs the transport processes reversibility. The 1st law of the thermodynamics gives,

$$q + w = \Delta H$$

The molar reaction enthalpy ΔH of the oxidation consists of work and heat energy. The second law of thermodynamics applied on reversible processes yields

$$\oint \Delta S = 0 \rightarrow q = q_{rev} = T \Delta S$$

where the reversible heat exchange with the environment equalizes the created reaction entropy,

$$q_{rev} + w_{rev} = \Delta H$$

Reaction entropy is the result of various opportunities for heat energy to be stored between the absolute zero level of temperature and the reactor temperature level.

$$w_{rev} = \Delta H - T \Delta S$$

Using the ambient temperature as a reference for the calculation of the Gibbs free enthalpy, ΔG , the reversible work of the reaction is equal to the Gibbs free enthalpy of the reaction

$$w_{rev} = \Delta G = \Delta H - T \Delta S$$

Based on the first and second laws of thermodynamics, the transfer of energy from one form to another can be confirmed by using the thermodynamic potential. From the first and the second laws of thermodynamics, an equation for internal energy (U) that is based on the variation of two independent variables of entropy S and volume V is derived where p is the pressure and T is temperature:

$$dU = T dS - p dV$$

Note that $T dS$ represents the reversible heat transfer and $p dV$ is the mechanical work. The following equations show how the dependent variables (T and p) are related to variations in the independent variables (S and V):

$$\left(\frac{dU}{dS}\right)_V = T$$

$$\left(\frac{dU}{dV}\right)_S = -p$$

A conversion of U using a Legendre transform begins with defining the new thermodynamic potential G (T , p) as follows:

$$G = U - \left(\frac{dU}{dS}\right)_V S - \left(\frac{dU}{dV}\right)_S V$$

$$G = U - TS + pV$$

The variation of G results in

$$dG = dU - TdS - SdT + pdV + Vdp$$

Since $dU = T dS - p dV$,

$$dG = -SdT + Vdp$$

The new thermodynamic potential H can be defined as

$$H = U - \left(\frac{dU}{dS}\right)_v$$

we obtain

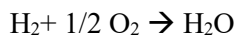
$$H = U + pV$$

where H stands for enthalpy. Through differentiation, it is revealed that H is a function of S and p :

$$dH = dU + pdV + Vdp$$

$$dH = TdS + Vdp$$

Considering the overall reaction of SOFCs,



$$\Delta G = \Delta G_{\text{H}_2\text{O}} - \Delta G_{\text{H}_2} - \frac{1}{2} \Delta G_{\text{O}_2}$$

If all the Gibbs free energy is consumed to electrical work, then

$$\Delta G = -nFE$$

where n and F represent number of electrons included in the chemical reaction and the Faraday constant, respectively.

Here, the Gibbs free energy is dependent on the temperature by the relation

$$\Delta G = \Delta H - T \Delta S$$

Substitution of the standard condition values ($T = 273.15 \text{ K}$, $p = 1 \text{ atm}$) into (1.4.19) gives the standard electrode potential E_0

$$E^0 = (237900 \text{ J mol}^{-1}) / (2 * 96485 \text{ C mol}^{-1}) = 1.23 \text{ V}$$

Beyond the standard condition, the theoretical reversible potential (E_{th}) can be derived from the Nernst equation as

$$E_{th} = E^0 - \left(\frac{RT}{2F}\right) \ln \left(\frac{p_{\text{H}_2\text{O}}}{p_{\text{H}_2} p_{\text{O}_2}^{1/2}} \right)$$

where R , T , p are the gas constant, absolute temperature, and partial pressure of each gas, respectively.

1.4. Materials for ceramic electrochemical cells

1.4.1. Cathode materials for SOFCs

SOFC cathodes must have high electrochemical activity on the surface for an efficient oxygen reduction reaction (ORR) and high diffusivity for the transfer of oxygen anions through the cathode bulk. Lanthanum strontium manganite (LSM) is widely used in the available SOFCs owing to its excellent compatibility with YSZ electrolyte and other cell components and its moderate electric (e^-) conductivity. Mechanically, it has a coefficient of thermal expansion (CTE) similar to that of YSZ and thus can reduce fatigue from thermal stress due to CTE mismatches. LSM can't transport ions well; therefore, the electrochemical reaction can only occur at the triple-phase boundary (TPB). New cathode material should have more reaction zone including TPB, to transmitting both electrons and oxygen ions. Mixed ionic electronic conducting (MIEC) ceramics, such as $LnBaCo_2O_{5+d}$ and $La_xSr_{1-x}Co_yFe_{1-y}O_{3-d}$ ($Ln = La, Pr, Nd, Sm, \text{ and } Gd$), are possible candidates. In addition, to make SOFC technology affordable, the reduced temperature operation at 600-800 °C can be a choice for the commercially viable long-term operation without severe degradation including lower price with less costly materials. However, sharp increases in the polarization resistance in the cathode part are observed at lower operating temperatures, leading to rapid decreases in SOFC performance levels. Conventional cathode materials having poor reactivity in the reduced temperature are a major challenge. In this regard, the cathodic polarization loss of a well-known cathode material LSM is undesirable for the IT-SOFCs.⁹

To overcome electro-catalytic issues, mixed ionic and electronic conductors (MIECs) have been adopted as cathode materials with consideration of their excellent catalytic activities for the oxygen reduction reaction (ORR). Among these MIEC materials, $Ba_{0.5}Sr_{0.5}Co_{0.8}Fe_{0.2}O_{3-\delta}$ (BSCF) has received tremendous attention for its fast oxygen-ion transport properties.

Nevertheless, wide application of BSCF has been inhibited by its structural instabilities at intermediate temperature. For example, Shao *et al.* showed that exponential decay in the measured oxygen permeation flux of BSCF occurs at temperature below 1098 K. Several groups have revealed that this degradation of BSCF results from a phase transition from a cubic structure into a two-phase mixture of hexagonal and cubic perovskites.¹⁰

1.4.2. Cathode materials for PCFCs

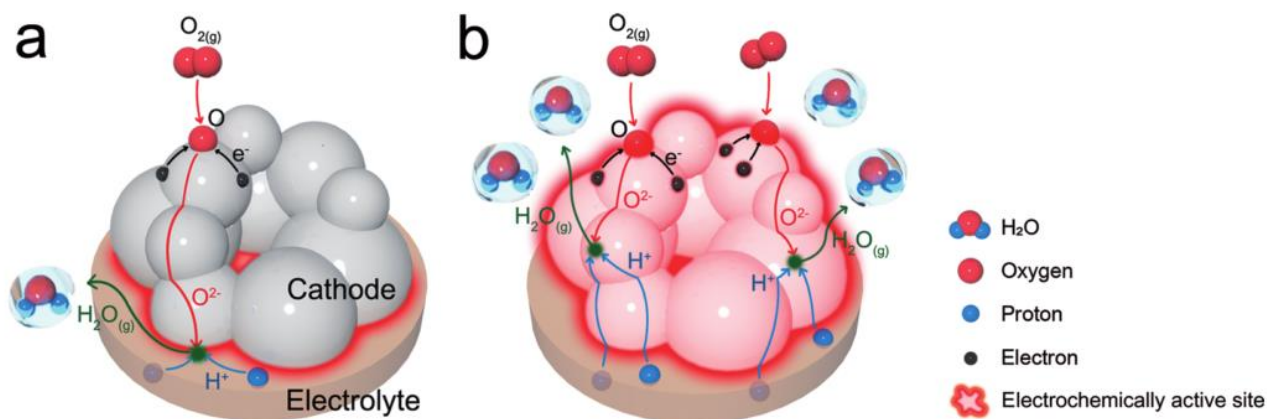


Figure 4 Schematic illustration of the water formation reaction at the H^+ -SOFC cathode using (a) mixed ionic and electronic conductors (O^{2-}/e^-) and (b) a triple conducting oxides ($H^+/O^{2-}/e^-$)

Generally, mixed ionic (O^{2-}) and electronic conductors (MIECs) are chosen as cathode material of O^{2-} -conducting SOFC system due to their excellent catalytic activities for the oxygen reduction reaction (ORR) by extending the electrochemically active site to the entire surface of cathode. On the contrary, for the reaction of proton and oxygen ion in the H^+ -SOFC system, oxygen ion should diffuse from the surface of MIECs to the interface between the proton conducting electrolyte and MIEC cathodes. Consequently, the MIEC cathodes limit the electrochemically active site to the interface between proton conducting electrolyte and cathode. Therefore, new approaches should be considered in tailoring of cathode materials for PCFCs. One of the basic requirements for high-performing PCFC cathode material is the high conductivity of the electron, oxide ion, and proton with the high chemical stability. In this regard, the triple conducting ($H^+/O^{2-}/e^-$) oxides (TCOs) effectively extend the electrochemically active site to the entire surface of cathode. (Figure 4)

To increase the electrochemical performance of the TCOs, extensive efforts have been devoted with two primarily different approaches. The first approach is doping various altrivalent elements into pure proton conducting oxides (*i.e.* BZO or BCO) to enhance their electrochemical activity for O^{2-} and e^- . For example, many trivalent ions are doped into the B-site of PCO to increase oxygen-ion kinetics, and O'Hayre group recently reported that transition-metal cations (Co and Fe) doped $BaZr_xY_{1-x}O_{3-\delta}$ presents great catalytic properties as the PCFC cathode by activating electronic conduction while maintaining protonic property of barium zirconates.⁵ Another approach for the development of TCO is finding MIEC (O^{2-}/e^-) materials having high protophillic properties. Since this approach has advantages that it is already well-studied on the electro-catalytic mechanism of O^{2-} and e^- in MIECs, many researchers have investigated to find protophillic MIECs for high performance PCFCs. Recently, our group reported that a layered perovskite material, $NdBa_{0.5}Sr_{0.5}Co_{1.5}Fe_{0.5}O_{5+\delta}$ (NBSCF), shows excellent electrochemical performance with low polarization resistance of $0.081 \Omega \text{ cm}^2$ at $700 \text{ }^\circ\text{C}$ under

practical PCFC operating condition.

1.4.3. Development of proton conducting oxide for electrolyte material

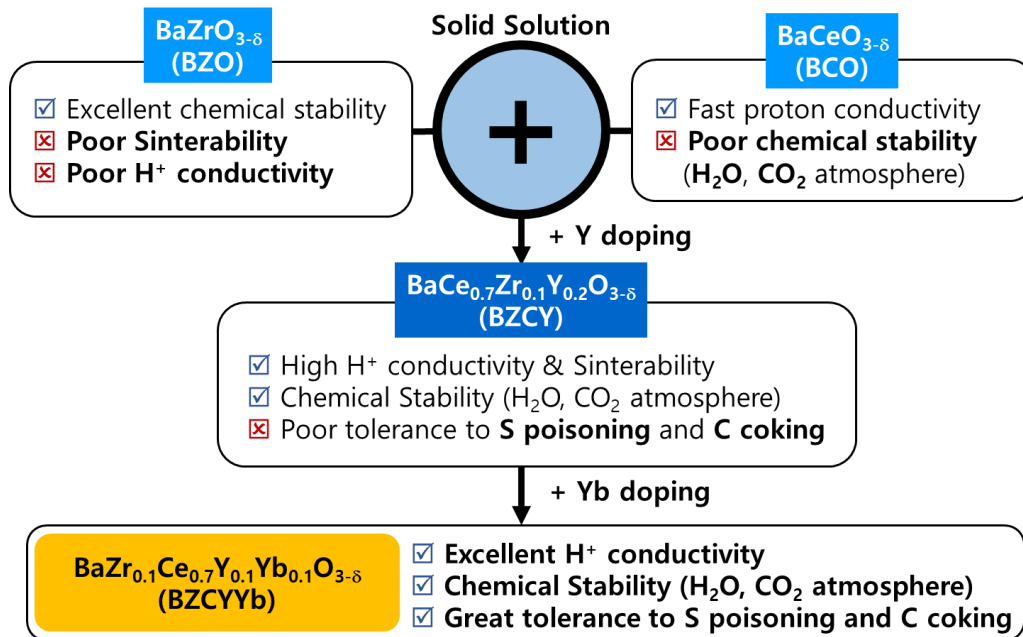


Figure 5 Development of proton conducting electrolyte material

Among proton conducting oxides for the electrolyte, the doped barium cerate and barium zirconate based materials are considered as two of the most promising candidates for H⁺-SOFC applications because of their fast proton transports. (Figure 5) Barium cerate based materials have high conductivity but with limited stability, especially in steam or CO₂ containing atmospheres. On the other hand, barium zirconate-based materials exhibited excellent chemical stability in steam or CO₂ containing atmospheres, but their conductivity is one order of magnitude lower than that of the barium cerate systems. A good combination between them, Ba(Zr_{0.1}Ce_{0.7}Y_{0.2})O_{3-δ} (BZCY) showed a great potential to possess the high conductivity while maintaining excellent chemical stability. Recently, Liu group reported a barium zirconate-cerate co-doped with Yb and Y, BaZr_{0.1}Ce_{0.7}Y_{0.1-x}Yb_xO_{3-δ} (BZCYYb), that displays excellent tolerance to sulfur poisoning and coking. This material is a very unique mixed ion conductor; it contains and allows rapid transport of both protonic defects and oxide ion vacancies, resulting in a high ionic conductivity (~0.01 S cm⁻¹ at humidified O₂ atmosphere). However, the study based on BZCYYb electrolyte in application of SOFC are still at early stages and the performance of the full cell is limited by electrode materials, especially the cathode.⁶

1.4.4. Various type of structures for cathode materials

Simple Perovskite Structure

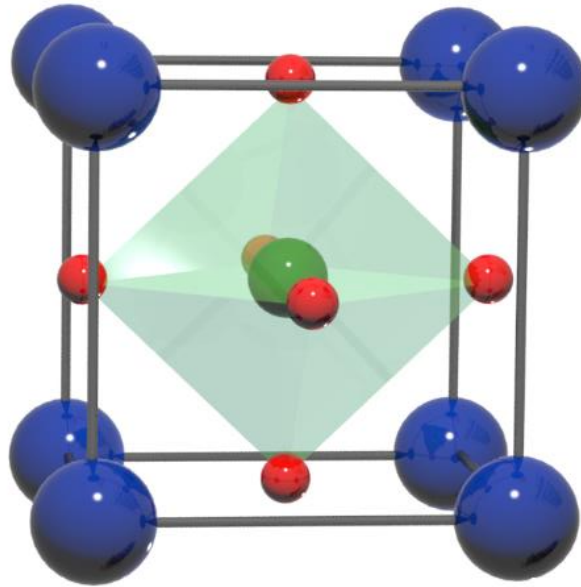


Figure 6 Unit cell structure of perovskite

Perovskite, calcium titanium oxide mineral (CaTiO_3), was named after the Russian mineralogist Lev Perovski, which is very stable and orthorhombic at high temperatures. Combination of the large oxide ion with a smaller radius metal ion gives a cubic close-packed crystal structure of oxygen ions along with interstitial metal ions. For the chemical formula ABX_3 , the crystal structure is the perovskite obtained by the partial replacement of the oxygen with cation. For example, SrTiO_3 has a three-dimensional net of corner sharing $[\text{TiO}_6]$ octahedra with Sr^{2+} ions in twelve-fold cavities between the polyhedral (Figure 6). In the cubic ABX_3 perovskite structure ($a = 3.905 \text{ \AA}$, space group $Pm-3m$, $Z = 1$), the A atoms are in the $(\frac{1}{2}, \frac{1}{2}, \frac{1}{2})$ position, the B atoms in the $(0, 0, 0)$ position, and the X atoms in three positions $(\frac{1}{2}, 0, 0)$; $(0, \frac{1}{2}, 0)$; and $(0, 0, \frac{1}{2})$.

A simple cubic structure has the A site cation is 12-fold-coordinated with oxygen ions, while the B site cation is 6-fold-coordinated. Depending on the constituents A and B ions of the perovskite ABO_3 , it can be an oxygen conductor (BaCoO_3 and SrCoO_3) or a proton conductor (BaCeO_3 and SrCeO_3). Size, changes from the original composition, and the Jahn-Teller effect can explain the distortion of the structure. A tolerance factor t and an octahedral factor μ are an important parameter to define stability and structure; here, t is as the ratio of the distance A-X to the distance B-X ($t = (R_A + R_X) / \{\sqrt{2}(R_B + R_X)\}$, where R_A , R_B and R_X are the ionic radii of the corresponding ions) and μ is defined as the R_B/R_X . The cubic structure of can be maintained within certain range of t , 0.89–1.0, and it changes to tetragonal or orthorhombic structures with t values over 1.0. ¹¹

Ordered Perovskite Structure

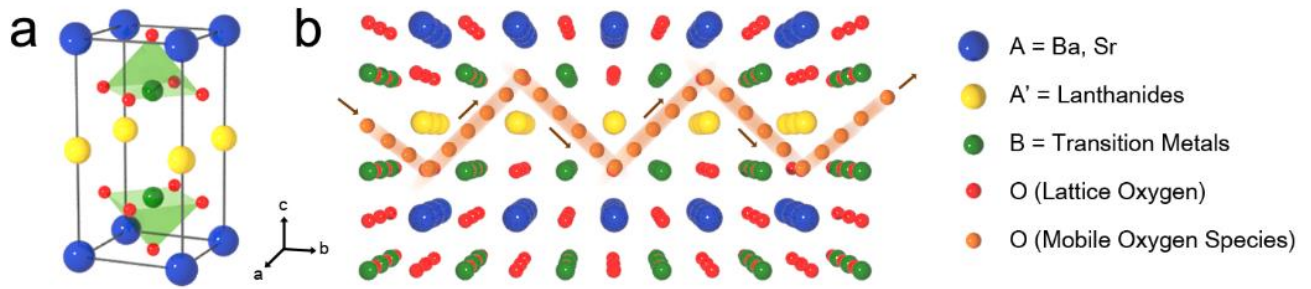


Figure 7 (a) The structure of layered perovskite unit cell($AA'B_2O_{5+d}$) and (b) a proposed mechanism for the bulk diffusion of the mobile oxygen species via the pore channels; a zig-zag type trajectory through the CoO plane perpendicular to the PrO plane.

Layered perovskite oxides such as $\text{LnBaCo}_2\text{O}_{5+\delta}$ ($\text{Ln} = \text{Pr, Nd, Sm, and Gd}$) have received attention as cathode materials for IT-SOFCs. The layered perovskites have a general formula described with $AA'B_2O_{5+\delta}$, where A is trivalent lanthanide ion, A' is alkaline earth metal and B is a first-row transition metal. (Figure 7) Generally, the layered structure with a stacking sequence of $\dots[A'O][BO_2][AO_8][BO_2]\dots$ is generated from the size difference between the large A' ions and relatively small A ions. These layered structures reduce the oxygen bonding strength in the $[AO_8]$ layer and create the disorder-free channel for fast oxygen diffusion and surface exchange. Recently, many research groups have reported the enhancement of the stability and electrochemical performance originated from the various ion substitution into the B site. For example, it was reported that substitution of Fe for Co improves the oxygen kinetics as well as the long-term stability, while Cu substitution for Co reduces the TEC and enhances the redox stability.¹²

Chapter 2. Effect of Fe Doping on Layered $\text{GdBa}_{0.5}\text{Sr}_{0.5}\text{Co}_2\text{O}_{5+\delta}$ Perovskite Cathodes for Intermediate Temperature Solid Oxide Fuel Cells

Layered-perovskite cathode materials have attracted considerable attention for intermediate temperature solid oxide fuel cells (IT-SOFCs) because of high catalytic activity for fast oxygen ion diffusion through pore channels and oxygen reduction reaction (ORR) at low temperature. In this study, we investigated the Fe doping effect into Co sites on the electrochemical and electrical properties for a layered perovskite, $\text{GdBa}_{0.5}\text{Sr}_{0.5}\text{Co}_{2-x}\text{Fe}_x\text{O}_{5+\delta}$ ($x = 0 \sim 1.0$), for IT-SOFC cathode materials. Moreover, electrochemical properties of $\text{GdBa}_{0.5}\text{Sr}_{0.5}\text{CoFeO}_{5+\delta}$ - γ GDC ($\gamma = 0, 20, 40, \text{ and } 50 \text{ wt\%}$) cathodes were estimated to determine the optimized cell performance. At a given temperature, the electrical conductivity and the area specific resistances (ASRs) of $\text{GdBa}_{0.5}\text{Sr}_{0.5}\text{Co}_{2-x}\text{Fe}_x\text{O}_{5+\delta}$ decrease with Fe content. The lowest ASR of $0.067 \Omega \text{ cm}^2$ was obtained at 873 K for the $\text{GdBa}_{0.5}\text{Sr}_{0.5}\text{CoFeO}_{5+\delta}$. The $\text{GdBa}_{0.5}\text{Sr}_{0.5}\text{CoFeO}_{5+\delta}$ composite with 40 wt% GDC was identified as an optimum cathode material, showing the highest maximum power density (1.31 W cm^{-2}) at 873 K, and other samples also showed high power density over 1.00 W cm^{-2} .

This chapter has been published.

Reproduced with permission from Kim. J., *et al.*, Effect of Fe Doping on Layered $\text{GdBa}_{0.5}\text{Sr}_{0.5}\text{Co}_2\text{O}_{5+\delta}$ Perovskite Cathodes for Intermediate Temperature Solid Oxide Fuel Cells, *Journal of the American Ceramic Society*, 97, 651 (2014). Copyright 2014. *Journal of the American Ceramic Society*, Wiley.

2.1. Introduction

Solid oxide fuel cells (SOFCs) have many advantages such as high energy conversion efficiency, efficient regeneration of waste heat, low pollutant emissions and extensive fuel flexibility. Considerable problems, however, emerge with high operating temperature (973 - 1273 K), such as high cost and incompatibility of the thermal expansion coefficient (TEC), which can cause thermal stress and undesirable reactions between the electrode and electrolyte. Therefore, great efforts have been made to lower the operating temperature of the SOFC to the intermediate range (773 - 973 K) for long-term stability and flexible choice of the SOFC material. However, operation at intermediate temperature causes serious problems associated with degradation of the electrocatalytic activity to the oxygen reduction reaction (ORR) on the cathode.¹³⁻¹⁵

To overcome these electro-catalytic problems, mixed ionic and electronic conductors (MIECs) have been used as SOFC cathodes.¹⁶ Especially, cobalt based simple perovskites having an excellent catalytic activity, such as $\text{Ba}_{0.5}\text{Sr}_{0.5}\text{Co}_{0.8}\text{Fe}_{0.2}\text{O}_{3-\delta}$ and $\text{La}_{0.6}\text{Sr}_{0.4}\text{Co}_{0.2}\text{Fe}_{0.8}\text{O}_{3-\delta}$ ¹⁷, have been suggested as MIEC cathodes.

Layered perovskite oxides have received much attention in recent years due to their unusually rapid oxygen transport kinetics.^{18,19} This layered perovskite compound has a general formula of $\text{AA}'\text{B}_2\text{O}_{5+\delta}$ where A = trivalent lanthanide ion ($\text{Ln} = \text{Pr}, \text{Nd}, \text{Sm}, \text{ and } \text{Gd}$), $\text{A}' = \text{Ba}$, and B = a first row transition metal ion or a mixture thereof.

The layered perovskite consists of two layers with alternating stacking of $\dots[A'O|BO_2|AO_{\delta}|BO_2]\dots$, and hyperstoichiometric oxygen ions (*i.e.* excess oxygen) are localized at the lanthanide layers.^{20,21}

Among the various types of layered perovskite cathode materials, $GdBaCo_2O_{5+\delta}$ (GBCO) has been found to exhibit a high oxygen surface exchange coefficient and an ionic diffusion at a appropriate temperature range of 773 - 973 K by Tarancón *et al.*²² Furthermore, based on a low thermal expansion coefficient (TEC) of GBCO ($\sim 16 \times 10^{-6} \text{ K}^{-1}$) that is lower than the thermal expansion coefficient (TEC) of other cobaltite cathode materials ($20.5 \times 10^{-6} \text{ K}^{-1}$ for $La_{0.6}SrCoO_{3-\delta}$ or $19.5 \times 10^{-6} \text{ K}^{-1}$ for $Ba_{0.6}Sr_{0.4}Co_{0.2}Fe_{0.8}O_{3-\delta}$), this material has potential for IT-SOFC applications.²³

Meanwhile, several researchers have reported an interesting effect of ion substitution into $LnBaCo_2O_{5+}$. For example, there are some groups that replace the Ba^{2+} site with Sr^{2+} , which improves the electrical and electrochemical performance of the layered perovskite oxide.²⁴⁻²⁶ and other groups also reported beneficial effects on Co replacement.²⁷⁻²⁹

In this study, synergy effects of S site doping and Fe site doping on the A-site and Fe doping on the B-site in a layered perovskite, $GdBaCo_2O_{5+\delta}$, were investigated by structural characterization, thermogravimetric analysis, and electrochemical properties of $GdBa_{0.5}Sr_{0.5}Co_{2-x}Fe_xO_{5+\delta}$ ($x = 0, 0.5, \text{ and } 1.0$). We also optimize the composition of Ce_{0.9}Gd_{0.1}O_{1.95} (GDC) as an electro-catalyst for IT-SOFC cathode material.

2.2 Experimental procedure

GdBa_{0.5}Sr_{0.5}Co_{2-x}Fe_xO_{5+δ} ($x = 0, 0.5, \text{ and } 1.0$) oxides were synthesized by the Pechini method and the glycine-nitrate process (GNP) was used to make fine NiO and Ce_{0.9}Gd_{0.1}O_{1.95} (GDC) to study the electrochemical performance of perovskites. The detailed procedure has been explained elsewhere.²⁶

For evaluation of the structural and electrical properties, GdBa_{0.5}Sr_{0.5}Co_{2-x}Fe_xO_{5+δ} ($x = 0, 0.5, \text{ and } 1.0$) powders were pelletized at 5 MPa and then finally sintered for 12 h at 1373 K ($x = 0$) and 1423 K ($x = 0.5$ and 1.0), respectively, and the relative densities of all samples were over 90%.

Synthesized materials were identified with X-ray diffraction (XRD) patterns (Rigaku-diffractometer, Cu K α radiation) and the XRD data were refined using the Rietveld method with the GSAS program. *In-situ* XRD was also carried out in air within the range of room temperature (RT) to 1073 K (Bruker D8 advance, Cu K α radiation). Chemical compatibility between the GdBa_{0.5}Sr_{0.5}Co_{2-x}Fe_xO_{5+δ} ($x = 0, 0.5, \text{ and } 1.0$) and GDC was evaluated by an XRD analysis of an intimate mixture of 50 wt% GdBa_{0.5}Sr_{0.5}Co_{2-x}Fe_xO_{5+δ} and 50 wt% GDC fired at 1273 K for 4 h. The microstructures of the single cells were investigated by using a field emission scanning electron microscope (SEM) (Nova SEM).

Thermogravimetric analysis (TGA) was performed using an SDT-Q600 (TA instrument, USA) in order to determine the oxygen content as a function of temperature (373 to 1173 K) with a heating/cooling rate of 2 K min⁻¹ in air.

The electrical conductivities of the GdBa_{0.5}Sr_{0.5}Co_{2-x}Fe_xO_{5+δ} oxides were evaluated by a four-terminal DC arrangement with rectangular-shape bars, and each sample was sintered at 1373 K ($x = 0$) and 1423 K ($x = 0.5$ and 1.0). The potentiostat (BioLogic) was used to measure the current and voltage at intervals of 50 K at temperature ranging from 373 K to 1023 K.

To evaluate the electrochemical performance of the GdBa_{0.5}Sr_{0.5}Co_{2-x}Fe_xO_{5+δ} cathodes, GDC and cathode powders were mixed at a weight ratio of 6:4 and ball-milled for 24h. The electrode powders were blended with an organic binder (Heraeus V006) to form slurries.

The electrochemical impedance spectroscopy of GdBa_{0.5}Sr_{0.5}Co_{2-x}Fe_xO_{5+δ} was measured using a symmetric cell. The GDC powders were pelletized and sintered at 1623 K for 4 h in air to obtain the electrolyte substrates. The GdBa_{0.5}Sr_{0.5}Co_{2-x}Fe_xO_{5+δ} cathode slurries were screen-printed onto both sides of GDC electrolytes to form symmetrical cells and the samples were heated at 1173 K for 4 h. The silver wire and paste were used as the current collector for the electrodes. In order to determine the optimized cell performance, electrochemical properties of GdBa_{0.5}Sr_{0.5}CoFeO_{5+δ}- γ GDC ($\gamma = 0, 20, 40, \text{ and } 50$ wt%) cathodes were evaluated. GdBa_{0.5}Sr_{0.5}CoFeO_{5+δ}- γ GDC cathodes were mixed at weight ratios of 10 : 0, 8 : 2, 6 : 4, and 5 : 5, and then ball-milled for 12 h.

The electrochemical performances of GdBa_{0.5}Sr_{0.5}Co_{2-x}Fe_xO_{5+δ} cathodes were evaluated with NiO-GDC anode-supported cells. The cells consist of 3 layers: NiO-GDC as an anode, GDC as an electrolyte, and a cathode. The NiO-GDC cermet anode was fabricated from a mixture of nickel oxide, GDC prepared by GNP, and starch at a weight ratio of 6:4:1.5, and then these mixtures were ball-milled together with ethanol for 24h. A thin GDC

electrolyte on the porous anode (NiO-GDC) support was fabricated by the drop-coating method. The anode-electrolyte layer (NiO-GDC/GDC) disks were subsequently sintered at 1623 K for 5 h. Cathode material slurries were screen-printed onto the electrolyte surface with a uniform thickness, and the single cells consisting 3 layers (NiO-GDC/GDC/GdBa_{0.5}Sr_{0.5}Co_{2-x}Fe_xO_{5+δ}) were subsequently sintered at 1173 K in air for 4 h. Silver wires were then attached at both the cathode and anode surfaces by using silver paste as a current collector. The NiO-GDC anode-supported single cell was sealed fully onto one end of the alumina tube using a ceramic adhesive (Aremco, Ceramabond 552). Humidified H₂ (3% H₂O) was applied to the anode side as a fuel through a water bubbler with a flow rate of 20 mL min⁻¹, while air was supplied as an oxidant to the cathode during the single cell test. The *I-V* curves and impedance spectra were acquired with a BioLogic Potentiostat and analyzed with EC-lab software.

2.3. Results and Discussion

The XRD patterns of the $\text{GdBa}_{0.5}\text{Sr}_{0.5}\text{Co}_{2-x}\text{Fe}_x\text{O}_{5+\delta}$ ($x = 0, 0.5, \text{ and } 1.0$) (GBSCFs) are shown in Figure 8(a). XRD data of GBSCFs show single phase peaks of layered perovskite structures without any secondary phases after sintering at 1373 K for 12 h. As Fe contents increase than $x > 1.0$, the formation of GdFeO_3 secondary phase was observed, indicating the Fe solubility of ~ 1.0 in the $\text{GdBa}_{0.5}\text{Sr}_{0.5}\text{Co}_{2-x}\text{Fe}_x\text{O}_{5+\delta}$ system, thus the investigation for the excessive substitution of Fe was excluded in this study. All samples display a tetragonal structure with the space group $P4/mmm$ confirmed by Rietveld refinement, as presented in Figure 8(b), and the calculated structural parameters of GBSCFs are listed in Table 2. Lattice parameters and cell volumes increase with a higher Fe amount due to the substitution of the larger $\text{Fe}^{3/4+}$ ions into the smaller $\text{Co}^{3/4+}$ ions.²⁷

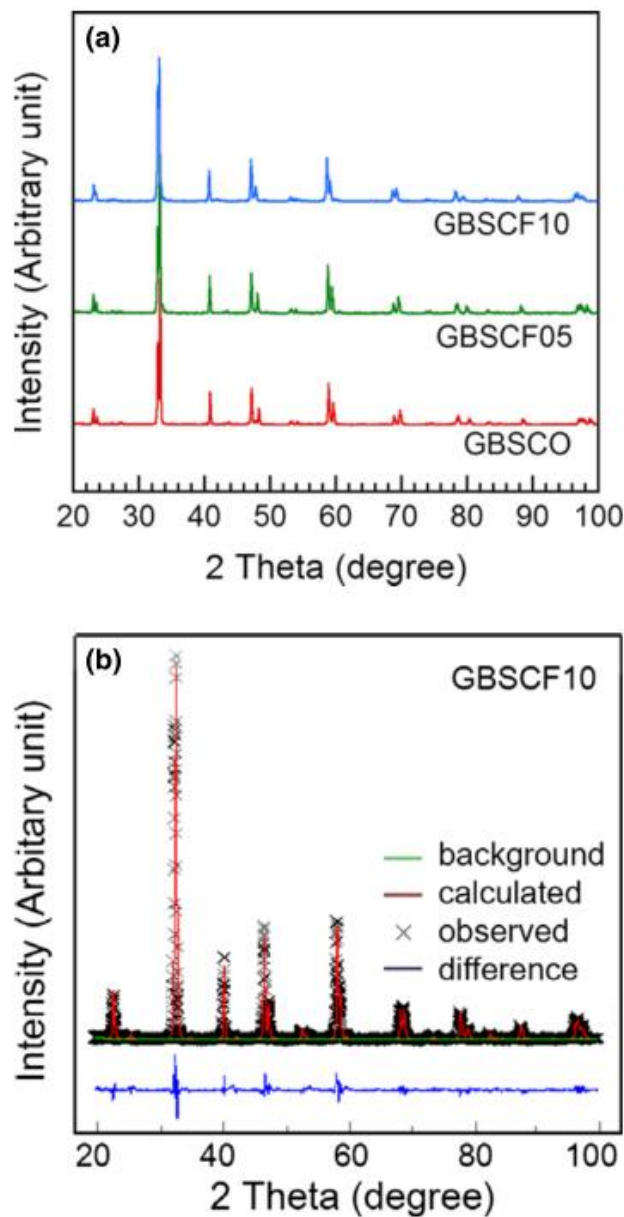


Figure 8. (a) XRD patterns of $\text{GdBa}_{0.5}\text{Sr}_{0.5}\text{Co}_{2-x}\text{Fe}_x\text{O}_{5+\delta}$ ($x = 0, 0.5, \text{ and } 1.0$) sintered at various temperatures, (b) observed and calculated XRD profiles and the difference between them for $\text{GdBa}_{0.5}\text{Sr}_{0.5}\text{CoFeO}_{5+\delta}$

In order to confirm the structural properties at different temperatures (RT to 1073 K), high-temperature XRD measurement is performed in air and presented in Figure 9. The *in-situ* XRD patterns of the GBSCF10 show that the material remained in its layered perovskite structure over the examined temperature range. The main diffraction peaks obviously shift to lower 2 theta with increasing temperature, indicating that the volume of unit cells increased due to the larger size of reduced B-site cation as shown in inset of Figure 9. This behavior is common among other transition metal defect perovskite, including BSCF, LSC and LSCF.

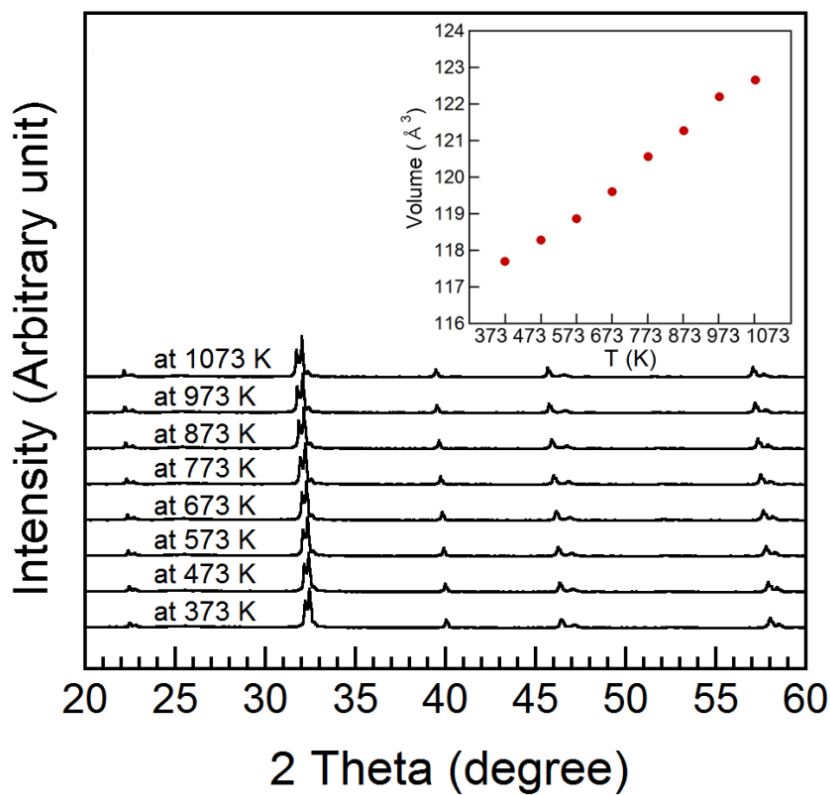


Figure 9 The in-situ XRD patterns of the GdBa_{0.5}Sr_{0.5}CoFeO_{5+δ} at different temperatures at various temperatures. The inset shows the dependence of temperature on unit cell volume V (Å³).

The chemical compatibilities between the GBSCFs and GDC have been confirmed by the XRD measurements. As seen in Figure 10, the characteristic diffraction peaks for the GBSCFs suggest that they have a layered perovskite structure without any detectable secondary phase, which could affect the electrochemical performance.

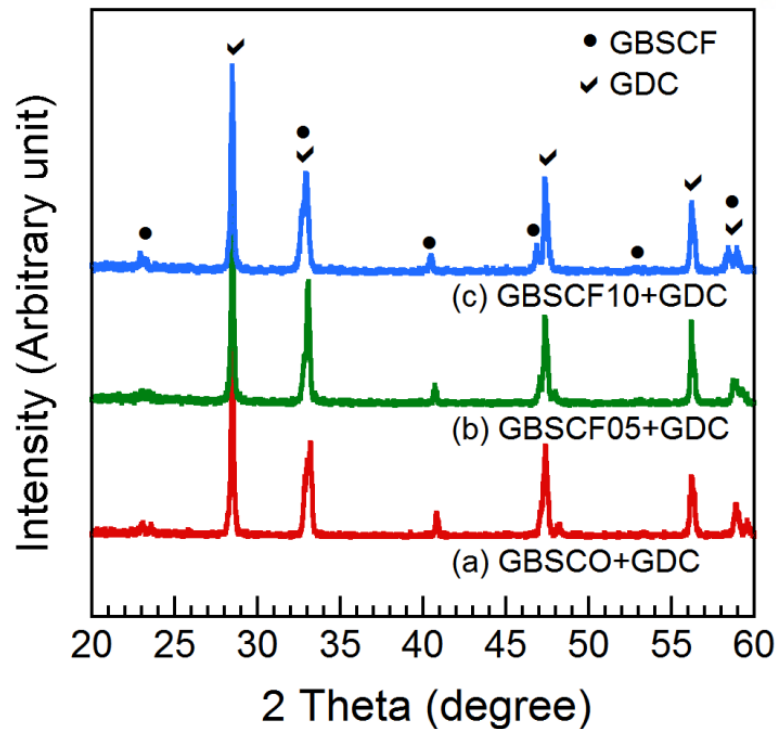


Figure 10 XRD patterns of $\text{GdBa}_{0.5}\text{Sr}_{0.5}\text{Co}_{2-x}\text{Fe}_x\text{O}_{5+\delta}$ ($x = 0, 0.5, \text{ and } 1.0$)–GDC mixture after sintered at 1273 K in air for 4 h.

The microstructures of the $\text{GdBa}_{0.5}\text{Sr}_{0.5}\text{Co}_{2-x}\text{Fe}_x\text{O}_{5+\delta}$ -40GDC have been investigated by SEM, as shown in Figure 11. The electrode microstructure is associated with the surface area, electrochemical active sites, volume fraction of chemical phases present, and electron transport.^{30,31} These properties affect the fuel cell performance through the reaction kinetics, charge transport, and mass transport processes. The microstructures of the porous $\text{GdBa}_{0.5}\text{Sr}_{0.5}\text{Co}_{2-x}\text{Fe}_x\text{O}_{5+\delta}$ -40GDC cathode are similar, and thus the substitution of Fe for Co did not affect the electrochemical active sites, which are related to the cell performance. All of the samples show good adhesion between the cathode and electrolyte with uniform thickness of about 20 μm and 15 μm , respectively.

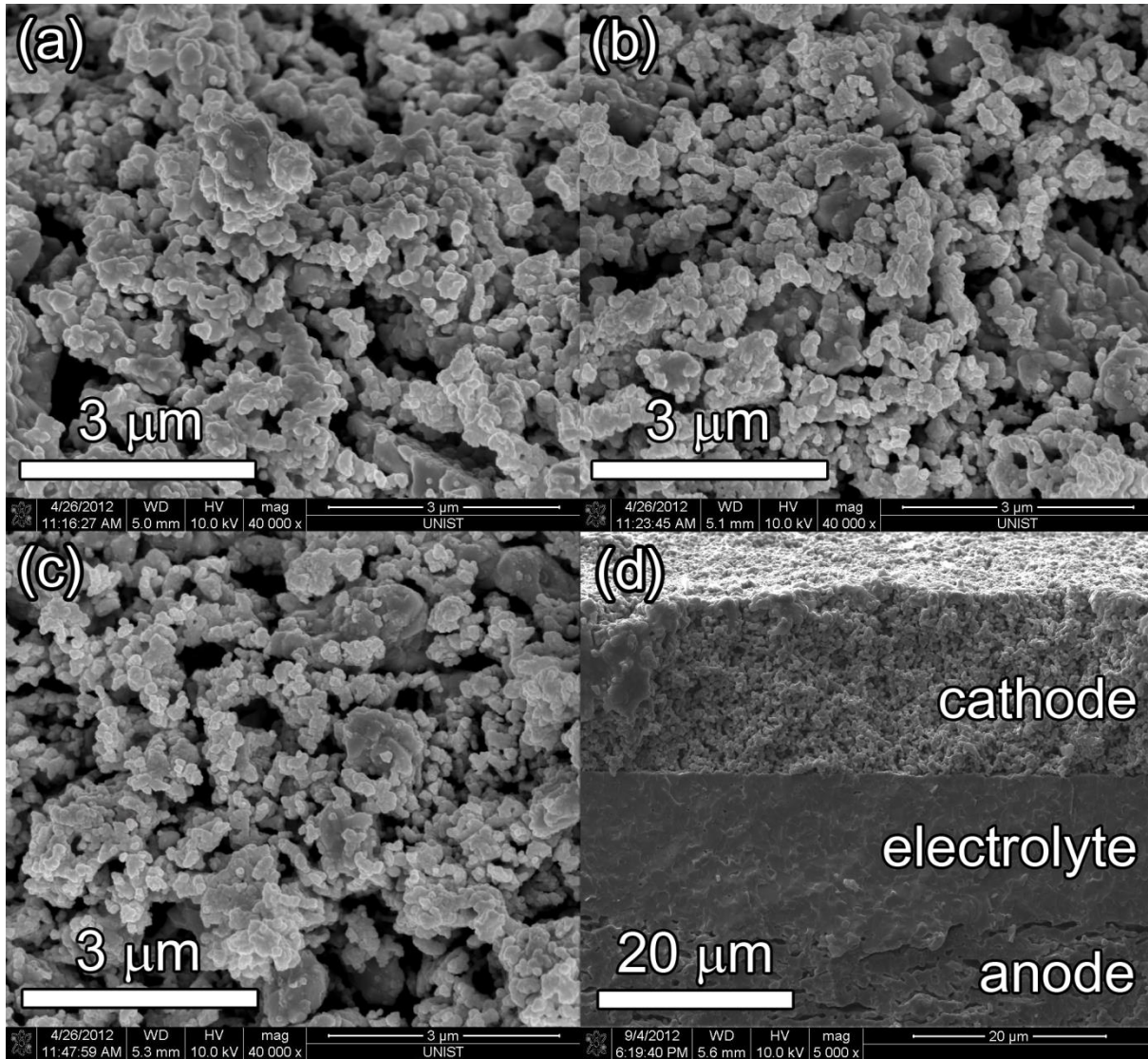


Figure 11 SEM images showing the microstructure of a single cell (GDC - $\text{GdBa}_{0.5}\text{Sr}_{0.5}\text{Co}_{2-x}\text{Fe}_x\text{O}_{5+\delta}$ / GDC / NiO-GDC): (a) $x=0$, (b) $x=0.5$, (c) $x=1.0$, and the cross section of a single cell: (d) $x=1.0$.

Thermogravimetric analysis (TGA) data for the GBSCFs are shown in Figure 12. The GBSCF samples dramatically lose oxygen from the lattice above 573 K with reduction of $\text{Fe}^{3+/4+}$ and $\text{Co}^{3+/4+}$. At given temperature, the oxygen losses decrease with increasing Fe content, because the stronger Fe-O bond compared to the Co-O bond restrains the oxygen loss upon heating.

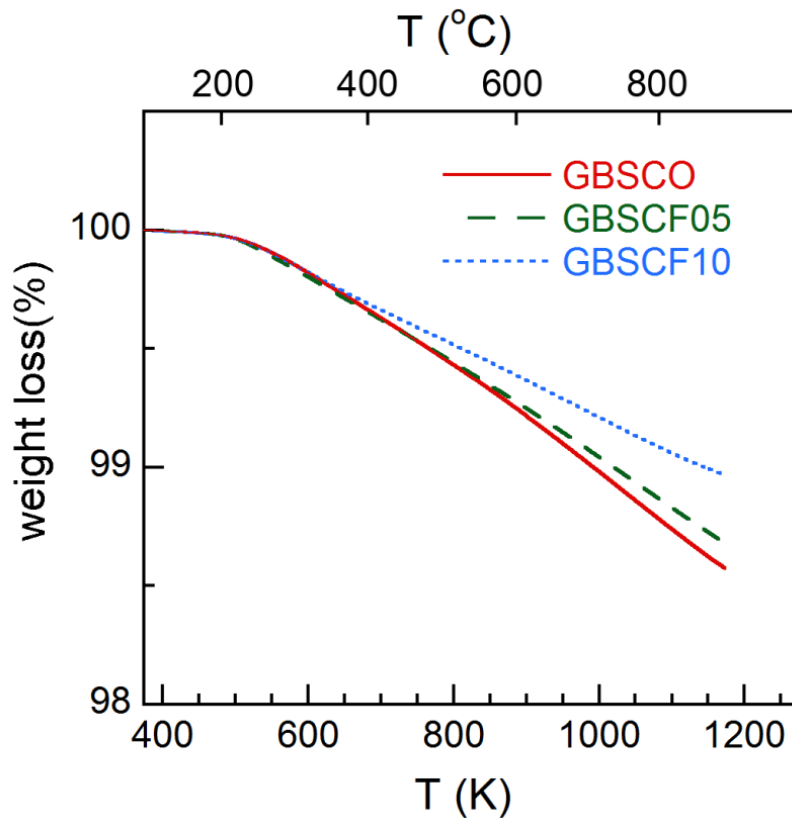


Figure 12 Thermogravimetric data of $\text{GdBa}_{0.5}\text{Sr}_{0.5}\text{Co}_{2-x}\text{Fe}_x\text{O}_{5+\delta}$ ($x = 0, 0.5, \text{ and } 1.0$) showing the variation of oxygen loss (%) as a function of temperature.

The electrical conductivities of the GBSCFs are described by an Arrhenius plot in Figure 13. The electrical conductivity of the Fe-free sample, GBSCO, decreases with increasing temperature, implying typical metallic behavior due to the considerable decrease of charge carrier concentration accompanied by the loss of oxygen. The electrical conductivity of the Fe-substituted samples, however, shows a metal-insulator (M-I) transition at about 573 K due to the low-spin to high-spin transition of Co^{3+} ions.^{32,33} Beyond the M-I transition temperature, 573 K, the electrical conductivity decreases due to increasing loss of oxygen content. At a given temperature, decreasing conductivity of $\text{GdBa}_{0.5}\text{Sr}_{0.5}\text{Co}_{2-x}\text{Fe}_x\text{O}_{5+\delta}$ ($x = 0, 0.5, \text{ and } 1.0$) is observed with increasing Fe content, and this is ascribed to a decrease in the covalency of the (Co-Fe)-O bond. The electrical conductivity is within a range of 600 to 30 S cm^{-1} at 873 K, which is adequate for their use as cathodes in SOFCs.

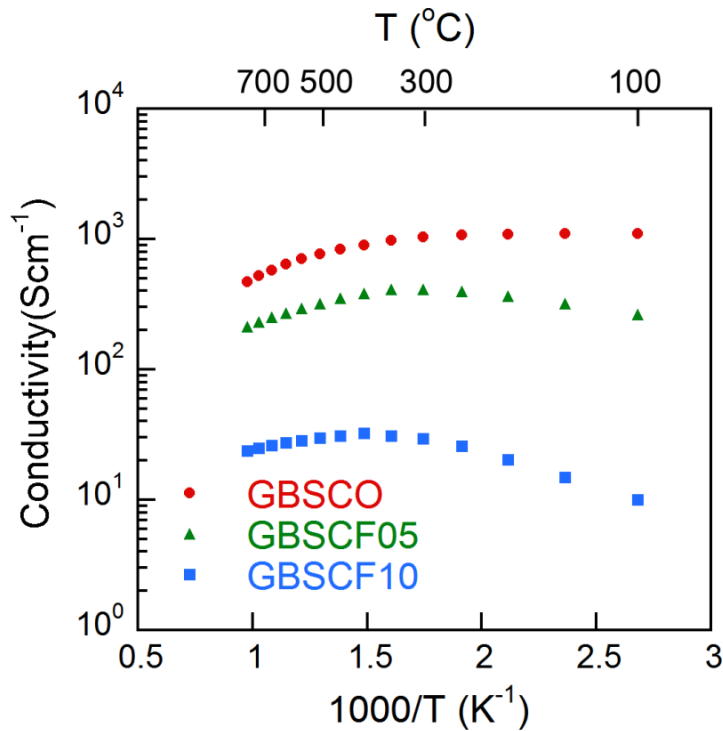
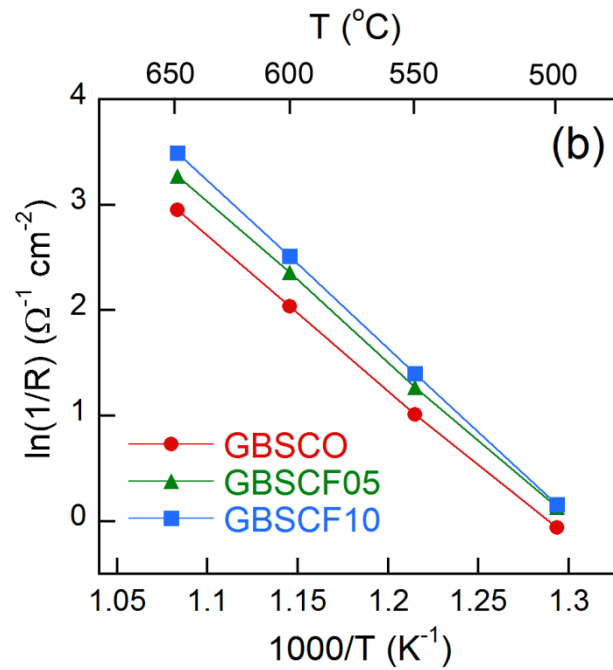
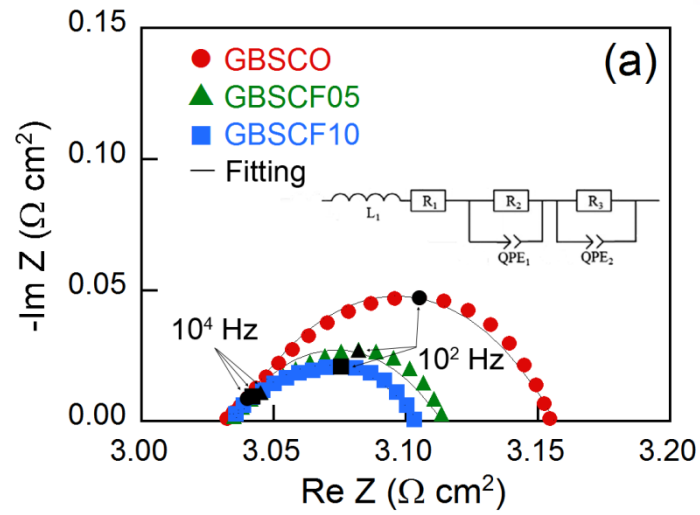


Figure 13 Electrical conductivities of $\text{GdBa}_{0.5}\text{Sr}_{0.5}\text{Co}_{2-x}\text{Fe}_x\text{O}_{5+\delta}$ ($x = 0, 0.5, \text{ and } 1.0$) in a temperature range of 373 to 1023 K in air.

The area specific resistances (ASR) of GBSCF-40GDC are obtained by AC impedance spectroscopy and representative impedance spectra are presented in Figure 14 (a) with curve-fitting using software EC-lab. The ASR is used to describe all resistances associated with the electrode and electrolyte of the cell, and the values are determined by the difference between high-frequency and low-frequency intercepts at the real axis of the Nyquist plot. In the equivalent circuit, L is an inductance induced by the cables; R_1 is ohmic resistance; R_2 is caused by the charge transfer during the migration and diffusion of oxygen ion from the TPBs into electrolyte lattice; R_3 is relative to the non-charge transfer. The polarization resistance (R_p) of the cathode materials is defined by the sum of R_2 and R_3 . The ASR values of the GBSCF-40GDC cathodes are 0.123, 0.095, and 0.067 $\Omega \text{ cm}^2$ at 873 K, for $x = 0, 0.5, \text{ and } 1.0$, respectively. This tendency can be explained as follows.



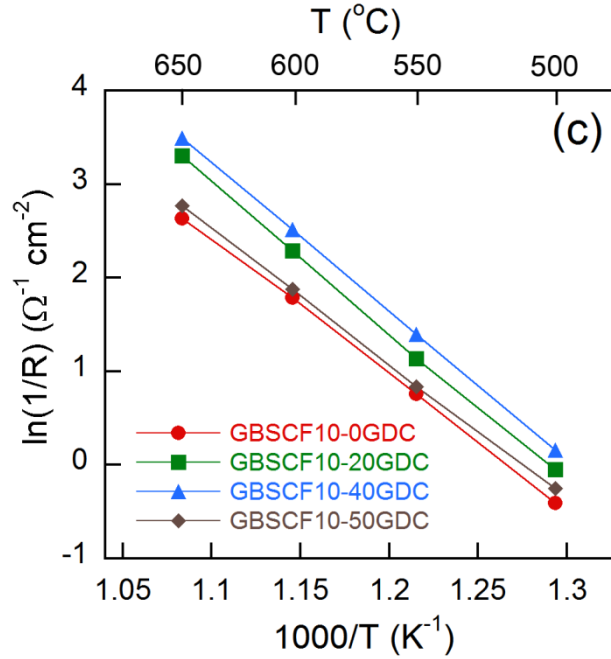


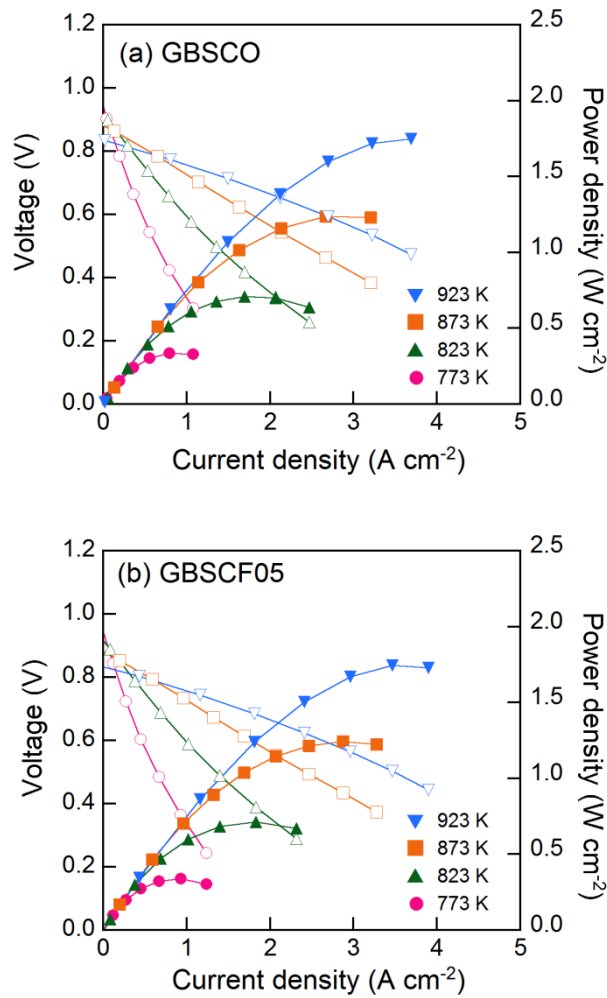
Figure 14 (a) Typical impedance spectra of the symmetrical cells at 873 K, (b) Arrhenius plots of the ASRs for $\text{GdBa}_{0.5}\text{Sr}_{0.5}\text{Co}_{2-x}\text{Fe}_x\text{O}_{5+\delta}$ ($x = 0, 0.5, \text{ and } 1.0$), and (c) GBSCF10- y GDC ($y = 0, 20, 40, \text{ and } 50$ wt%) symmetrical cells.

Generally, the defects of oxygen ions contain useful information about the mechanism of oxygen ion diffusion.³⁴ For example, studying a layered perovskite structure system, Taskin *et al.* reported that the hyperstoichiometric oxygen species in the Ln-O layer could be responsible for the high diffusivity of oxide ions, because the Ln-O layer provides a disorder-free channel as the oxygen bonding strength in this layer is reduced. Interestingly, the electrochemical performance tended to improve with greater hyperstoichiometric oxygen content (δ), and this study has also shown that the ASR is reduced with higher oxygen content (Figure 12 and Figure 14). These phenomena might be evidence that a larger concentration of hyperstoichiometric oxygen ions has a positive influence on the oxygen ion diffusivity for the layered perovskite materials. Further research is thus needed to establish the oxygen ion diffusion mechanism of layered perovskites, next generation cathode materials.

Meanwhile, it has been extensively documented that there exists an optimum composition of GDC as an electrocatalyst within cathode materials that can maximize the electrocatalytic activity of the cathodes due to extension of the triple phase boundaries (TPBs). To determine the optimized ratio of GDC, ASR values of $\text{GdBa}_{0.5}\text{Sr}_{0.5}\text{CoFeO}_{5+\delta-y}\text{GDC}$ ($y = 0, 20, 40, \text{ and } 50$ wt%) composites were obtained and the results are presented in Figure 14(c) as an Arrhenius plot. As expected, the ASR values decreased with an increasing amount of GDC up to 40 wt%. For an excessive amount of GDC beyond 40 wt%, however, the ASR values increase. This indicates that an overly large amount of GDC particles reduces the continuity of GBSCF10 in the composites, thereby resulting in a decrease of effective electron-conducting paths in the electrode. Therefore,

GdBa_{0.5}Sr_{0.5}CoFeO_{5+δ}-40GDC was selected as an optimum cathode material composition.

Figure 15 shows the current-voltage (*I-V*) curves and corresponding power density curves obtained with configuration of GdBa_{0.5}Sr_{0.5}Co_{2-x}Fe_xO_{5+δ} (*x* = 0, 0.5, and 1.0)-40GDC/GDC/NiO-GDC single cell at various temperatures. As expected from the lowest ASR value for GBSCF10, the maximum power density of GBSCF10 was 1.31 Wcm⁻² at 873 K, and other samples also showed high power density over 1.00 W cm⁻².



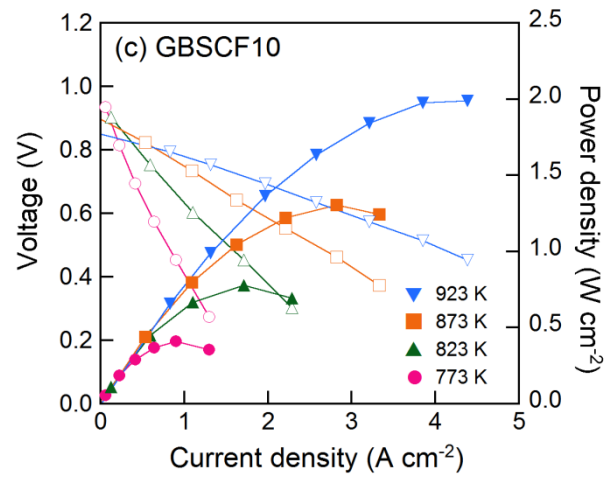


Figure 15 I - V curves and corresponding power density curves of single cells ($\text{GdBa}_{0.5}\text{Sr}_{0.5}\text{Co}_{2-x}\text{Fe}_x\text{O}_{5+\delta}/\text{GDC}/\text{NiO-GDC}$) under various temperatures: (a) $x = 0$, (b) $x = 0.5$, and (c) $x = 1.0$.

2.4. Conclusion

GdBa_{0.5}Sr_{0.5}Co_{2-x}Fe_xO_{5+δ} layered perovskite oxides have been studied as a promising cathode material for IT-SOFCs. GdBa_{0.5}Sr_{0.5}Co_{2-x}Fe_xO_{5+δ} powders were prepared by the Pechini method and glycine-nitrate-process (GNP). The electrical conductivity decreased with increasing Fe content from 700 Scm⁻¹ to 30 Scm⁻¹ at 873 K, which is high enough to meet the requirement for use as an IT-SOFC cathode. In the microstructural analysis, no particular differences were observed between GBSCFs with various amounts of Fe by SEM. The oxygen loss of GdBa_{0.5}Sr_{0.5}Co_{2-x}Fe_xO_{5+δ} at 873 K decreased with increasing amount of Fe. The ASR of GdBa_{0.5}Sr_{0.5}Co_{2-x}Fe_xO_{5+δ} decreased with Fe content and the optimized GdBa_{0.5}Sr_{0.5}CoFeO_{5+δ}-40GDC cathode material had the lowest ASR of 0.067 Ω cm² at 873 K, and consequently exhibited remarkable cell performance of 1.31 Wcm⁻² at 873 K.

Chapter 3. Chemically Stable Perovskites as Cathode Materials for Solid Oxide Fuel Cells: La-Doped $\text{Ba}_{0.5}\text{Sr}_{0.5}\text{Co}_{0.8}\text{Fe}_{0.2}\text{O}_{3-\delta}$

$\text{Ba}_{0.5}\text{Sr}_{0.5}\text{Co}_{0.8}\text{Fe}_{0.2}\text{O}_{3-\delta}$ (BSCF) has won tremendous attention as an IT-SOFC cathode material on the basis of its fast oxygen-ion transport properties. Nevertheless, wide application of BSCF is definitely impeded by its phase instabilities at intermediate temperature. Here we report on a chemically stable SOFC cathode material, $\text{La}_{0.5}\text{Ba}_{0.25}\text{Sr}_{0.25}\text{Co}_{0.8}\text{Fe}_{0.2}\text{O}_{3-\delta}$ (LBSCF), prepared by strategic approaches using the Goldschmidt tolerance factor. The tolerance factors of LBSCF and BSCF indicate that the structure of the former has a smaller deformation of cubic symmetry than that of the latter. The electrical property and electrochemical performance of LBSCF are improved compared with those of BSCF. LBSCF shows also excellent chemical stability under air, a CO_2 -containing atmosphere, and low $p(\text{O}_2)$ while BSCF decomposed under the same conditions. Together with this excellent stability, LBSCF shows a power density of 0.81 W cm^{-2} for 100 h, whereas 25 % degradation for BSCF is observed after 100 h.

This chapter has been published.

Reproduced with permission from Kim, J., *et al.*, Chemically Stable Perovskites as Cathode Materials for Solid Oxide Fuel Cells: La-Doped $\text{Ba}_{0.5}\text{Sr}_{0.5}\text{Co}_{0.8}\text{Fe}_{0.2}\text{O}_{3-\delta}$, Chemsuschem, 7, 669 (2014). Copyright 2014. Chemsuschem, Wiley.

3.1. Introduction

With exponential growth of energy consumption and finite fossil fuel resources, awareness of the necessity of high efficiency energy conversion devices is increasing. Solid oxide fuel cells (SOFCs) are considered an answer to the needs of the times, by providing high energy conversion efficiency, efficient reclamation of waste heat, low pollutant emissions, and extensive fuel flexibility. The high operating temperature (1073-1273 K) of SOFCs, however, is an obstacle to their commercialization, mainly due to related corrosion, chemical interdiffusion, reactions between components, and high thermal stress. In recent years, research aimed at lowering the working temperature of SOFCs down to an intermediate temperature (IT) range, 773 – 973 K, has been actively carried out.

Fuel cell operation at intermediate temperature, however, leads to serious problems, including a drop of the electro-catalytic activity for the oxygen reduction reaction (ORR) over the cathode.¹⁶ To overcome electro-catalytic issues, mixed ionic and electronic conductors (MIECs) such as $\text{La}_{0.6}\text{Sr}_{0.4}\text{CoO}_{3-\delta}$, $\text{Sm}_{0.5}\text{Sr}_{0.5}\text{CoO}_{3-\delta}$, $\text{La}_{0.6}\text{Sr}_{0.4}\text{Co}_{0.2}\text{Fe}_{0.8}\text{O}_{3-\delta}$, and cation-ordered $\text{LnBaCo}_2\text{O}_{5+\delta}$ ($\text{Ln} = \text{Pr, Nd, Sm, Gd and Y}$) have been adopted as cathode materials with consideration of their excellent catalytic activities for the oxygen reduction reaction (ORR).^{11]} Among these MIEC materials, $\text{Ba}_{0.5}\text{Sr}_{0.5}\text{Co}_{0.8}\text{Fe}_{0.2}\text{O}_{3-\delta}$ (BSCF) has received tremendous attention for its fast oxygen-ion transport properties.^{35,36}

Nevertheless, wide application of BSCF has been inhibited by its structural instabilities at intermediate

temperature. For example, Shao *et al.* showed that exponential decay in the measured oxygen permeation flux of BSCF occurs at temperature below 1098 K.³⁷ Several groups have revealed that this degradation of BSCF results from a phase transition from a cubic structure into a two-phase mixture of hexagonal and cubic perovskites.^{38,39}

The structural instability of cubic BSCF can be rationalized using the Goldschmidt tolerance factor (t_f), which is a useful indicator for the stability and distortion of crystal structures. To keep the cubic structure stable, the t_f can be controlled near to 1 by doping proper size materials as schematically shown in Figure 16.⁴⁰ For BSCF, its t_f value is 1.052, implying that its structure tends to change into the hexagonal phase. Fortunately, the t_f of BSCF can be rendered closer to 1 by substituting smaller ions into the A-site and/or larger ions into the B-site.⁴¹

Among possible dopants, our group found that substituting smaller La^{3+} compared to Ba^{2+} and Sr^{2+} can mitigate the tolerance factor and La^{3+} doped BSCF is thereby stable in the cubic perovskite phase. In addition, according to Hayashi *et al.*, relaxation of distortion could contribute to enhanced ionic conductivity by reducing the local strain in the lattice.⁴²

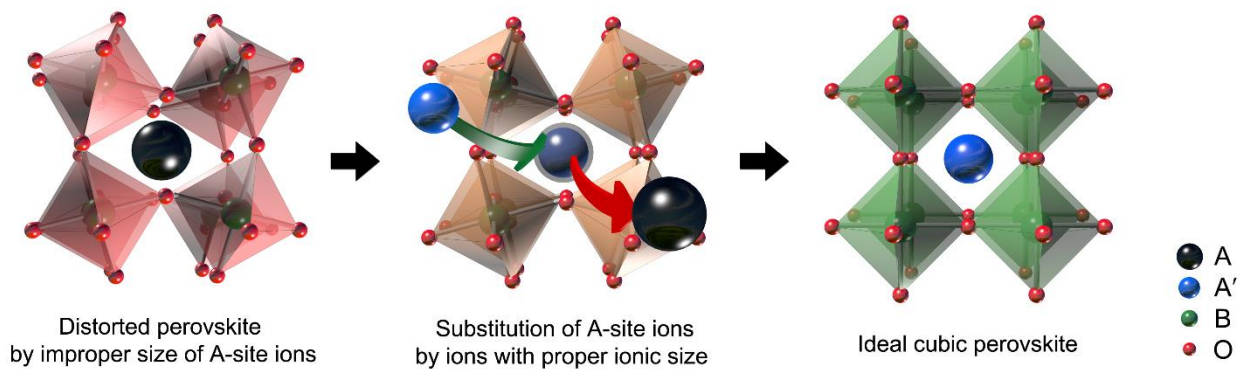


Figure 16 Schematic illustration of the perovskite structure state as a function of ionic size

Here we demonstrate a strategic approach based on La^{3+} doping into the A-site of BSCF, providing high oxygen reduction activity and excellent structural stability at intermediate temperature operation. A systematic evaluation of the structural, thermogravimetric, electrical, and electrochemical properties of LBSCF has been carried out.

3.2. Experimental Section

Synthesis of electrode and electrolyte powders

$\text{Ba}_{0.5}\text{Sr}_{0.5}\text{Co}_{0.8}\text{Fe}_{0.2}\text{O}_{3-\delta}$ (BSCF) and $\text{La}_{0.5}\text{Ba}_{0.25}\text{Sr}_{0.25}\text{Co}_{0.8}\text{Fe}_{0.2}\text{O}_{3-\delta}$ (LBSCF) were synthesized using the Pechini method. Stoichiometric amounts of $\text{La}(\text{NO}_3)_3 \cdot 6\text{H}_2\text{O}$ (Aldrich, 99.9 %, metal basis), $\text{Ba}(\text{NO}_3)_2$ (Aldrich, 99+ %), $\text{Sr}(\text{NO}_3)_2$ (Aldrich, 99+ %), $\text{Co}(\text{NO}_3)_2 \cdot 6\text{H}_2\text{O}$ (Aldrich, 98+ %), and $\text{Fe}(\text{NO}_3)_3 \cdot 6\text{H}_2\text{O}$ (Aldrich, 98%) were dissolved in distilled water with proper amounts of citric acid and ethylene glycol. The solutions were heated in air followed by combustion to form fine powders, which were calcinated at 873 K for 4 h. For measurement of electrical conductivity and coulometric titration, the BSCF and LBSCF powders were pressed into pellets at 5 MPa and sintered in air at 1473 and 1423 K, respectively, for 12 h (to achieve relative density, 97%). $\text{Ce}_{0.9}\text{Gd}_{0.1}\text{O}_{2-x}$

(GDC) powders for the electrolyte and NiO-GDC powders for the anode were synthesized using the GNP method; the detailed procedure has been described elsewhere.^[21] For preparation of cathode slurries, pre-sintered cathode and GDC powders (at a weight ratio of 60:40) were mixed via ball milling, together with an organic binder (Heraeus V006), and composite cathodes with 40 wt% GDC, denoted as BSCF-40GDC and LBSCF-40GDC, were obtained.

Fabrication of fuel cells

Symmetrical cells with a configuration of electrode/GDC/electrode were used for impedance spectroscopy. GDC powder was pressed into pellets of 0.8 mm thickness and sintered at 1623 K for 4 h in air to obtain a dense electrolyte membrane. The cathode slurries were screen-printed onto both sides of the GDC electrolytes to form symmetrical cells and the samples were heated at 1273 K for 4 h. Silver wire and paste were used as the current collector for the electrodes.

Ni-GDC anode-supported cells with a configuration of Ni-GDC/GDC/cathode were fabricated using a drop-coating method. NiO powder, GDC powder, and starch (weight ratio of 6:4:1.5) were mixed using ball milling in ethanol for 24 h. After drying, the NiO-GDC mixture was pressed into a pellet (0.6 mm thick and 15 mm diameter). Thin GDC electrolyte membranes were prepared by a refined particle suspension coating technique. A GDC suspension was prepared by dispersing GDC powder (Aldrich) in ethanol with a small amount of binder (polyvinyl Butyral, B-98) and dispersant (Triethanolamine, Alfa Aesar) at a ratio of 1:10. The GDC suspension was applied to a NiO-GDC anode support by drop-coating, followed by drying in air and subsequent co-sintering at 1673 K for 5 h.

Characterizations

Synthesized materials were confirmed with X-ray diffraction (XRD) patterns (Rigaku-diffractometer, Cu Ka radiation) and the XRD data were refined using the Rietveld method with the GSAS program. A thermogravimetric analysis (TGA) was performed using a SDT-Q600 (TA Instruments, USA). TGA experiments were performed from 373 K to 1173 K with a heating/cooling rate of 2 K min⁻¹ in air. The room-temperature oxygen content values were determined by iodometric titration. The microstructures and morphologies of the single cells were observed using a field emission scanning electron microscope (SEM) (Nova SEM). Transmission electron microscopy (TEM) images were acquired with a JEOL JEM 2100F with a probe forming

(STEM) Cs corrector at 200 kV. Cross sectional samples for TEM analysis were prepared using a focused ion beam (FIB, Quanta 3D, FEI). Electrical conductivities of the BSCF and LBSCF cathode materials were determined in air using a four-electrode DC arrangement with rectangular-shape bars. All four electrodes were made of Ag wire and Ag paste. A potentiostat (BioLogic) was used to measure the current and voltage at intervals of 50 K at temperature ranging from 373 K to 1023 K.

To evaluate the electrochemical performance of symmetrical cells, the Ag wire and Ag paste were used as the current collector for the electrodes. Impedance spectra were recorded under OCV in a frequency range of 1 mHz to 500 kHz with ac perturbation of 14 mV in a temperature range of 773 - 923 K.

For the single cell tests, silver wires were attached at the cathode side using Ag paste and Pt wires were attached at the anode side using Ni-O paste as a current collector. The NiO-GDC anode-supported single cell was fully sealed onto one end of the alumina tube using a ceramic adhesive (Aremco, Ceramabond 552). Humidified H₂ (3% H₂O) was applied to the anode side as a fuel thorough a water bubbler with a flow rate of 100 mL min⁻¹, while air was supplied as an oxidant to the cathode during the single cell test. *I-V* polarization curves were recorded between 773 and 923 K. The *I-V* curves and impedance spectra were acquired with a BioLogic potentiostat and analyzed with EC-lab software.

The redox properties and oxygen nonstoichiometry of the cathodes were identified using coulometric titration (CT) as a function of the oxygen partial pressure, $p(\text{O}_2)$. The detailed CT procedure has been described elsewhere.⁴³ After purging 5 % O₂-Ar gas over the sample in the tube for 24 h, $p(\text{O}_2)$ was evaluated from the OCV. The sample was allowed to equilibrate with the surrounding atmosphere until the change in potential was less than 1 mV h⁻¹. Oxygen nonstoichiometry was determined through this procedure at 973 K over a wide range of oxygen partial pressure. Electrical conductivity was measured using a four-electrode configuration and a BioLogic potentiostat.

3.3. Results and Discussion

The XRD patterns of the BSCF and LBSCF samples are presented in Figure 17a. All of the observed diffraction patterns are identified as perovskite structures without any impurities. The main diffraction peaks of the LBSCF obviously shift toward larger 2 theta compared with those of the BSCF due to the substitution of smaller La^{3+} cation for A-sites. In order to identify the structural properties of the LBSCF sample, Rietveld refinement of the LBSCF was performed by the GSAS program and the results are shown in Figure 17b. LBSCF could be indexed to a cubic structure, having a space group $Pm-3m$ with $a=3.8741 \text{ \AA}$, while the lattice parameter of BSCF shows a higher value, 3.9511 \AA with the space group $Pm-3m$.⁴⁴

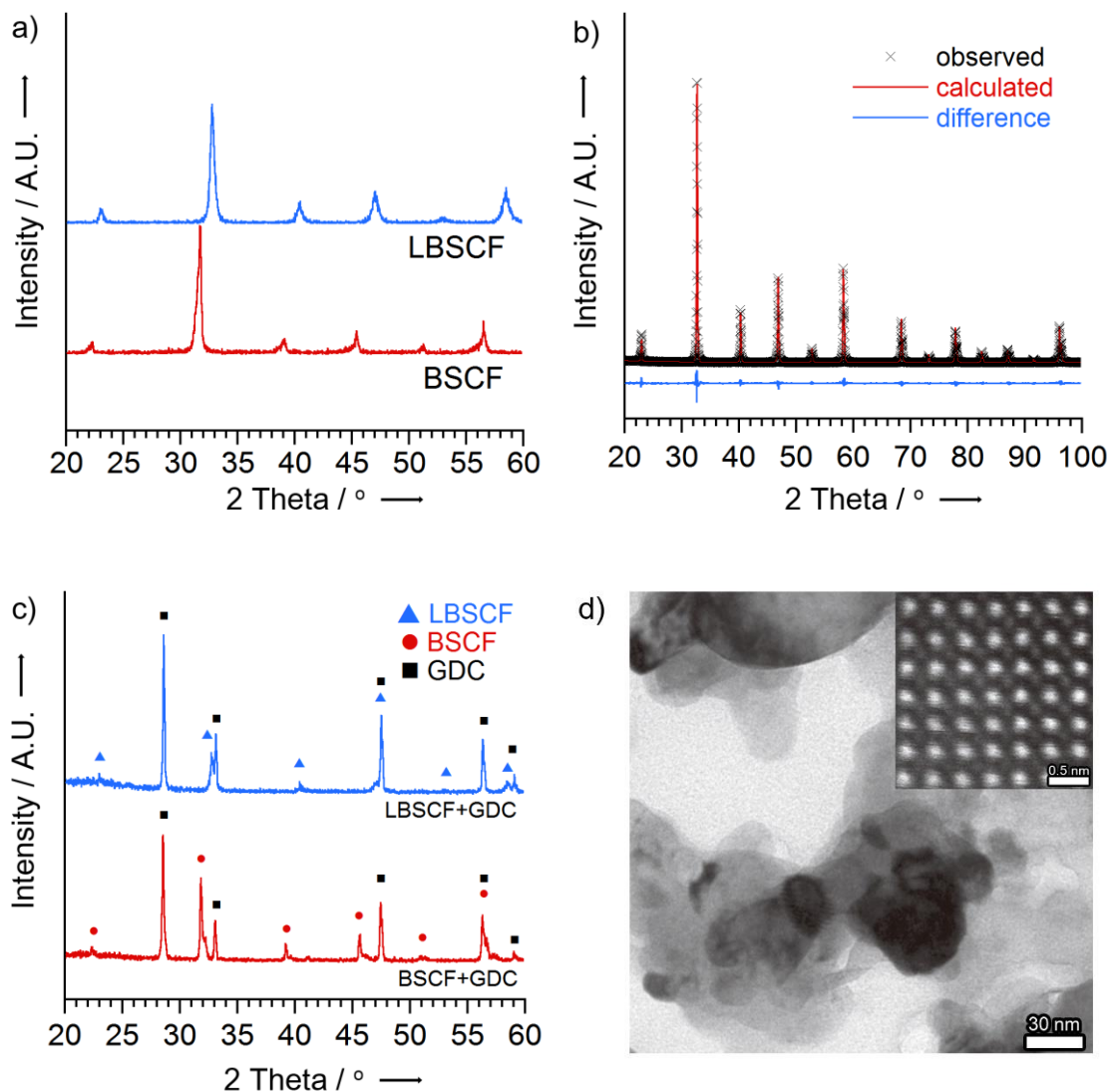


Figure 17 a) XRD patterns of the BSCF and LBSCF sintered at 1473K and 1423K, respectively for 12h. b) Observed, calculated XRD profiles and the difference between them for LBSCF. c) XRD patterns of cathode-GDC mixture sintered at 1273 K in air for 4 h. d) Bright-field (BF) TEM image of LBSCF-GDC cathode sintered at 1273K in air for 4h. Inset shows atomic-scale scanning TEM (STEM) high-angle annular dark-field (HAADF) image of LBSCF.

The chemical compatibility between the cathode materials and GDC electrolyte was evaluated using a mixture of corresponding powders (1:1 wt% ratio) fired at 1273 K for 4h. As shown in Figure 17c, XRD spectra indicate the individual phases of the BSCF, LBSCF, and GDC without formation of secondary phases. Transmission electron microscopy (TEM) images of the sintered LBSCF-GDC composite cathode are presented in Figure 17d. The atomic-resolution Scanning TEM (STEM) high-angle annular dark-field (HAADF) image of LBSCF in the inset of Figure 2d shows even A-site contrast, indicating that a disordered perovskite structure is successfully synthesized in the composite cathode.

The temperature dependence of the oxygen non-stoichiometry for BSCF and LBSCF is examined by TGA and the results are shown in Figure 18. The oxygen contents of the BSCF and LBSCF at room temperature were measured by the iodometry titration method. In the whole range of temperature, the oxygen concentration of the LBSCF is higher than that of the BSCF and both samples start to lose weight at around 573 K. McIntosh *et al.* suggested that the unusual low oxygen concentration of BSCF could be derived from its large A-O and B-O bond distances.⁴⁵ On the contrary, with a decrease of the average effective radii of A-site ions by substituting smaller La^{3+} ions (1.36 Å) into A-site ions (1.61 Å for Ba^{2+} and 1.44 Å for Sr^{2+}), LBSCF can accommodate more oxygen ions in the lattice.

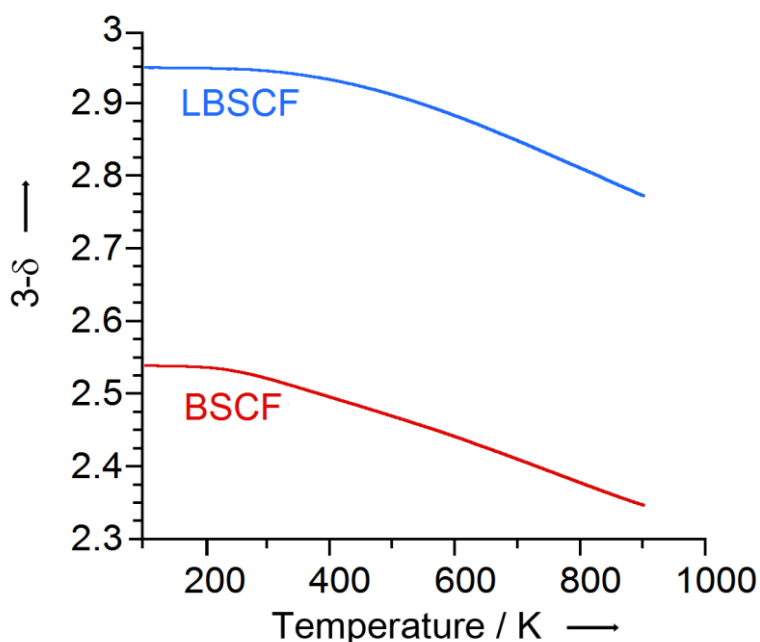


Figure 18 Thermogravimetric data of the BSCF and LBSCF presenting a variation of oxygen contents as a function of temperature in air.

The electrical conductivities of the BSCF and LBSCF samples are described by Arrhenius plots in Figure 19.

At a given temperature, the electrical conductivity of the LBSCF is much higher (900 S cm^{-1} at 873 K) than that of the BSCF (15 S cm^{-1} at 873 K). This could be ascribed to an increase of hole concentration by La doping into the BSCF, as anticipated from the TGA data and following Kröger–Vink notation.⁴⁶ In addition, the relaxation of structural distortion by La^{3+} doping into BSCF could affect the electrical conductivity.⁴² The electrical conductivity of the LBSCF sample decreases upon heating due to a loss of the oxygen from the lattice. The electrical conductivity of the BSCF sample meanwhile shows similar behavior to that of other previous perovskite materials.⁴⁷

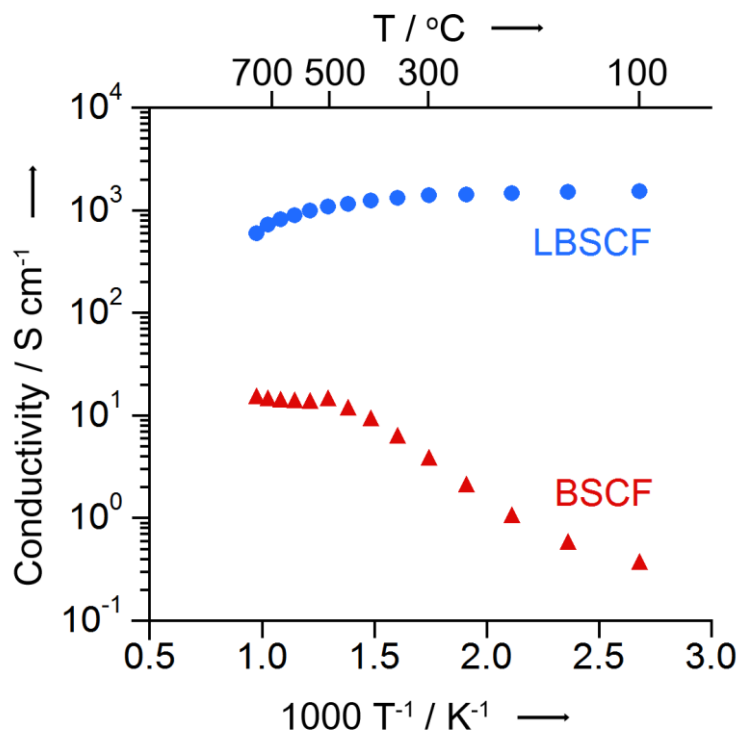


Figure 19 Electrical conductivity data for the BSCF^[24] and LBSCF as a function of temperature in air.

The morphologies of the BSCF-40GDC and LBSCF-40GDC composite cathodes were investigated using SEM. As seen in Figure 20, the LBSCF-40GDC cathode shows considerably smaller particle size than the BSCF-40GDC cathode. Generally, electrode microstructure is associated with electrochemically active sites, volume fraction of chemical phases present, and electron transport paths, which can affect the fuel cell performance through the electrochemical kinetics. Taking these factors into consideration, the smaller particle size of LBSCF could improve the performance by expanding electrochemically active sites such as triple phase boundaries (TPBs). All of the samples show good adhesion between the cathode and electrolyte. The thickness of the cathode and electrolyte is about $20 \mu\text{m}$ and $15 \mu\text{m}$, respectively.

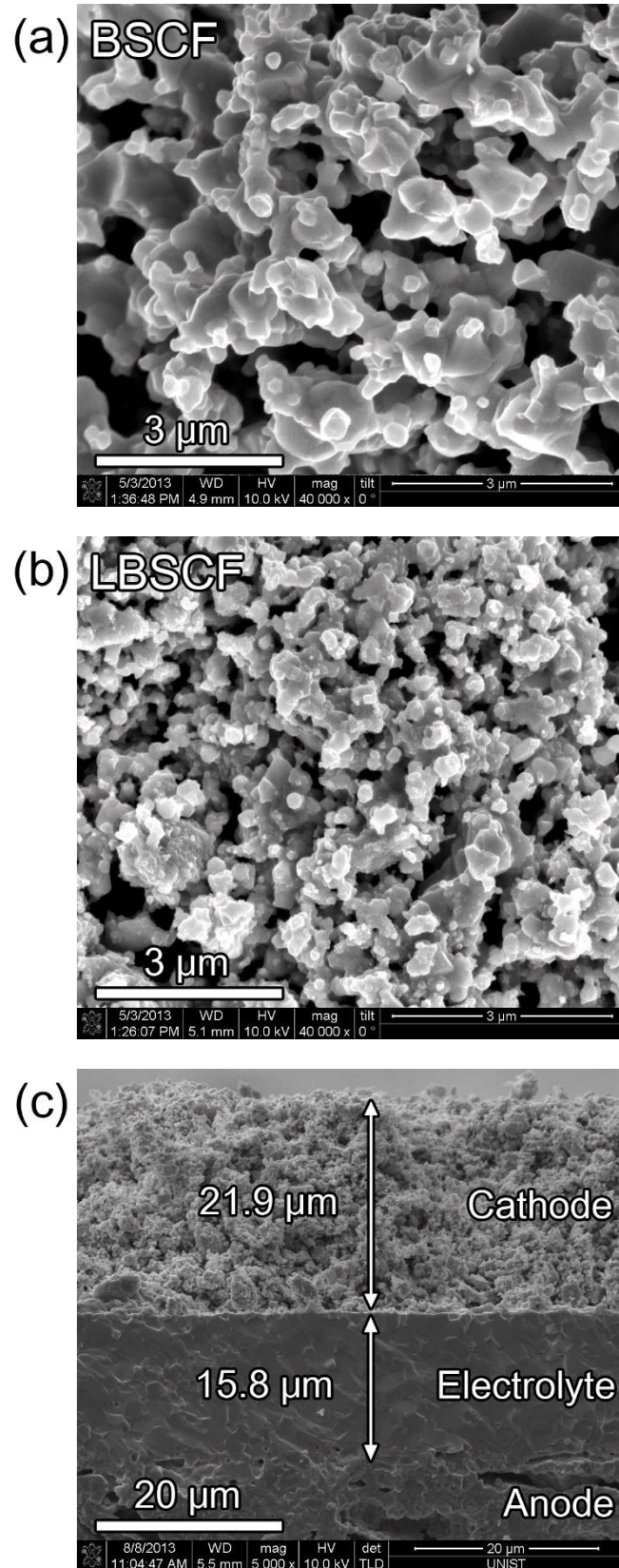


Figure 20 Scanning electron microscope image of porous a) BSCF-40GDC, b) LBSCF-40GDC composite and c) cross-section of LBSCF-40GDC/GDC/NiO-GDC single cell.

The area specific resistances (ASR) of BSCF-40GDC and LBSCF-40GDC were evaluated by AC impedance

spectroscopy and the results are presented in Figure 21a with curve-fitting using EC-lab software. The ASR is used to describe all resistances associated with the electrode and electrolyte of the cell, and the values are determined by the difference between high-frequency and low-frequency intercepts at the real axis of the Nyquist plot. In the equivalent circuit, L is the inductance induced by the cables; R_1 is ohmic resistance; R_2 is caused by charge transfer during the migration and diffusion of oxygen ions from the TPBs into the electrolyte lattice; and R_3 is related to non-charge transfer such as oxygen surface exchange and gas-diffusion inside and outside the electrode layer. The polarization resistance (R_p) of the cathode materials is defined by the sum of R_2 and R_3 . LBSCF shows relatively lower ASR values compared to BSCF; $0.064 \Omega \text{ cm}^2$ and $0.091 \Omega \text{ cm}^2$, respectively, at 873 K. This could be explained as follows. First, as can be seen in Figure 21, the smaller particle size of LBSCF relative to that of BSCF could expand the TPBs, which can affect the electrochemical performance by promoting ORRs. In addition, according to Dusastre *et al.* and Wu *et al.*, the ambipolar conductivity of MIECs characterizes the simultaneous transport properties of both electronic and ionic species. In this regard, the significant enhancement of the electrical conductivity by La^{3+} doping into BSCF could increase the ambipolar conductivity, leading to improved electrochemical performance.^{17,48,49} As seen in Figure 21b, LBSCF-40GDC shows lower ASR values compared to BSCF in an intermediate temperature range of 773 – 923 K.

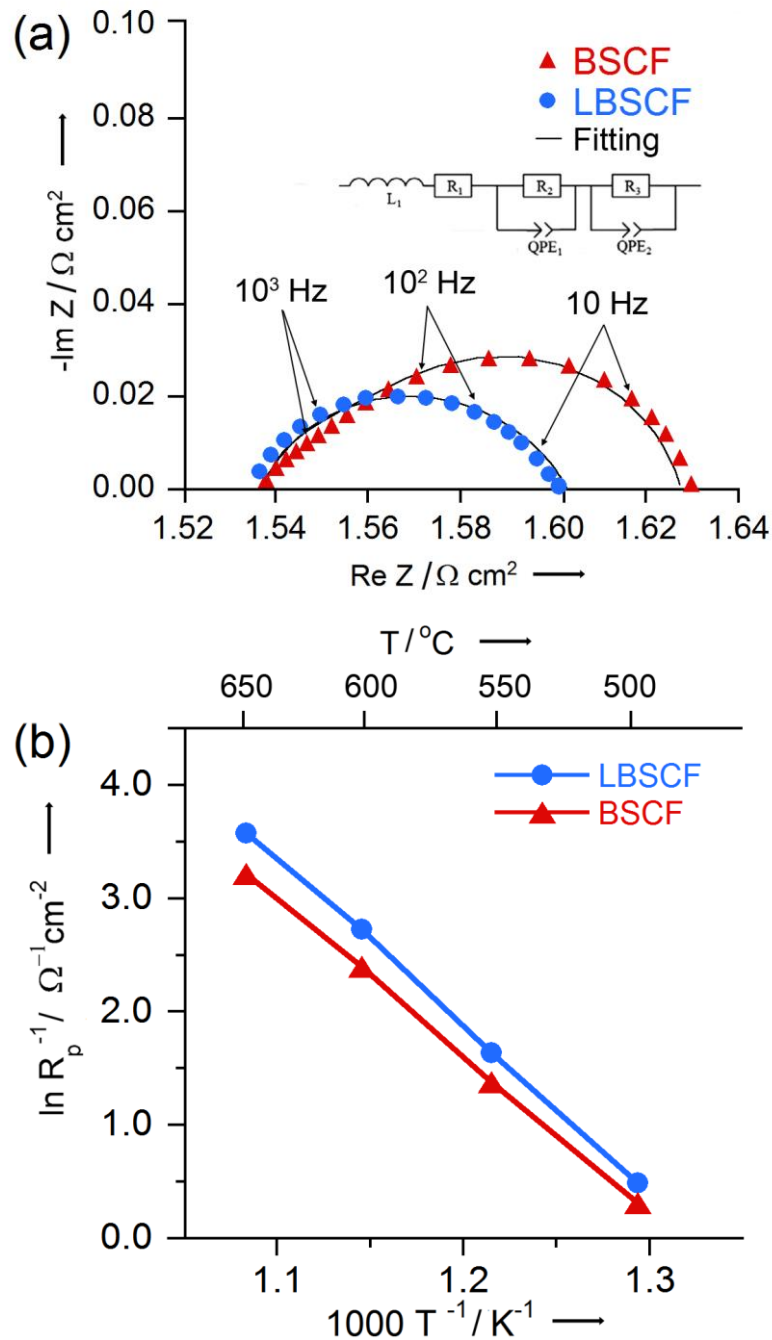


Figure 21 a) Impedance spectra and fitted Nyquist plots with BSCF-40GDC and LBSCF-40GDC composite cathode on symmetrical cell measured at 873 K under OCV condition. b) Arrhenius plot of polarization resistance for BSCF-40GDC and LBSCF-40GDC composite cathode.

Figure 22 presents the current-voltage (I - V) curves and corresponding power density curves obtained with the configuration of BSCF-GDC/GDC/NiO-GDC and LBSCF-GDC/GDC/NiO-GDC single cell at various temperatures. As expected from the lower ASR values for LBSCF, there are considerable enhancements in electrochemical performance of LBSCF compared to BSCF, and values of the maximum power density are 1.77 and 1.48 W cm^{-2} for LBSCF and BSCF at 873 K, respectively.

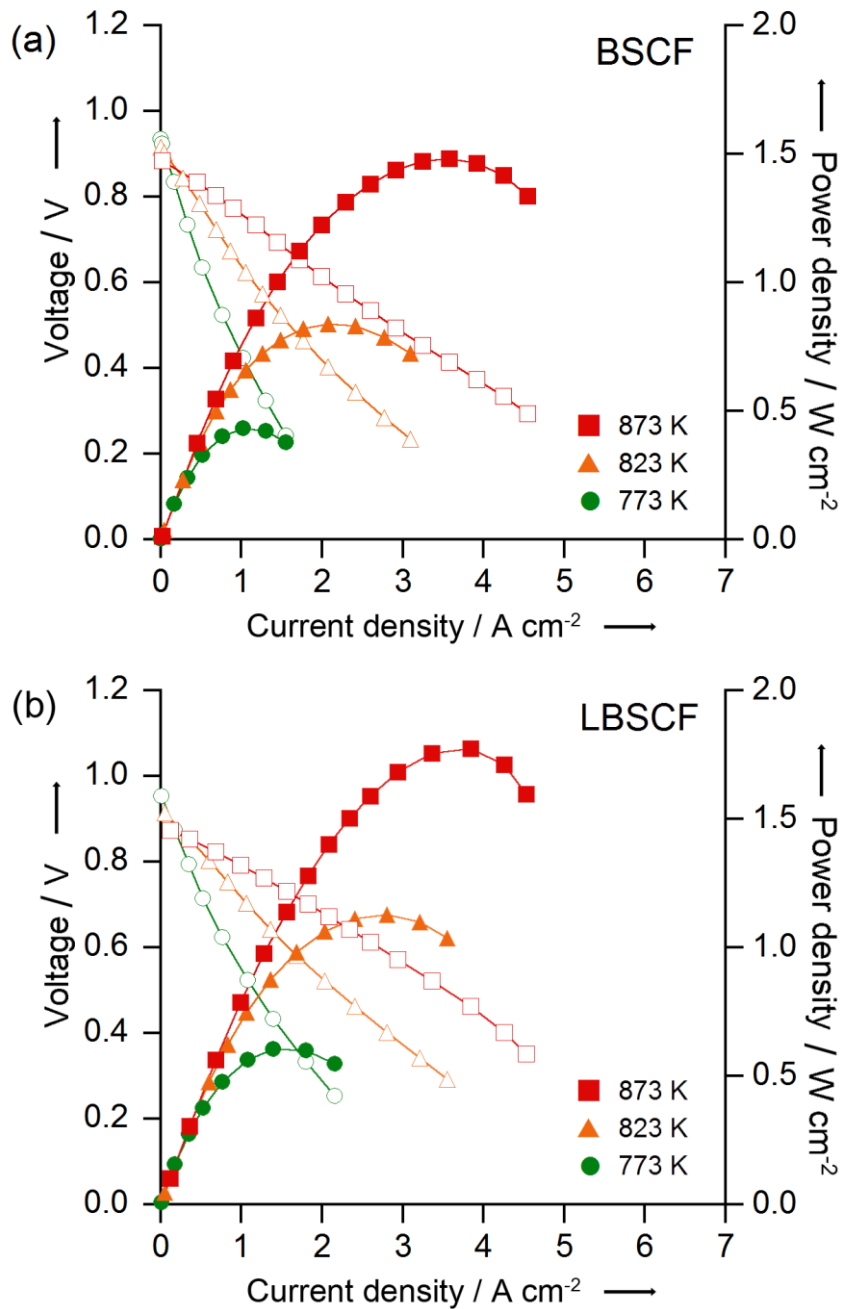


Figure 22 I - V curve and corresponding power density curves of single cell for a) BSCF-40GDC and b) LBSCF-40GDC cathodes in various temperatures.

Many researchers have reported that BSCF suffers from the degradation in long term stability due to the decomposition of the cubic perovskite into hexagonal perovskite at intermediate-temperature in air.⁴⁰ In addition, the phase instability of BSCF under CO₂-containing atmosphere also restricts its practical application for the SOFC cathode.^{50,51} Generally, such a structural instability of perovskites can be avoided by regulating the Goldschmidt tolerance factor (t_f) using appropriate substitutions, which can be defined as the following mathematical expression,

$$t_f = \frac{r_A + r_O}{\sqrt{2} \cdot (r_B + r_O)} \quad (1)$$

where r_A , r_B , and r_O are the radii of cation A, cation B, and oxygen, respectively. In order to stabilize the cubic structure, the t_f of perovskites should be closer to 1. For perovskite materials, the valence of B-site transition metals (Co/Fe) is changeable and trivalence metals coexist with quadrivalence metals^[35]; thus the tolerance factor should be calculated carefully with consideration of the various ionic radii of transition metals. In this paper, we have considered the distribution ratio of trivalence and quadrivalence for Co/Fe in order to decide the value of r_B . Assuming that r_B varies depending on the valence state of the B-site ions (i.e., a trivalence state or quadrivalence state), the t_f value can be calculated from the following equation:

$$t_f = \frac{(0.5 \cdot r_{La^{3+}}) + (0.25 \cdot r_{Ba^{2+}}) + (0.25 \cdot r_{Sr^{2+}}) + r_{O^{2-}}}{\sqrt{2} \cdot [x \cdot (0.8 \cdot r_{Co^{4+}} + 0.2 \cdot r_{Fe^{4+}}) + (1-x) \cdot (0.8 \cdot r_{Co^{3+}} + 0.2 \cdot r_{Fe^{3+}}) + r_{O^{2-}}]} \quad (2)$$

where x is the mole fraction of the quadrivalence B-site ions from the sum of the trivalence and quadrivalence B-site ions, and the ionic radii involved in this equation are taken from Shannon's results.^[36] As seen in Figure 23, the t_f of BSCF is within a range of 1.043 ~ 1.062, indicating that the structure of BSCF tends to change to the hexagonal phase, which is an impediment to long-term operation. Meanwhile, with substitution of smaller La^{3+} into the A-site of BSCF, the t_f values of LBSCF fall within a lower range of 1.014 ~ 1.033 compared to BSCF, suggesting that the structure of LBSCF has a smaller deformation of cubic symmetry than that of BSCF.

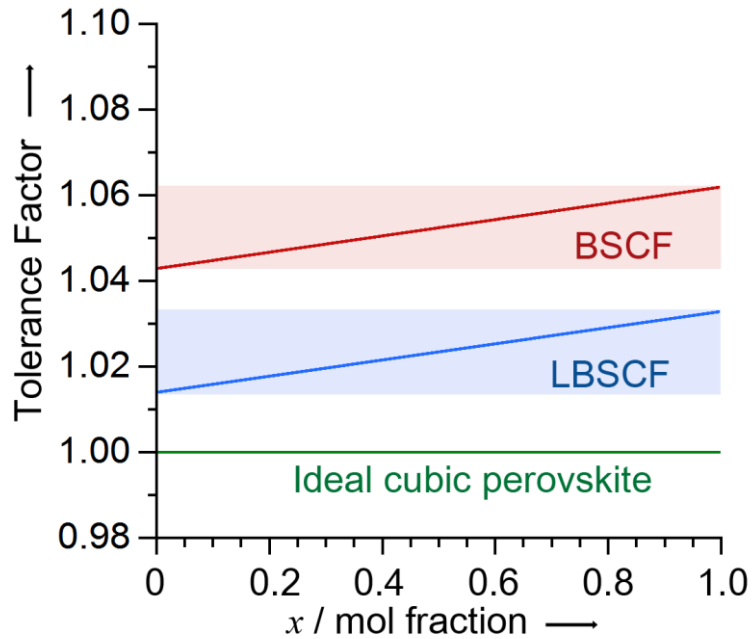


Figure 23 Tolerance factors (t_f) of the BSCF and LBSCF materials as function of mole fraction for quadrivalence B-site ion from the sum of trivalence and quadrivalence B-site ion. The existing region of t_f values for each samples is in colored.

In order to evaluate the structural stability of the BSCF and LBSCF samples under practical operating conditions, both sintered samples were re-annealed under ambient air and 10 vol% CO₂. All samples were then identified by XRD, as shown in Figure 24. For BSCF, the formation of a hexagonal phase is observed in air (Figure 9a), and barium carbonate is formed with exposure to 10 vol% CO₂ for 8 h (Figure 24c), as expected from previous reports.⁵² Meanwhile, no secondary phase was identified from the re-annealed LBSCF under both air and 10 vol% CO₂ (Figure 24b and d), suggesting that the cubic perovskite LBSCF has excellent chemical durability under air below 1123 K and/or a CO₂-containing atmosphere.

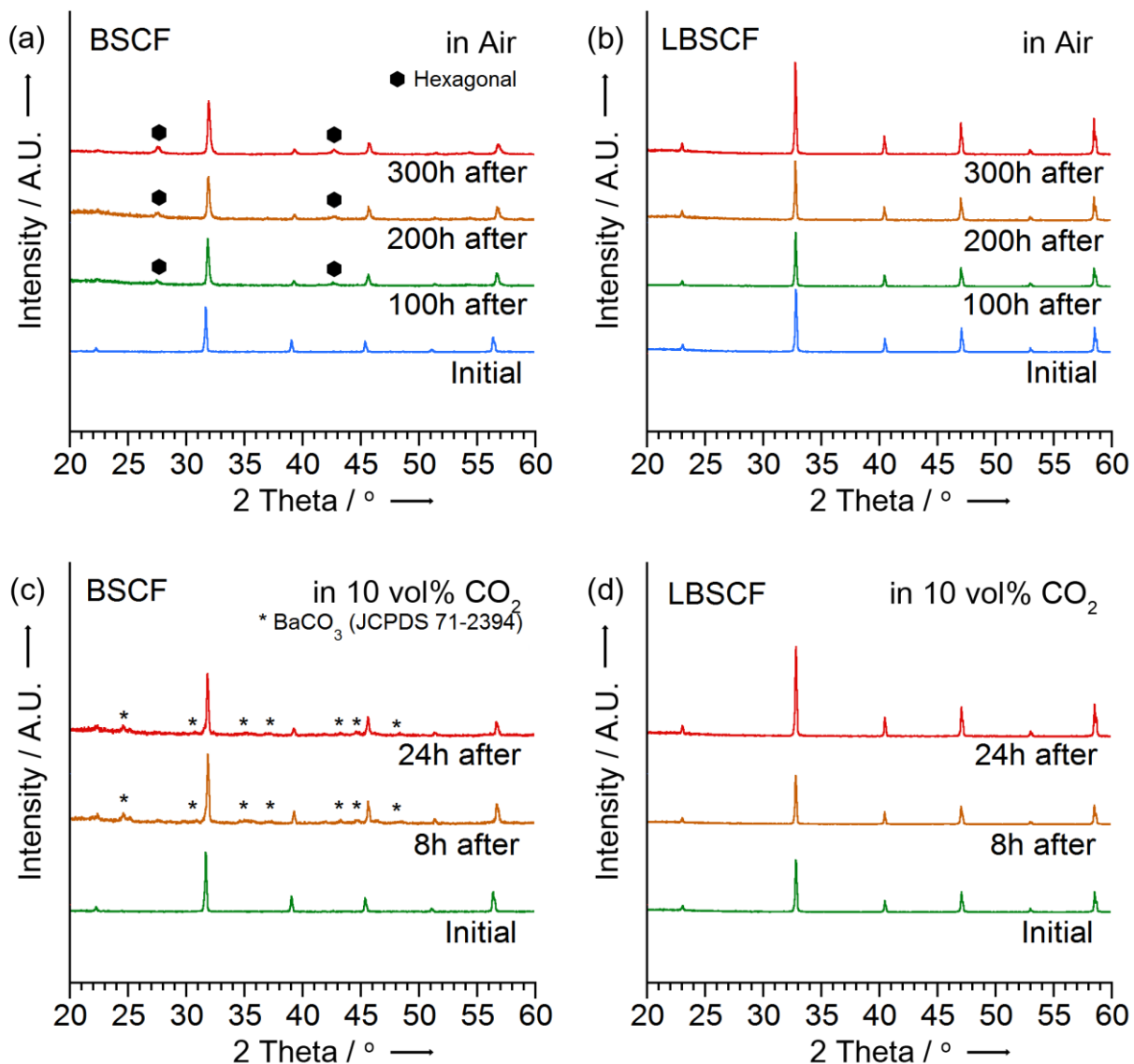
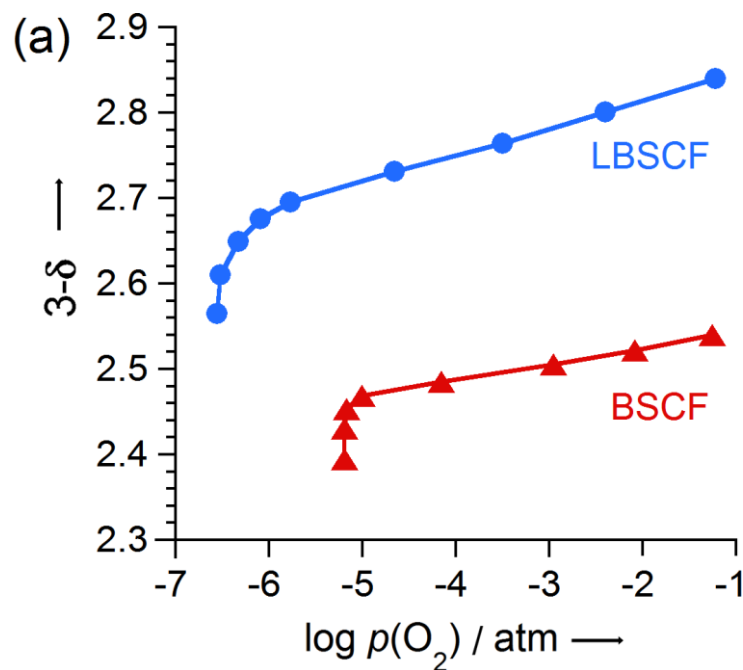


Figure 24 X-ray diffraction patterns for the BSCF and LBSCF re-annealed at 973 K in ambient air; a) and b). CO₂ durability result of both cathode powders re-annealed at 1173 K in 10 vol% CO₂; c) and d). Peaks of the hexagonal phase and carbonates are marked with a hexagon and asterisk, respectively.

In addition, under the operating conditions, the TPBs of the cathode are subjected to a lower $p(\text{O}_2)$, which

could cause redox degradation of the cathode. Thus, sufficient electrical conductivity and redox stability at lower $p(\text{O}_2)$ are important to ensure efficient current collection and long-term stability. Figure 25 presents the oxygen nonstoichiometries and electrical conductivities for LBSCF as a function of $p(\text{O}_2)$, determined by coulometric titration (CT). The detailed procedure of CT has been described elsewhere.⁴³ The initial oxygen contents of both samples are determined by iodometric titration and TGA data. As can be seen in Figure 25, the BSCF sample shows a sudden drop of oxygen content (Figure 25a) and electrical conductivity (Figure 25b) at around $\sim 10^{-5}$ atm $p(\text{O}_2)$, which is possibly the starting point of decomposition. Meanwhile, the oxygen content of the LBSCF starts to decline at a lower $p(\text{O}_2)$ of $\sim 10^{-6}$ atm with sufficient electrical conductivity of about 130 S cm^{-1} , suggesting that the LBSCF cathode has more favorable redox stability and reasonable current collection at the operating conditions than the BSCF cathode.



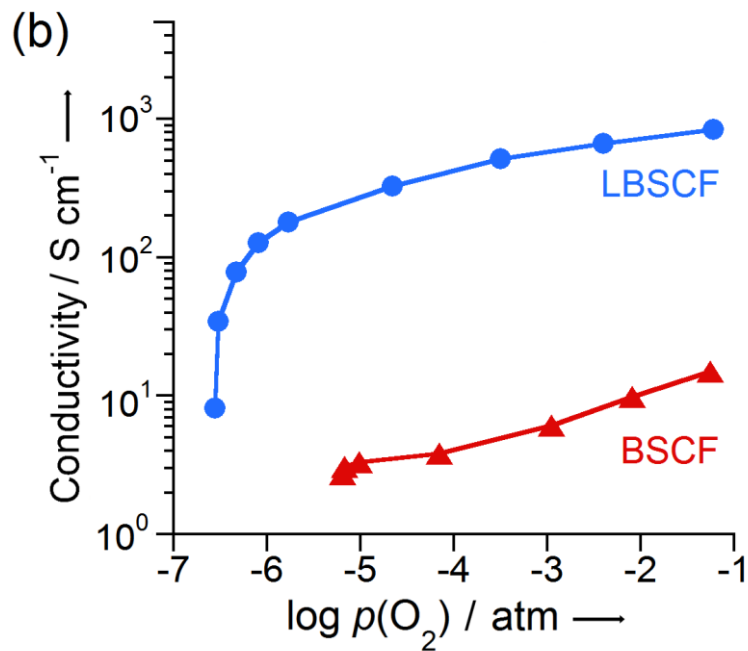


Figure 25 a) Oxygen non-stoichiometry and b) electrical conductivities of the BSCF [38] and LBSCF under various $p(\text{O}_2)$ (atm) at 973 K by coulometric titration.

Figure 26 presents the results of the long-term stability test for the BSCF and LBSCF with application of constant voltage of 0.6 V at 823 K with humidified hydrogen (~3% H_2O) as a fuel and air as an oxidant. As expected from the enhanced structural stability of LBSCF under various operating conditions, excellent stability of LBSCF is achieved with a power density of 0.81 W cm^{-2} for 100h, whereas electrochemical degradation of 25 % after 100h is observed for BSCF, and this is ascribed to its structural instability. Considering the enhancement of the electrochemical performance and structural stability, LBSCF is a promising candidate for cathode materials in practical IT-SOFC systems.

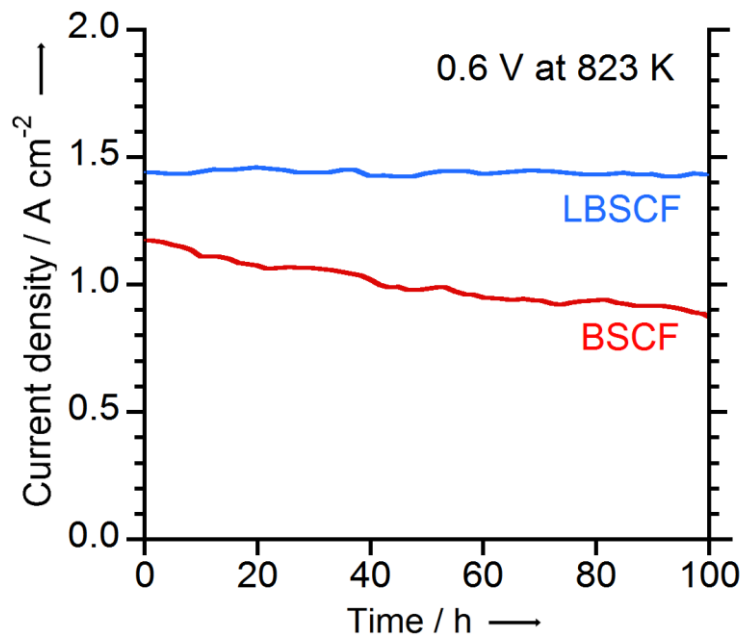


Figure 26 Long term stability data for the BSCF-40GDC and LBSCF-40GDC with applying a constant voltage of 0.6 V at 823 K.

3.4. Conclusions

In the present study, we have reported remarkable enhancement of the phase stability and electrochemical performance of La³⁺ doped BSCF by a strategic approach. At a given temperature, the electrical conductivity of LBSCF is much higher (900 S cm⁻¹ at 873 K) than that of BSCF (15 S cm⁻¹ at 873 K). LBSCF shows relatively lower ASR values of 0.064 Ω cm² compared to BSCF at 873 K, and exhibits remarkable cell performance of 1.77 W cm⁻² at 873 K. Tolerance factors of LBSCF closer to 1 than BSCF suggest that LBSCF has a more stable cubic perovskite structure. LBSCF shows not only high redox stability at lower $p(\text{O}_2)$ but also excellent phase stability under air and CO₂-containing atmospheres, which could reasonably account for its enhanced stability. Excellent stability of LBSCF is achieved with a power density of 0.81 W cm⁻² for 100 h, whereas 25 % degradation after 100 h is observed for BSCF. It is demonstrated that the electrochemical performance and chemical stability of BSCF are improved remarkably by La³⁺ doping and LBSCF is indeed a promising candidate for cathode materials in practical IT-SOFC systems.

Chapter 4. Triple-Conducting Layered Perovskites as Cathode Materials for Proton-Conducting Solid Oxide Fuel Cells

We report on an excellent anode-supported H^+ -SOFC material system using a triple conducting ($H^+/O^{2-}/e^-$) oxide (TCO) as a cathode material for H^+ -SOFCs. Generally, mixed ionic (O^{2-}) and electronic conductors (MIECs) have been selected as the cathode material of H^+ -SOFCs. In an H^+ -SOFC system, however, MIEC cathodes, however, limit the electrochemically active sites to the interface between the proton conducting electrolyte and the cathode. New approaches to the tailoring of cathode materials for H^+ -SOFCs should therefore be considered. TCOs can effectively extend the electrochemically active sites from the interface between the cathode and the electrolyte to the entire surface of the cathode. The electrochemical performance of NBSCF/BZCYYb/BZCYYb-NiO shows excellent long term stability for 500 h at 1023 K with high power density of 1.61 W cm^{-2} .

This chapter has been published.

Reproduced with permission from Kim, J., *et al.*, Triple-Conducting Layered Perovskites as Cathode Materials for Proton-Conducting Solid Oxide Fuel Cells, *Chemsuschem*, 7, 2811 (2014). Copyright 2014. Chemsuschem, Wiley.

4.1. Introduction

Solid oxide fuel cells (SOFCs) have attracted much attention because of their high energy conversion efficiency, low pollutant emissions, efficient reclamation of waste heat, and excellent fuel flexibility. The high operating temperature ($>1073\text{K}$) of SOFCs, however, is an obstacle to their commercialization, due mainly to significant degradation, sealing problems, high thermal stress, and utilization of expensive materials. In recent years, extensive efforts have been devoted to lowering the working temperature of SOFCs down to an intermediate temperature (IT) range (773 to 1073 K) because of the economic competitiveness and flexible choice of cell material.^{15,53–56}

Proton-conducting oxides are ideally suited for the electrolytes of IT-SOFCs because of the low activation energy and high ionic conductivity at intermediate temperatures. In addition, proton-conducting SOFC (H^+ -SOFC) can avoid water formation, and thus dilution of the fuel, on the anode side during operation because water will form on the cathode side of the cell, which can lead to higher fuel utilization and greater Nernst potential of SOFCs.^{57–61} In the H^+ -SOFC system, mobile protons can be incorporated at the anode by forming a covalent bond between the lattice oxygen and proton which originates from the dissociated water. This mobile protons transfer through the dense electrolyte to the cathode. The overall half reactions at the anode and cathode could be expressed as Equation. (1) and

(2), respectively: ^{62,63}



Among these proton conducting oxides for the electrolyte, the doped barium cerate and barium zirconate based materials are considered as two of the most promising candidates for H⁺-SOFC applications because of their fast proton transports. Barium cerate based materials have high conductivity ⁶⁴ but with limited stability, especially in steam or CO₂ containing atmospheres ^{58,65}. On the other hand, barium zirconate-based materials exhibited excellent chemical stability in steam or CO₂ containing atmospheres,⁶⁶ but their conductivity is one order of magnitude lower than that of the barium cerate systems.^{64,66,67} A good combination between them, Ba(Zr_{0.1}Ce_{0.7}Y_{0.2})O_{3-δ} (BZCY) showed a great potential to possess the high conductivity while maintaining excellent chemical stability.⁶⁸ Recently, Liu group reported a barium zirconate-cerate co-doped with Yb and Y, BaZr_{0.1}Ce_{0.7}Y_{0.1-x}Yb_xO_{3-δ} (BZCYYb), that displays excellent tolerance to sulfur poisoning and coking. This material is a very unique mixed ion conductor; it contains and allows rapid transport of both protonic defects and oxide ion vacancies, resulting in a high ionic conductivity (~0.01 S cm⁻¹ at humidified O₂ atmosphere).⁶⁹ However, the study based on BZCYYb electrolyte in application of SOFC are still at early stages and the performance of the full cell is limited by electrode materials, especially the cathode.^{60,70}

Generally, mixed ionic (O²⁻) and electronic conductors (MIECs) are chosen as cathode material of O²⁻ conducting SOFC system due to their excellent catalytic activities for the oxygen reduction reaction (ORR) by extending the electrochemically active site to the entire surface of cathode.^{71,72} On the contrary, for the reaction of proton and oxygen ion in the H⁺-SOFC system, oxygen ion should diffuse from the surface of MIECs to the interface between the proton conducting electrolyte and MIEC cathodes (Step 3 in Table 1). Consequently, the MIEC cathodes limit the electrochemically active site to the interface between proton conducting electrolyte and cathode as described in Figure 27a and Step 4-6 of Table 1.^{62,73} Therefore, new approaches should be considered in tailoring of cathode materials for H⁺-SOFCs. One of the basic requirements for high-performing H⁺-SOFC cathode material is the high conductivity of the electron, oxide ion, and proton with the high chemical stability. In this regards, the triple conducting (H⁺/O²⁻/e⁻) oxides (TCOs) effectively extend the electrochemically active site to the entire surface of cathode as proposed by elementary steps (Table 1) and Figure 27b.

Table 1 Suggested elementary reaction steps and their reaction orders for MIEC and TCO cathode with proton-conducting electrolytes

Step	Elementary reaction for MIEC cathode	Step	Elementary reaction for TCO cathode
Step 1	$O_{2(g)} \rightarrow 2O_{ad}$	Step' 1	$O_{2(g)} \rightarrow 2O_{ad}$
Step 2	$O_{ad} + 2e^-_{cathode} \rightarrow O^{2-}_{cathode}$	Step' 2	$O_{ad} + 2e^-_{cathode} \rightarrow O^{2-}_{cathode}$
Step 3	$O^{2-}_{cathode} \rightarrow O^{2-}_{interface}$	Step' 3	$OH^-_{electrolyte} \rightarrow OH^-_{cathode}$
Step 4	$OH^-_{electrolyte} \rightarrow H^+_{interface} + O^{2-}_{electrolyte}$	Step' 4	$OH^-_{cathode} \rightarrow H^+_{cathode} + O^{2-}_{electrolyte}$
Step 5	$H^+_{interface} + O^{2-}_{interface} \rightarrow OH^-_{interface}$	Step' 5	$2H^+_{cathode} + O^{2-}_{cathode} \rightarrow H_2O_{cathode}$
Step 6	$H^+_{interface} + OH^-_{interface} \rightarrow H_2O_{interface}$	Step' 6	$H_2O_{cathode} \rightarrow H_2O_{(g)}$
Step 7	$H_2O_{interface} \rightarrow H_2O_{(g)}$		

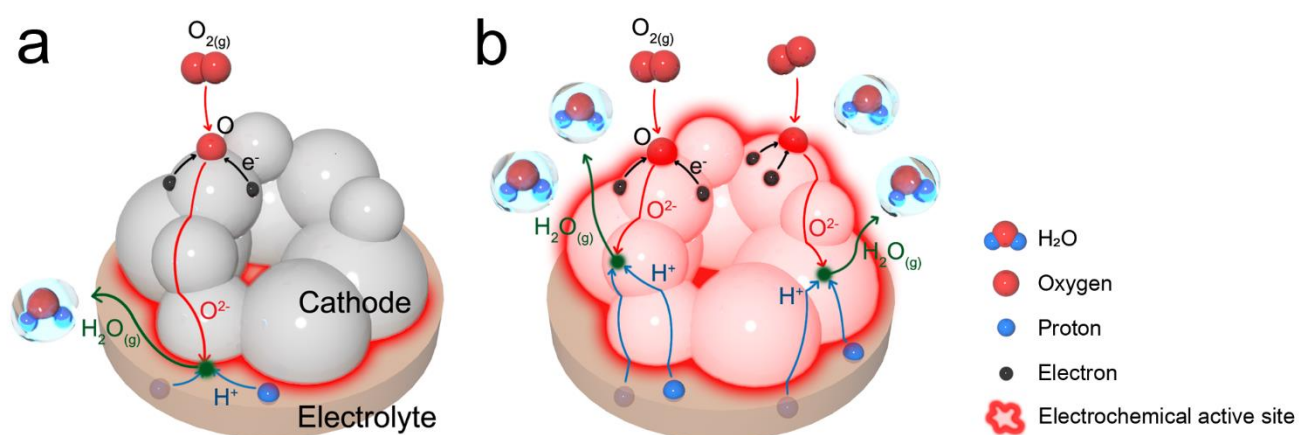


Figure 27 Schematic illustration of the water formation reaction at the H^+ -SOFC cathode using (a) a mixed ionic and electronic conductors (O^{2-}/e^-) and (b) a triple conducting oxides ($H^+/O^{2-}/e^-$)

Layered perovskite oxides have recently received a great deal of attention for O^{2-} -SOFC cathode materials due to their unusually rapid oxygen transport kinetics rate.^{74–79} More recently, we have reported the layered perovskite cathode material, $NdBa_{0.5}Sr_{0.5}Co_{1.5}Fe_{0.5}O_{5+\delta}$ (NBSCF), which has a high electrochemical performance with excellent stabilities under operating conditions.⁷⁶ This family of layered perovskite compounds has a general formula $AA'B_2O_{5+\delta}$ where A = trivalent lanthanide ion ($Ln = Pr, Nd, Sm, \text{ and } Gd$), $A' = Ba \text{ or } Sr$, and $B = \text{ a first row transition metal ion or a mixture thereof}$. The layered perovskite consists of two layers with alternating stacking of $\dots|AO|BO_2|A'O_\delta|BO_2|\dots$. Based on our DFT modeling results in the previous study, the layered structure provides a pore channel for ion motion in the $[Ln-O]$ and $[Co-O]$ planes that could provide fast paths for oxygen transport and this oxygen ion diffusion path could follow a zig-zag type trajectory through the $Co-O$ plane perpendicular to the $Ln-O$ plane.(Figure 28)⁷⁶ Furthermore, according to Grimaud et al., these layered perovskite cathode materials are found to exhibit the high proton conducting properties than other perovskite-related cathodes so that the layered perovskites can be considered as a promising candidate for H^+ -SOFC cathodes.⁸⁰ Therefore, layered perovskites is considered as promising TCO cathode

materials, which would show great potential in application of H⁺-SOFC systems.

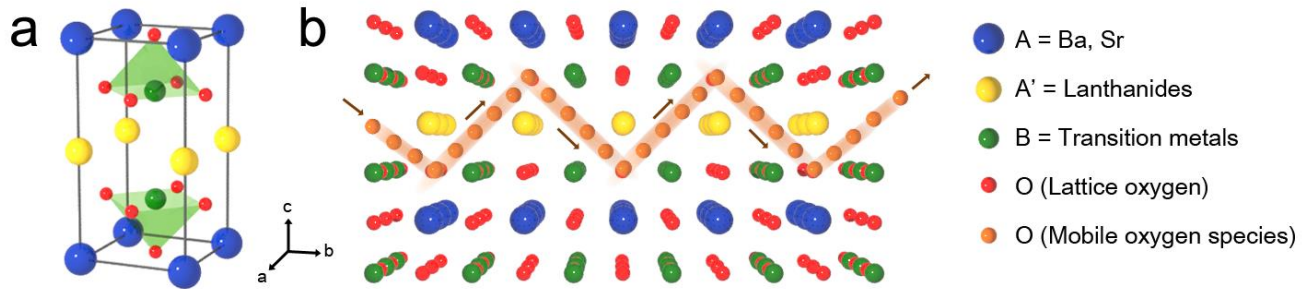


Figure 28 (a) The structure of layered perovskite unit cell($AA'B_2O_{5+\delta}$) and (b) a proposed mechanism for the bulk diffusion of the mobile oxygen species via the pore channels based on our previous study⁷⁶; a zig-zag type trajectory through the CoO plane perpendicular to the PrO plane.

In this study, we reported the application of a novel single-phase cathode material, NBSCF in H⁺-SOFC system and the highest performance of the fuel cell is reported so far based on proton-conducting electrolyte. The new anode-supported SOFC system is composed with NBSCF/BZCYYb/BZCYYb-NiO. The structural and morphological investigation are performed by means of X-ray diffraction (XRD) and scanning electron microscopy (SEM). The excellent long-term stability of single cells is demonstrated.

4.2. Experimental Section

Preparation of powders

The $\text{NdBa}_{0.5}\text{Sr}_{0.5}\text{Co}_{1.5}\text{Fe}_{0.5}\text{O}_{5+\delta}$ (NBSCF) for cathode and the NiO for the anode were synthesized using a Pechini method. Stoichiometric amounts of $\text{Nd}(\text{NO}_3)_3 \cdot 6\text{H}_2\text{O}$ (Aldrich, 99.9 %, metal basis), $\text{Ba}(\text{NO}_3)_2$ (Aldrich, 99+ %), $\text{Sr}(\text{NO}_3)_2$ (Aldrich, 99+ %), $\text{Co}(\text{NO}_3)_2 \cdot 6\text{H}_2\text{O}$ (Aldrich, 98+ %), and $\text{Fe}(\text{NO}_3)_3 \cdot 6\text{H}_2\text{O}$ (Aldrich, 98%) were dissolved in distilled water with proper amounts of citric acid and ethylene glycol. The solutions were heated in air followed by combustion to form fine powders, which were calcinated at 873 K for 4 h. The NiO powders for anode were synthesized by glycine nitrate process (GNP). Stoichiometric amounts of nitrates were dissolved in distilled water with proper amount of glycine. The solutions were heated up to 623 K and followed by combustion to form fine powders. $\text{BaZr}_{0.1}\text{Ce}_{0.7}\text{Y}_{0.1}\text{Yb}_{0.1}\text{O}_{3-\delta}$ (BZCYYb) powders were synthesized by a typical solid state reaction method. Stoichiometric amounts of barium carbonate, zirconium oxide, cerium oxide, ytterbium oxide, and yttrium oxide powders (all from Aldrich Chemicals) were mixed by ball milling, followed by sintering at 1373 K in air for 10 h.

Ni-BZCYYb anode-supported cells were fabricated using a drop-coating method. NiO and BZCYYb powder (weight ratio of 6.5:3.5) were mixed by ball milling in ethanol for 24 h. After drying, the NiO-BZCYYb mixture was pressed into a pellet (0.6 mm thick and 15 mm diameter). Thin BZCYYb electrolyte membranes were prepared by a refined particle suspension coating technique. A BZCYYb suspension was prepared by dispersing BZCYYb powders (Aldrich) in ethanol with a small amount of binder (polyvinyl Butyral, B-98) and dispersant (Triethanolamine, Alfa Aesar) at a ratio of 1:10. The BZCYYb suspension was applied to a NiO-BZCYYb anode support by drop-coating, followed by drying in air and subsequent co-sintering at 1673 K for 4 h. For preparation of cathode slurries, pre-sintered NBSCF cathode powders were mixed by ball milling, blended together with an organic binder (Heraeus V006). The NBSCF cathode slurry was screen printed onto electrolyte surface of Ni-BZCYYb anode-supported cells. The single cells consisting three layers (NBSCF/BZCYYb/NiO-BZCYYb) were subsequently sintered at 1173 K in air for 4h.

Synthesized materials were confirmed with X-ray diffraction (XRD) patterns (Rigaku-diffractometer, Cu $K\alpha$ radiation). The microstructures and morphologies of the single cells were observed using a field emission scanning electron microscope (SEM) (Nova SEM).

For the single cell tests, Ag wires were attached at the cathode side using Ag paste and Pt wires were attached at the anode side using Ni-O paste as a current collector. The NiO-BZCYYb anode-supported single cell was sealed fully onto one end of the alumina tube using a ceramic adhesive (Aremco, Ceramabond 552). Humidified H_2 (3% H_2O) was applied to the anode side as a fuel through a water bubbler with a flow rate of 100 mL min^{-1} , while air was supplied as an oxidant to the cathode during the single cell test. The I-V polarization curves were recorded between 873 and 1023 K. The I-

V curves and impedance spectra were acquired with a BioLogic Potentiostat and analysed with EC-lab software.

4.3. Results and Discussion

The XRD patterns of the NBSCF, BZCYYb and their composite powders are presented in Figure 29. The characteristic diffraction patterns for the NBSCF and BZCYYb are identified in a single phase, respectively. The chemical compatibility between the NBSCF and BZCYYb is investigated by heating the mixtures at 1223 K for 4h. As shown in Figure 29 (c), there are no obvious reactions between the NBSCF and BZCYYb powders, indicating that the layered perovskite NBSCF is chemically compatible with BZCYYb under the processing condition.

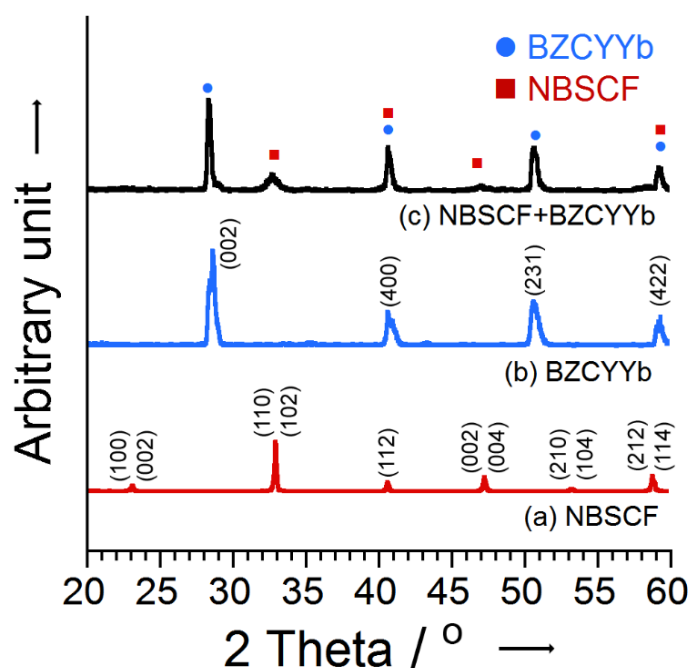


Figure 29 XRD patterns of (a) NBSCF powder sintered at 1323 K for 12 h, (b) BZCYYb powder sintered at 1673 K for 4 h, and (c) NBSCF–BZCYYb mixture after sintered at 1223K for 24 h.

Figure 30 shows the microstructure of the NBSCF cathode and single cell (NBSCF/BZCYYb/NiO-BZCYYb) by SEM image. The NBSCF cathode has a highly porous morphology that ensures good gas diffusion. As shown in Figure 30b, the dense BZCYYb electrolyte and the porous NBSCF cathode (ca. $\sim 15\mu\text{m}$ thick) is successfully fabricated. The NBSCF cathodes are adhered well onto the BZCYYb electrolyte without any cracks or delamination, which is expected to enhance the mechanical compatibility and the long-term stability of the cathode/electrolyte interface.

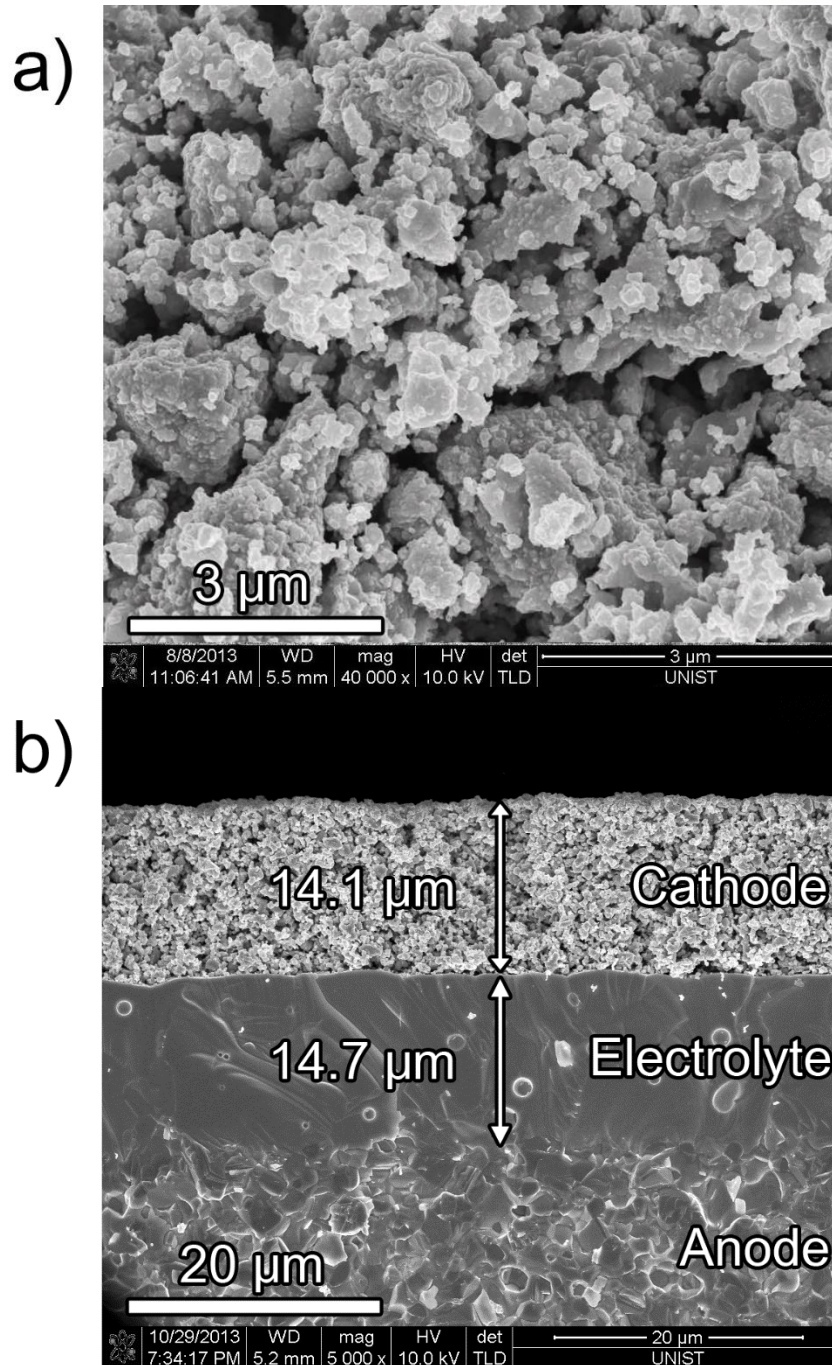


Figure 30 Scanning electron microscope image of (a) porous NBSCF cathode and (b) cross-section of the single cell.

The long term stability test is performed with applying the constant voltage of 0.6 V at 1023 K and presented in Figure 31. Humidified hydrogen (~3% H₂O) and air is used as fuel and oxidant, respectively. The power density improves during the initial period within about 100 h. This kind of activation phenomena is often observed in the Mn-based perovskite cathode such as lanthanum manganite⁸¹ and a series of praseodymium manganites.⁸² At the present study, it may be associated with

the improvement of the electrode catalyst function and the enhancement of the activations between the electrodes/electrolyte which needs our further investigation.⁸³ After the stabilization of the power output, the excellent power density of 1.61 W cm^{-2} is produced at 1023 K without the observable degradation for 500 h. To the best of our knowledge, the outstanding power density 1.61 W cm^{-2} with long term stability for 500 h represents the highest operating performance ever reported in the literature based on barium cerate electrolyte under the similar testing conditions. Furthermore, in practical SOFC applications, such stable and high power density can contribute to improve not only the fuel efficiency but also the commercialization of the SOFCs.

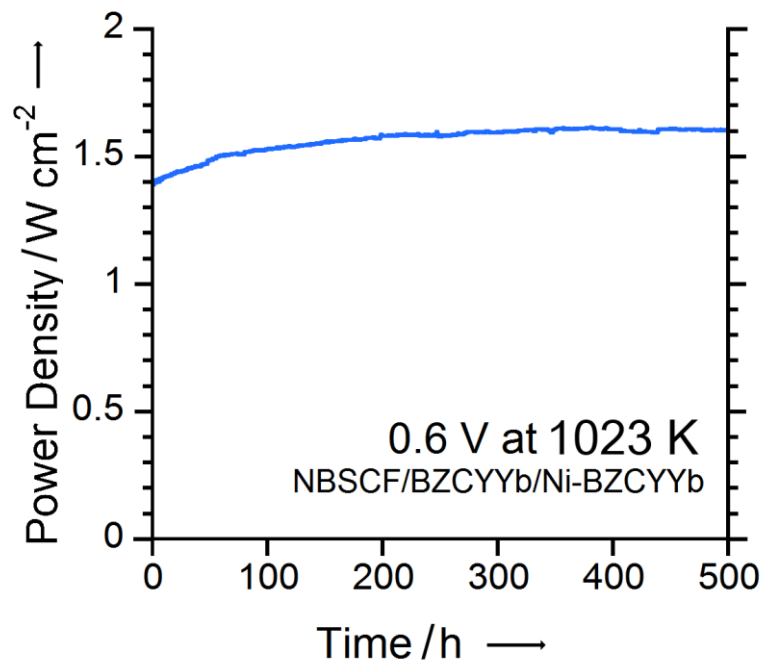


Figure 31 Long term stability data of the single cells (NBSCF/BZCYYb/NiO-BZCYYb) with applying a constant voltage of 0.6 V at 1023 K.

After stability test for 500 h, the impedance spectra and current-voltage (I - V) curves of the single cell are obtained at various temperatures. Generally, impedance spectra of the single cell is used to describe all resistances associated with the electrode and electrolyte. The intercept with the real axis at high frequencies represents the ohmic resistance which is mainly originated from the electrolyte, whereas the difference between the high-frequency and low-frequency intercepts with the real axis designates the sum of the electrode polarization resistances for the single cell. As shown in Figure 32a, the ohmic resistance of the single cell are 0.063, 0.079, 0.100, 0.128 $\Omega \text{ cm}^2$ and the polarization resistances are 0.046, 0.081, 0.145, and 0.284 $\Omega \text{ cm}^2$ at 1023, 973, 923, and 873 K, respectively.

As expected from the low ohmic and polarization resistances of the single cells, the outstanding

maximum power densities of 1.71, 1.37, 1.05, and 0.69 W cm⁻² is achieved at 1023, 973, 923, and 873 K, respectively, and presented in Figure 32b. Again, the new anode-supported H⁺-SOFC material system (NBSCF/BZCYYb/BZCYYb-NiO) shows the highest maximum power densities ever compared to any H⁺-SOFC configurations at the similar operating conditions.^{69,84-87} This outstanding results demonstrate that H⁺-SOFC with a configuration of NBSCF/BZCYYb/BZCYYb-NiO is one of the most compatible material system in terms of practical IT-SOFC applications.

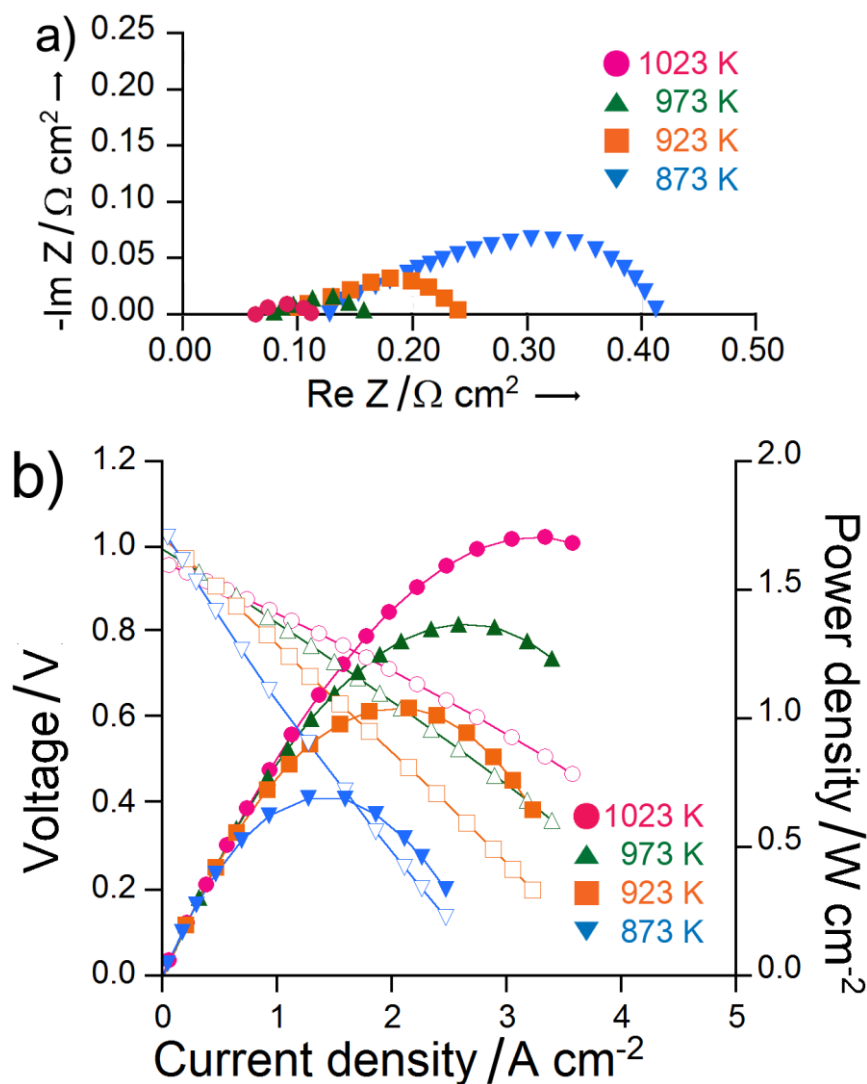


Figure 32 (a) Impedance spectra of the single cell (NBSCF/BZCYYb/NiO-BZCYYb) measured under open-circuit condition and (b) I - V curve and corresponding power density curves of the single cell at various temperatures after 500h stability test.

4.4. Conclusion

In summary, we evaluated the electrochemical performance of the new anode-supported SOFC material system, NBSCF/BZCYYb/BZCYYb-NiO. The NBSCF and BZCYYb powders were successfully synthesized and result of the single cell test shows the excellent long term stability for 500 h at 1023 K with high power density of 1.61 W cm⁻². TCO cathodes effectively extend the electrochemically active site from interface between electrode and electrolyte to the entire surface of cathode. This work demonstrates that the triple conducting (H⁺/O²⁻/e⁻) oxide cathode, NBSCF, shows excellent compatibility with proton-conducting electrolyte, BZCYYb. The new anode-supported SOFC material system, NBSCF/BZCYYb/BZCYYb-NiO, is promising candidate for the practical IT-SOFC applications.

Chapter 5. Hybrid-solid oxide electrolysis cell: A new strategy for efficient hydrogen production

Water electrolysis based on a solid oxide electrolysis cell (SOEC) has potential to be cost-effective, environmentally friendly, and highly efficient for hydrogen production. There are two types of SOECs, depending on electrolyte materials: oxygen ion conducting SOECs (oxygen-SOECs) and proton conducting SOECs (proton-SOECs). Here we report our new findings in exploring a SOEC based on a mixed-ion conductor that can transport both oxygen ion and proton at the same time, which is denoted as “Hybrid-SOEC”. When $\text{BaZr}_{0.1}\text{Ce}_{0.7}\text{Y}_{0.1}\text{Yb}_{0.1}\text{O}_3$ was used as an electrolyte, the Hybrid SOEC shows the highest efficiency, demonstrating a current density of 3.16 A cm^{-2} at 1.3 V and $750 \text{ }^\circ\text{C}$ in 10% humidified hydrogen at hydrogen electrode and 10% humidified air at air electrode. Moreover, the Hybrid SOEC exhibits no observable degradation in performance for more than 60 hours of continuous operation, implying a robust system for hydrogen production.

This chapter has been published.

Reproduced with permission from Kim, J., *et al.*, Hybrid-solid oxide electrolysis cell: A new strategy for efficient hydrogen production, *Nano energy*, 44, 121 (2017). Copyright 2017. Nano energy, Elsevier.

5.1. Introduction

Environment-friendly and clean fuels have attracted world-wide attention due to the growing concerns about global warming and other environmental issues associated with the heavy consumption of fossil fuels.⁸⁸ Hydrogen is considered a promising alternative to fossil fuels because it is the cleanest fuel on the earth and has the highest gravimetric energy density among all chemical fuels (143 kJ kg^{-1}).^{89,90} However, hydrogen does not exist naturally on the earth and must be produced from water or hydrocarbons. In fact, most hydrogen used today ($> 90\%$) is produced from hydrocarbons by the steam reforming, resulting in greenhouse gas (CO_2) emission and high cost.⁹¹ Other environmentally benign hydrogen production processes include photoelectrochemical, thermochemical, and electrochemical water splitting. Among them, water electrolysis is the most viable approach when renewable energy sources can be used to run the process. Low temperature electrolysis such as polymer electrolyte membrane (PEM) electrolysis and alkaline water electrolysis ($<100 \text{ }^\circ\text{C}$), however, needs significant amount of the electricity and noble metal-based electrocatalysts, leading to high cost and low energy efficiency.⁹² In contrast, high-temperature steam electrolysis based on solid oxide electrolytic cells (SOECs) is much more efficient because of their advantages for the water splitting both thermodynamically and kinetically.⁹³

Oxygen-SOEC is one of the most promising candidate for the high temperature water electrolysis.⁹⁴

In this system, the hydrogen is produced from the water-electrolysis reaction at the hydrogen electrode side as described in Figure 33(a). As an electrolyte material, yttria-stabilized zirconia (YSZ) is conventionally used because the YSZ exhibits sufficient pure oxygen ion conductivity at high temperatures ($> 800\text{ }^{\circ}\text{C}$).^{95–98} Despite the benefits of high temperature operation, however, wide application of the oxygen-SOEC has been inhibited because of critical issues (*e.g.*, poor long-term cell stability, interlayer diffusion, fabrication and materials problems).

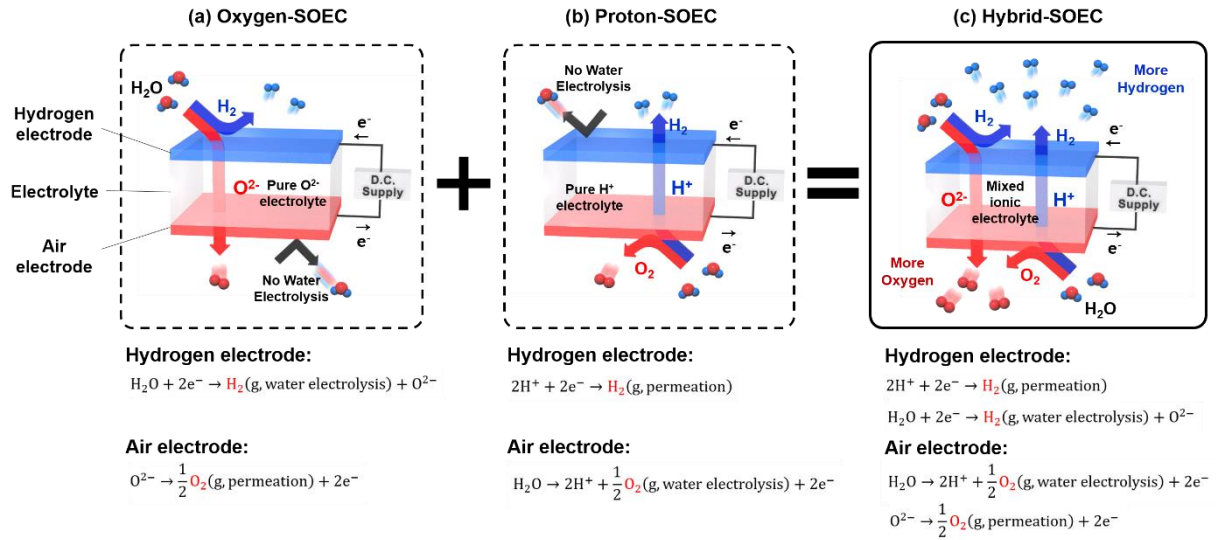


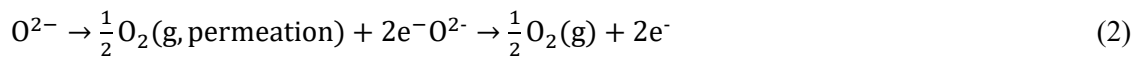
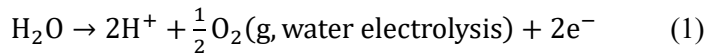
Figure 33 Schematic diagrams of the working principle. (a) Oxygen-SOEC, (b) proton-SOEC, and (c) Hybrid-SOEC system. In the oxygen- and proton-SOEC systems (a and b), even in the presence of steam on both electrodes, the electrochemical reaction for the water-electrolysis can occur at only one electrode. On the contrary, when mixed ion conducting electrolyte is used, the water electrolysis can occur at both at both air and hydrogen electrodes (so-called Hybrid-SOEC operating system), because the electrolyzed ion species (O^{2-} and H^+) can be counter-diffused across the mixed ionic conducting electrolyte. Consequently, in the Hybrid-SOEC system (c), more hydrogen could be generated by allowing simultaneous the oxygen-SOEC and proton-SOEC operation.

For these reasons, proton-SOECs using proton conducting oxides (PCOs) as electrolyte materials have acquired much interests because of their intermediate to low temperature operation.⁹⁹ In the proton-SOEC system (Fig. 1(b)), the proton is generated by water electrolysis at the air electrode and this proton permeates through the pure proton-conducting electrolyte, and the permeated proton reacts with electrons to produce hydrogen at the hydrogen electrode. Recently, extensive efforts have been devoted to developing the PCOs based on barium-zirconates (BZOs) and barium-cerates (BCOs) to improve their chemical stability and proton conductivity. Among those PCOs, aliovalent-doped $\text{BaCe}_{1-x}\text{Zr}_x\text{O}_{3-\delta}$ ($0 < x < 1$) have demonstrated high proton conductivity and successfully eliminated major issues

such as poor sinterability and low proton conductivity.^{59,100}

One of the notable points from these operating principles is that the water-electrolysis reaction can theoretically be occurred in both air electrode and hydrogen electrode depending on the type of ions (O^{2-} or H^+) that permeates the electrolyte. However, the water-electrolysis reaction is limited to only one side of electrode in the conventional SOECs, because only one ion can permeate across the single ion conducting electrolyte (*e.g.*, YSZ, BCOs, and BZO) even though steam is fed to both electrodes of the SOEC. In this regard, the introduction of the electrolyte conducting simultaneously both O^{2-} and H^+ species could be a good approach for the efficient hydrogen and oxygen production. In this system, water electrolysis can be occurred at both air and hydrogen electrodes (so-called Hybrid-SOEC operating system, Fig. 1(c)) because the electrolyzed ion species (O^{2-} and H^+) can be counter-diffused in the opposite direction across the mixed ionic conducting electrolyte. In other words, in the Hybrid-SOEC system, more hydrogen and oxygen could be generated simultaneously from the permeated proton (Equation 1 and 3) and water-electrolysis (Equation 2 and 4). The overall reactions at the air and hydrogen electrode in the Hybrid-SOEC system can be expressed as follows:

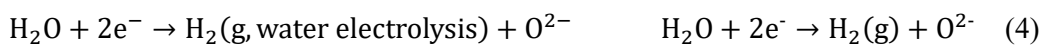
Air electrode:



Hydrogen electrode:



됩니다.



In this study, for the first time, we demonstrate the novel concept of “Hybrid-solid oxide electrolysis cell” (Hybrid-SOEC) based on the mixed ionic conducting electrolyte. To realize the efficient and stable Hybrid-SOEC operation, we adopt the $BaZr_{0.1}Ce_{0.7}Y_{0.1}Yb_{0.1}O_{3-\delta}$ (BZCYYb) as an electrolyte because this material has both protonic and oxide ion defect, resulting in high mixed ionic (O^{2-} and H^+) conductivity under proper condition.¹⁰¹ For electrode materials, we choose $NdBa_{0.5}Sr_{0.5}Co_{1.5}Fe_{0.5}O_{5+\delta}$ (NBSCF) - BZCYYb composite and Ni-BZCYYb composite as an air electrode and hydrogen electrode, respectively. The NBSCF layered perovskite can conduct protons, oxygen ions, and electrons, leading to increased number of electrochemically active sites on the entire surface of the air.^{6,76} These properties of the NBSCF may improve the catalytic activity for steam dissociation and O_2 evolution. Also, Ni shows excellent electrocatalytic activity for water splitting and hydrogen evolution and good compatibility with making Ni-BZCYYb composite as an ideal hydrogen electrode for the Hybrid

SOEC.¹⁰² The Hybrid-SOEC exhibits outstanding electrochemical performance with stability compared to other SOECs and representative water-electrolysis devices reported in the literatures.

5.2. Experimental Section

Synthesis of electrode and electrolyte powders: $\text{NdBa}_{0.5}\text{Sr}_{0.5}\text{Co}_{1.5}\text{Fe}_{0.5}\text{O}_{5+}$ (NBSCF) were synthesized by the Pechini method. The desired composition was obtained by each dissolving nitrate salts in distilled water with the addition of quantitative amounts of citric acid and ethylene glycol. After a viscous resin was formed, the mixture was heated to roughly 250 °C in air, followed by combustion to form powders, which were calcined at 600 °C for 4 hours and ball-milled in acetone for 24 hours. $\text{BaZr}_{0.1}\text{Ce}_{0.7}\text{Y}_{0.1}\text{Yb}_{0.1}\text{O}_3$ - (BZCYYb) powders were synthesized by the typical solid state reaction method. Stoichiometric amounts of barium carbonate, zirconium oxide, cerium oxide, ytterbium oxide, and yttrium oxide powders (all from Aldrich Chemicals) were mixed by ball milling, followed by sintering at 1100 °C in air for 10 hours. The NiO powders for the hydrogen electrode were synthesized by the glycine nitrate process (GNP). Stoichiometric amounts of nitrates were dissolved in distilled water with a proper amount of glycine. The solutions were heated up to 350 °C and followed by combustion to form fine powders.

Preparation of sample for XRD and SEM analysis: In order to test the chemical stability between the NBSCF and BZCYYb, slurries of the NBSCF-BZCYYb composite electrode were applied on the BZCYYb electrolyte by a screen printing method, and then fired at 950 °C in air for 4 hours. The chemical reactivity of NBSCF and BZCYYb was confirmed by using an X-ray diffractometer (Rigaku diffractometer, Cu K radiation). The microstructures and cross section of the Ni-BZCYYb/BZCYYb/NBSCF-BZCYYb single cell after electrolysis test were observed using field emission scanning electron microscopy (Nova Nano SEM, FEI, USA).

Fabrication of electrolysis cell: The NiO-BZCYYb electrode-supported cell was fabricated to measure the electrolysis performance and durability. For preparation of air electrode slurries, the calcined NBSCF powder and BZCYYb were mixed by ball-milling at weight ratio of 8:2, blended with a binder (Heraeus V006). NiO-BZCYYb supported cells were fabricated using the drop-coating method. The NiO-BZCYYb hydrogen electrode was prepared by a mixture of NiO and BZCYYb (weight ratio of 6.5:3.5) after being ball-milled in ethanol for 24 hours. The BZCYYb suspension was applied to a NiO-BZCYYb support by drop-coating, followed by drying in air and subsequent co-sintering at 1400 °C for 4 hours. Air electrode slurries were applied onto the surface of the BZCYYb electrolyte by screen printing and were finally sintered 950 °C for 4 hours in air.

Electrolysis performance and stability test: For the electrolysis tests, Ag wires were attached at both electrodes of the Ni-BZCYYb / BZCYYb / NBSCF-BZCYYb cell using Ag paste as a current collector. The cell was sealed fully onto one end of the alumina tube using a ceramic adhesive (Aremco, Ceramabond 552). The entire cell was placed inside a furnace and heated to the desired temperature. Nitrogen gas was switched to hydrogen, changing the phase from Ni oxide to Ni metal. The cell was tested from 750 to 550°C under three different atmosphere conditions; (1) in Hybrid-SOEC system:

under 90% H₂ and 10% steam fed in the hydrogen electrode and 90% air and 10% steam fed in the air electrode (2) in oxygen-SOEC system: under 90% H₂ and 10% steam fed in the hydrogen electrode and 100% air fed in the air electrode (3) in proton-SOEC system: under 100% hydrogen fed in the hydrogen electrode through bubbler at room temperature and 90% air and 10% steam fed in the air electrode. In order to assess the stability of the Ni-BZCYYb/BZCYYb/NBSCF-BZCYYb cell in Hybrid-SOEC, the voltage of the cell was recorded as a function of time under a constant high current of -0.45 A cm⁻² at 550 °C under 90% H₂ and 10% steam fed in the hydrogen electrode and 90% air and 10% steam fed in the air electrode. Impedance spectra, *I-V* curves and stability of the electrolysis cell were examined using a BioLogic Potentiostat at operating temperature. Impedance spectra were recorded under OCV in a frequency range of 1 mHz to 500 kHz with AC perturbation of 14 mV from 750 to 550 °C.

5.3. Results and discussion

In many cases, reactions between the electrode and the electrolyte materials may result in insulating phases at the interfaces, which blocks ionic and electronic transport across the interface between the electrode and the electrolyte.¹⁰³ Figure 34 shows XRD patterns of the NBSCF-BZCYYb composite fired at 950 °C for 4 hours. All the peaks correspond to the characteristic peaks for either the NBSCF or the BZCYYb, indicating that there are no obvious interfacial reactions or distinct secondary phases between them.

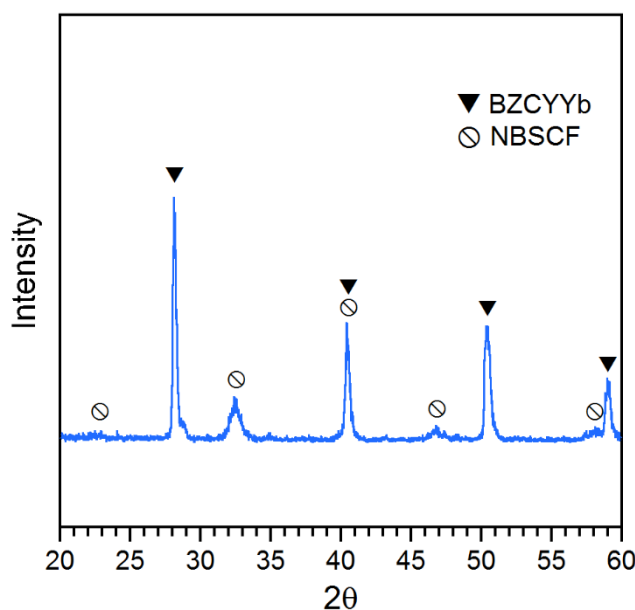


Figure 34 X-ray diffraction pattern of BZCYYb-NBSCF composite sintered at 950 °C 4hours.

The schematic diagram and experimental details for Hybrid-SOEC measurements are described in Figure 35. Hydrogen was supplied to the hydrogen electrode side while air was supplied to the air electrode side with a flow rate of 100 mL min⁻¹. In Hybrid-SOEC measurements, 10% steam was supplied to both electrodes from a water bubbler kept at a constant temperature for the required amount of steam and the tubes were heated by a heating tape to prevent condensation. Based on this Hybrid-SOEC equipment system, the impedance spectra and current-voltage (*I-V*) curves of the Ni-BZCYYb / BZCYYb / NBSCF-BZCYYb electrolytic cell were obtained at various temperatures. Generally, the ohmic resistance of the cell, determined from the intercept at high frequencies, corresponds to the ionic resistance of the BZCYYb electrolyte. The non-ohmic polarization resistance, determined by the diameter of the impedance loop (the difference between the intercept at the high frequencies and that at the low frequencies), includes the resistance to charge transfer and mass transfer processes for both electrodes.¹⁰⁴ Nyquist plot of the impedance data measured at OCV in Hybrid-SOEC system is shown

in Fig. S3. The non-ohmic resistances of the Hybrid-SOEC were 0.046, 0.065, 0.106, 0.209, and 0.383 $\Omega \text{ cm}^2$ at 750, 700, 650, 600, and 550 $^{\circ}\text{C}$, respectively.

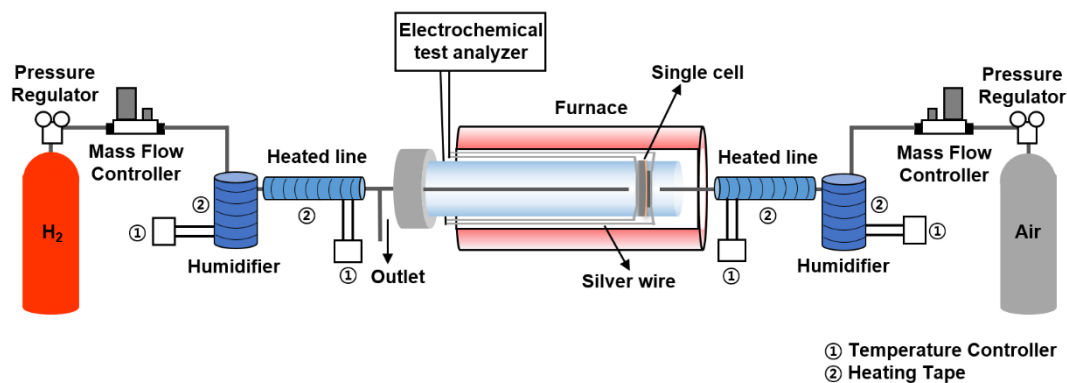


Figure 35 Schematic illustration of the experimental setup employed for the Hybrid-SOEC experiments.

Figure 36 (a) shows the performance of the Ni-BZCYYb / BZCYYb / NBSCF-BZCYYb electrolytic cell operated as Hybrid-SOEC at temperatures between 550 $^{\circ}\text{C}$ and 750 $^{\circ}\text{C}$. As expected from low non-ohmic resistance of the single cell, excellent current densities of 3.16, 2.41, 1.62, 0.75 and 0.42 A cm^{-2} were achieved at 750, 700, 650, 600 and 550 $^{\circ}\text{C}$, respectively, at 1.3 V (*i.e.*, the thermo-neutral voltage for steam electrolysis). For direct comparison, the results of our hybrid-SOEC at 700 $^{\circ}\text{C}$ are presented in Figure 36(b) with other results reported in the literatures.^{98,105–109} The performance of the Hybrid-SOEC is clearly better than those for the oxygen-SOECs and the proton-SOECs. As summarized in Figure 36(c), the remarkable current density of 2.41 A cm^{-2} is achieved at 700 $^{\circ}\text{C}$, which is much higher than those reported for the oxygen-SOEC (0.40 ~ 0.52 A cm^{-2}) and the proton-SOEC (0.08 ~ 0.21 A cm^{-2}). Conclusively, the Hybrid-SOEC based on BZCYYb represents one of the most promising electrolytic systems for the efficient hydrogen production.

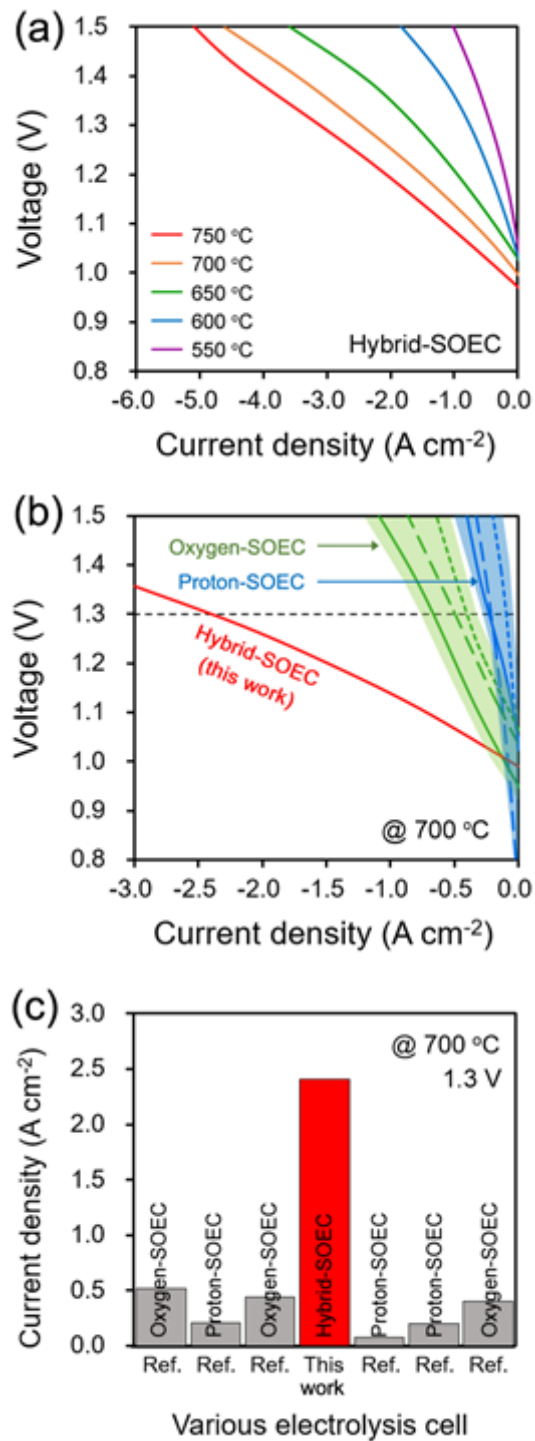


Figure 36 *I-V* curves for a Ni-BZCYYb / BZCYYb / NBSCF-BZCYYb cell. (a) *I-V* curves in the Hybrid-SOEC system at various temperatures (under 90% H₂ and 10% steam fed in the hydrogen electrode side and 90% air and 10% steam fed in the air electrode side). (b) *I-V* curves for comparison of present work and other studies reported in the literature at 700 °C (the performance range of *I-V* curves for the oxygen-SOEC and proton-SOEC is shaded in green and blue color, respectively). (c) Comparison of the current densities at 700 °C and 1.3 V.

In order to compare the electrochemical performance of the Hybrid-SOEC in different operating conditions, the single cell test was performed under the oxygen-SOEC, proton-SOEC, and Hybrid-SOEC systems (Figure 37). Under the Hybrid-SOEC system (10 % humidified condition on both electrodes), the excellent current density value of 4.61 A cm^{-2} was obtained at a cell voltage of 1.5 V at $700 \text{ }^\circ\text{C}$. In contrast, when the cell was operated in the proton-SOEC system (10 % humidified air on the air electrode), the current density was 3.17 A cm^{-2} at the same condition. Similarly, when it was operated in the oxygen-SOEC system (10 % humidified hydrogen on the hydrogen electrode), the current density was 4.02 A cm^{-2} . The current density at the Hybrid-SOEC system is approximately 45 % and 15 % higher than that at the proton-SOEC and the oxygen-SOEC system, respectively, indicating that the Hybrid-SOEC could produce more hydrogen and oxygen by electrolyzing water on both hydrogen and air electrodes. The amount of hydrogen and oxygen produced from the SOEC operation was also estimated from Faraday's law. Assuming 100% current efficiency, excellent hydrogen ($1.92 \text{ L h}^{-1} \text{ cm}^{-2}$) and oxygen ($0.96 \text{ L h}^{-1} \text{ cm}^{-2}$) production rate are achieved under the Hybrid-SOEC operating system at $700 \text{ }^\circ\text{C}$.

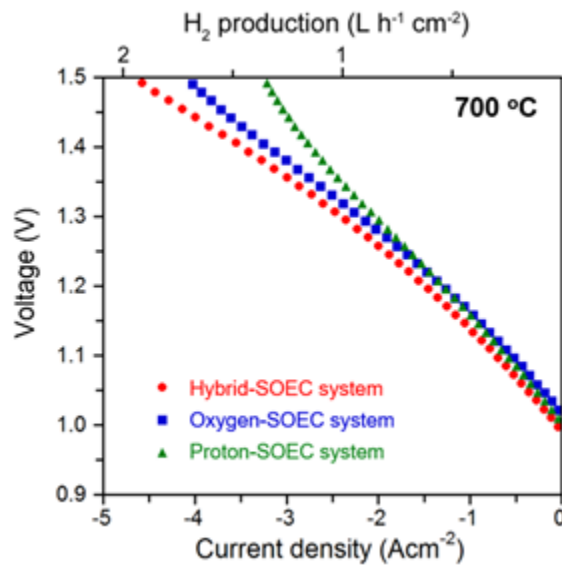


Figure 37 I-V curves for a Ni-BZCYYb/BZCYYb/NBSCF-BZCYYb cell under 90% H_2 and 10% steam fed in the hydrogen electrode side and 90% air and 10% steam fed in the air electrode side (red line, Hybrid-SOEC system), 90% H_2 and 10% steam fed in the hydrogen electrode side and 100% air fed in the air electrode side (blue line, oxygen-SOEC system), and 100% H_2 in the hydrogen electrode side and 90% air and 10% steam fed in the air electrode side (green line, proton-SOEC system) at $700 \text{ }^\circ\text{C}$.

To evaluate the stability of the Hybrid-SOEC, the cell voltage of the Hybrid-SOEC was recorded as a function of time under a constant current load of 0.45 A cm^{-2} at $550 \text{ }^\circ\text{C}$, as shown in Figure 38 (a). The cell voltage was relatively constant for more than 60 hours of continuous operation, indicating good stability of the Hybrid-SOEC under the condition for hydrogen production. After stability test of the Hybrid-SOEC at $550 \text{ }^\circ\text{C}$, the microstructures of the cell components are identified using scanning electron microscopy (SEM). Figure 38 (b)-(d) shows the micrographs of the Ni-BZCYYb / BZCYYb / NBSCF-BZCYYb cells. The BZCYYb electrolyte is dense and the interfaces between the electrodes and the electrolyte are well-connected; there was no observable cracks or delamination, indicating mechanical integrity of the Hybrid-SOEC under high humidity electrolysis operating conditions.

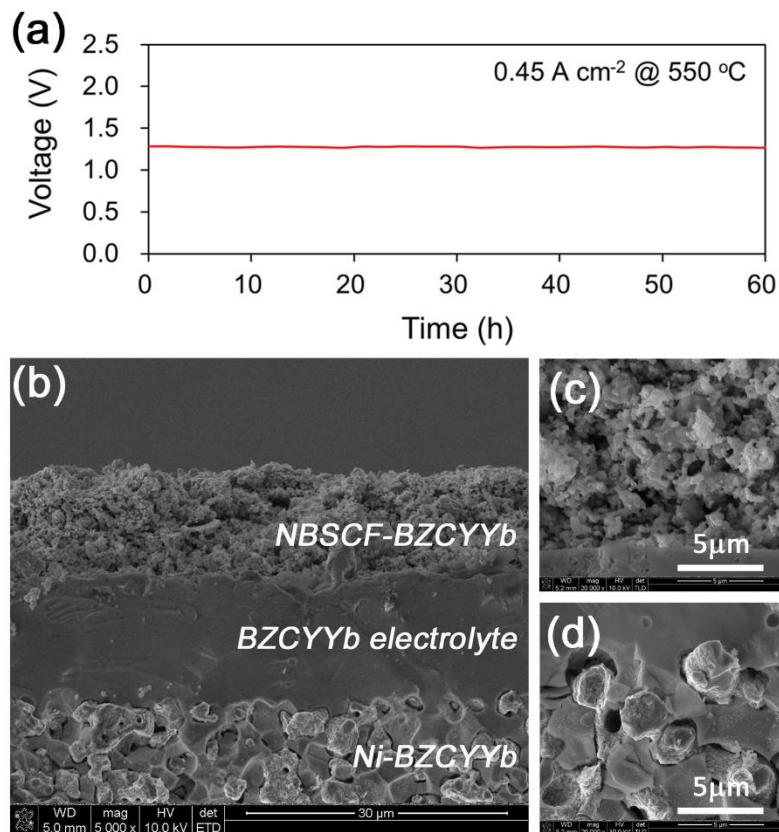


Figure 38 Stability test of single cell as a Hybrid-SOEC (a) Time-dependence of the cell voltage applied 0.45 A cm^{-2} at $550 \text{ }^\circ\text{C}$ during Hybrid-electrolysis under 90% H_2 and 10% steam fed in the hydrogen electrode and 90% air and 10% steam fed in the air electrode. The BZCYYb electrolyte is approximately $20 \text{ } \mu\text{m}$ thick and the NBSCF-BZCYYb composite air electrode is around $15 \text{ } \mu\text{m}$ thick. (b - d) SEM micrographs of Ni-BZCYYb / BZCYYb / NBSCF-BZCYYb cell as Hybrid-SOEC after stability at $550 \text{ }^\circ\text{C}$ during over 60 hours; (b) cross-sectional SEM micrograph of the fabricated cell after stability test, with BZCYYb electrolyte supported on Ni-BZCYYb hydrogen electrode, and NBSCF-BZCYYb air electrode; (c) microstructure of interface between NBSCF-BZCYYb and BZCYYb

electrolyte; (d) microstructure of interface between Ni-BZCYYb and BZCYYb electrolyte.

Figure 39 presents the electrochemical performance of the Hybrid-SOEC with other representative hydrogen production devices for comparison. Because each water-electrolysis device has different operating current ranges depending on the electrolyte media, the comparison has been made in high and low current range for the PEM-electrolysis ($\sim 2.0 \text{ A cm}^{-2}$, Figure 39 (a)) and the acidified water-electrolysis ($\sim 100 \text{ mA cm}^{-2}$, Figure 39 (b)), respectively. As shown in Figure 39 (a), the Hybrid-SOEC shows much lower overpotential than the PEM-electrolysis which typically uses Pt and Ir as catalysts.¹¹⁰ In addition, the comparison in the low-current range (Figure 39 (b)) reveals that the Hybrid-SOEC presents higher hydrogen evolution reaction (HER) performance than the acidified water-electrolysis system. Only 9 mV overpotential is required to attain 50 mA cm^{-2} in our Hybrid-SOEC system, meanwhile much higher overpotential is required to reach this current in the acidified water-electrolysis system using catalysts such as Pt (34 mV), PPy/MoS_x (58 mV), MoP|S (99 mV), and CoP (107 mV).¹¹¹⁻

114

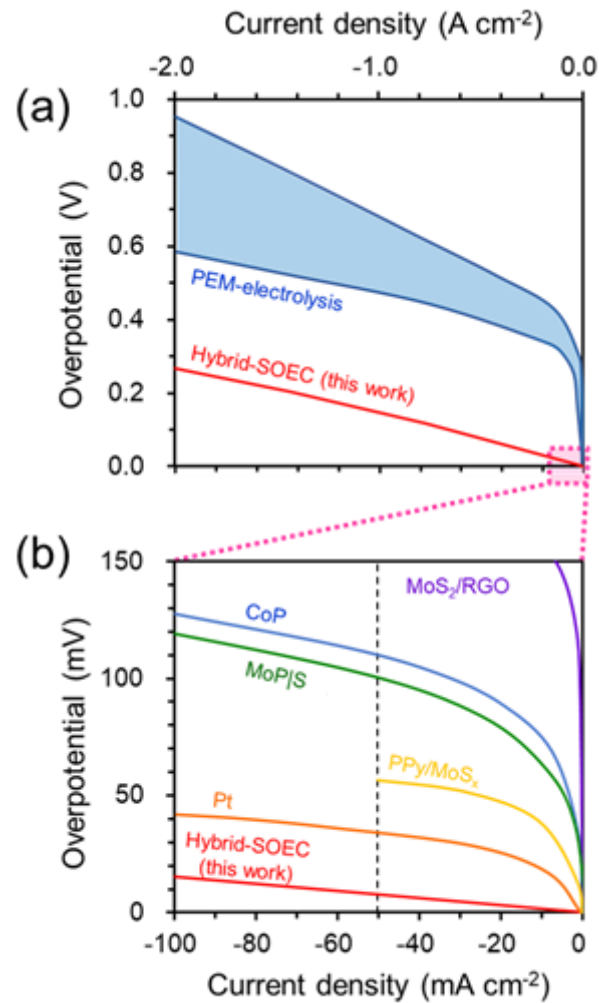


Figure 39 Comparison of the electrochemical performance of water-electrolysis by the Hybrid-SOEC and other representative applications. Polarization curves for the comparison with (a) the PEM-electrolysis using Ir anode and Pt cathode (performance range of the polymer electrolyte membrane (PEM)-electrolysis is colored by blue) and (b) acidified water-electrolysis using Pt, polypyrrole molybdenum sulfide (PPy/MoS_x), molybdenum phosphosulfide (MoP|S), and cobalt phosphide (CoP) catalyst.

5.4. Conclusions

In this study, we present the novel concept of “Hybrid solid oxide electrolysis cell (Hybrid-SOEC)” based on mixed ionic conducting electrolyte, BZCYYb, allowing simultaneous the oxygen-SOEC and proton-SOEC operation. The excellent stability is achieved under the Hybrid-SOEC operation without observable degradation for 60 h. Furthermore, in the Hybrid-SOEC system, the highest electrochemical performance for the hydrogen production was obtained among the reported SOEC and other representative water-electrolysis systems, implying that the Hybrid-SOEC represents a promising new

option for the cost-effective and highly efficient hydrogen production.

Chapter 6. The First Observation of Proton Trace in Triple Conducting Oxides: Thermodynamics and Kinetics of Proton

This chapter has not been published.

6.1. Introduction

Among the various type of fuel cells, ceramic fuel cells have been extensively studied as an eco-friendly alternative energy device in the aspect of high energy conversion efficiency and continuous production of the electricity without pollutant emissions. The high operating temperature ($> 800\text{ }^{\circ}\text{C}$) of conventional O^{2-} conducting ceramic fuel cells (solid oxide fuel cells, SOFCs), however, cause serious issues such as chemical inter-diffusion and high thermal stress. In this regard, protonic ceramic fuel cells (PCFCs) using proton conducting oxides (PCOs) have received great attention as promising candidates for the intermediate to low temperature operation ($400 \sim 800\text{ }^{\circ}\text{C}$) because of its relatively high ionic conductivity and low activation energy for the H^{+} transport compared with the O^{2-} transport in the conventional O^{2-} conducting oxides (YSZ, GDC, LSGM, and etc.)¹

After the first report of high-temperature proton conductivity in oxide material by Iwahara and co-workers in 1980s, many researchers have been investigated to utilizing the proton motion in solid oxides (so-called, “protonics” combining the proton and electronics) for the efficient PCFC operation. In the early stage of protonics research, the PCO electrolytes based on barium-zirconates and -cerates have been widely used as electrolyte materials. Among those PCO electrolytes, aliovalent-doped $\text{BaCe}_{1-x}\text{Zr}_x\text{O}_{3-\delta}$ ($0 < x < 1$) demonstrates high proton conductivity with overcoming their major issues such as poor sinterability and low proton conductivity under practical operating conditions.² Recently, a barium zirconate-cerate co-doped with Y and Yb, $\text{BaZr}_{0.1}\text{Ce}_{0.7}\text{Y}_{0.1}\text{Yb}_{0.1}\text{O}_{3-\delta}$ (BZCYYb), is reported with high ionic conductivity ($\sim 0.01\text{ S cm}^{-1}$) and excellent tolerance to sulfur poisoning and coking.³ However, the wide application of PCFCs is limited because of the cathodic polarization.⁴

Generally, mixed ionic (O^{2-}) and electronic conductors (MIECs) have been used as the cathode material for the conventional SOFC system because of their excellent electron conductivity and catalytic activities for the oxygen reduction reaction (ORR). However, when MIECs are used as PCFC cathodes, the electrochemically active site is limited into the interface between cathode and electrolyte, because the protons should diffuse from the PCO electrolyte to the cathode material in order to generate the electricity. Therefore, triple conducting oxides (TCOs) allowing the simultaneous transport of H^{+} , O^{2-} and e^{-} are required to effectively extend the electrochemically active sites to the entire surface of the cathode.

To increase the electrochemical performance of the TCOs, extensive efforts have been devoted with two primarily different approaches. The first approach is doping various altermultivalent elements into pure proton conducting oxides (*i.e.* BZO or BCO) to enhance their electrochemical activity for O^{2-} and e^- . For example, many trivalent ions are doped into the B-site of PCO to increase oxygen-ion kinetics, and O'Hayre group recently reported that transition-metal cations (Co and Fe) doped $BaZr_xY_{1-x}O_{3-\delta}$ presents great catalytic properties as the PCFC cathode by activating electronic conduction while maintaining protonic property of barium zirconates.⁵ Another approach for the development of TCO is finding MIEC (O^{2-}/e^-) materials having high protophilic properties. Since this approach has advantages that it is already well-studied on the electro-catalytic mechanism of O^{2-} and e^- in MIECs, many researchers have investigated to find protophilic MIECs for high performance PCFCs. Recently, our group reported that a layered perovskite material, $NdBa_{0.5}Sr_{0.5}Co_{1.5}Fe_{0.5}O_{5+\delta}$ (NBSCF), shows excellent electrochemical performance with low polarization resistance of $0.081 \Omega \text{ cm}^2$ at $700 \text{ }^\circ\text{C}$ under practical PCFC operating condition. Even though these efforts, the systematic development of TCOs is very difficult because of characterization challenges of protonics in the TCOs, as below reasons.

In order to identify the protonic behavior of PCOs (*i.e.*, H^+ -conducting electrolyte materials), the electromotive force (EMF) method is used through the measurement of open-circuit voltage (OCV) for concentration cells. For the TCOs, However, it is difficult to measure the protonic properties by the EMF method because of their large electron conductivity. In addition, it is very complicated to analyze the thermodynamics and kinetics properties of TCOs, because not only H^+ , but also O^{2-} and e^- are simultaneously affect the cathodic performance of PCFCs. To overcome these complexities of the characterization for protonics in TCOs, it could be an effective candidate to study the proton properties of MIEC materials. The MIECs have been already well-optimized and -studied on their electrochemical reaction mechanism of O^{2-} and e^- in the ceramic fuel cell system in many literatures, therefore, the protonic properties of TCOs can be understood more clearly.

In this study, for the first time, we comprehensively identified both thermodynamic and kinetic properties of protonics for the TCO, $PrBa_{0.5}Sr_{0.5}Co_{1.5}Fe_{0.5}O_{5+\delta}$ (PBSCF). The diffusion coefficient of proton of PBSCF is identified with isotope exchange method using the time-of-flight secondary ion mass spectroscopy (TOF-SIMS). For thermodynamic property, protonation enthalpy of the PBSCF is evaluated by TGA. To evaluate the electrochemical performance, single cell test is performed using the PBSCF as a PCFC cathode material.

6.2. Experimental Section

Synthesis of electrolyte and electrode powders: The Pechini method was used to synthesize $\text{PrBa}_{0.5}\text{Sr}_{0.5}\text{Co}_{1.5}\text{Fe}_{0.5}\text{O}_{5+\delta}$ (PBSCF). The desired composition was obtained by each dissolving nitrate salts in distilled water with the addition of ethylene glycol and quantitative amounts of citric acid. After a viscous resin was formed, the mixture was heated to 250 °C in air followed by combustion to make fine powders, which were calcined for 4 hours at 600 °C and ball-milled for 24 hours in acetone. The typical solid state reaction was used to synthesize $\text{BaZr}_{0.1}\text{Ce}_{0.7}\text{Y}_{0.1}\text{Yb}_{0.1}\text{O}_{3-\delta}$ (BZCYYb) powders. Stoichiometric amounts of barium carbonate, cerium oxide, zirconium oxide, yttrium oxide powders, and ytterbium oxide (all from Aldrich Chemicals) were mixed by ball milling process, followed by sintering at 1100 °C for 10 hours in air. The glycine nitrate process (GNP) The NiO powders were used for the hydrogen electrode. Stoichiometric amounts of nitrates with a proper amount of glycine were dissolved in distilled water. The solutions were heated up to 350 °C and followed by combustion to make powders.

Preparation of sample for SEM and XRD analysis: PBSCF-BZCYYb mixtures are sintered at 950 °C in air for 4 hours, in order to investigate the chemical reactivity between the PBSCF and BZCYYb. (Figure 40) The chemical reactivity of PBSCF and BZCYYb was checked by an X-ray diffractometer (Rigaku diffractometer, Cu $K\alpha$ radiation). The microstructures and cross-section images of the NiO-BZCYYb/BZCYYb/PBSCF single cell was observed using field emission scanning electron microscopy (Nova Nano SEM, FEI, USA). (Figure 41)

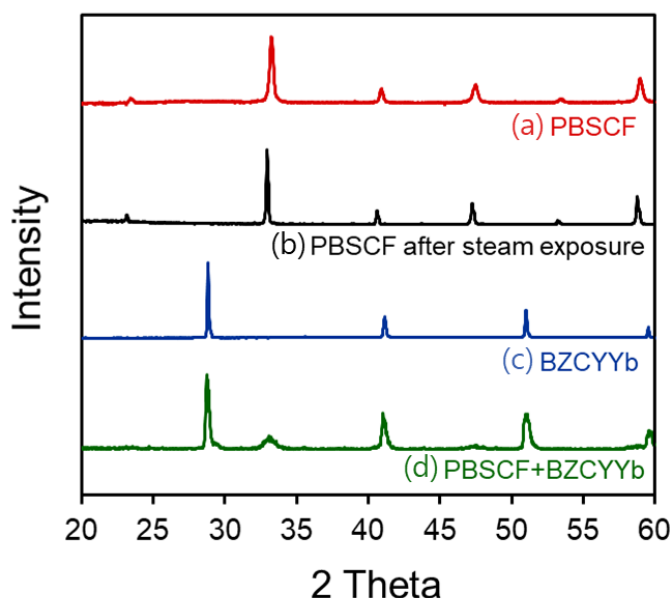


Figure 40 XRD diffraction pattern of (a) PBSCF sintered at 1150 °C for 12 h, (b) PBSCF after steam exposure (10 vol% H_2O containing air) for 100 h at 650 °C, (c) BZCYYb sintered at 1400 °C for 4 h, and (d) a mixture of PBSCF and BZCYYb sintered at 950 °C 4h.

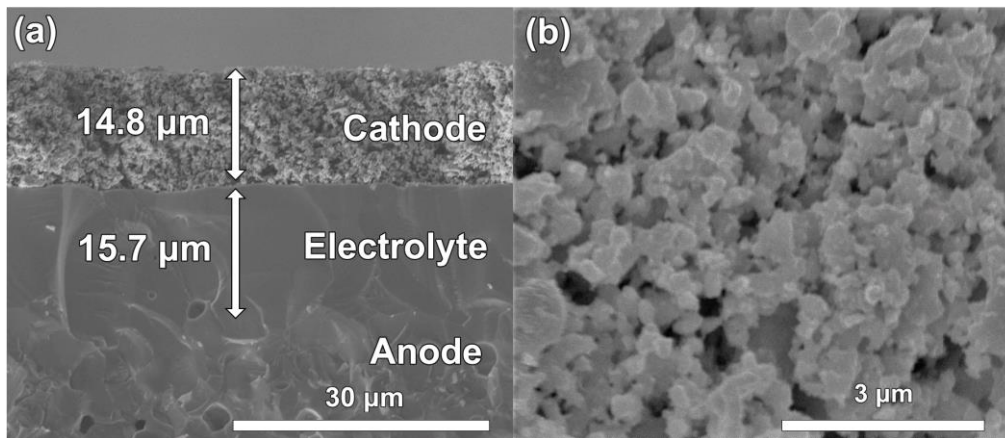


Figure 41 (a) Cross-sectional SEM image of PBSCF/BZCYYb/NiO-BZCYYb cell. (b) SEM image of porous PBSCF cathode

Fabrication of single cell: The NiO-BZCYYb anode-supported cell was fabricated for the measurement of the electrolysis durability and performance. The calcined PBSCF and BZCYYb powders were mixed by ball-milling at weight ratio of 8:2, blended with a binder (Heraeus V006) for air electrode slurries. NiO-BZCYYb supported cells were fabricated by the drop-coating method. The NiO-BZCYYb hydrogen electrode was prepared by a mixture of NiO and BZCYYb (weight ratio of 6.5:3.5) after being ball-milled for 24 hours in ethanol. The BZCYYb suspension was applied to the NiO-BZCYYb support by drop-coating, followed by drying in air and co-sintering at 1400 °C for 4 hours. Air electrode slurries were screen-printed onto the surface of the BZCYYb electrolyte and were finally sintered 950 °C in air for 4 hours.

Time-of-flight secondary ion mass spectrometry: Isotope proton exchange was measured with 10 vol% D₂O-containing air in the range of 250~550 °C. The D₂O-exchanged samples were analyzed by time-of-flight secondary ion mass spectrometry (ToF-SIMS) on a Ion ToF-SIMS 5 (ION-TOF GmbH, Münster, Germany). A 25 keV Bi⁺ primary ion beam of 1.10 pA current was used to generate the secondary ions for analysis and a Cs⁺ beam (2 kV) incident for sputtering. Hydrogen depth profiles were investigated from the exchanged surface of sample by sputter depth profiling. After ToF-SIMS analysis, the crater depth was measured using a KLA-Tencor P6 surface profilometer. (Figure 42)

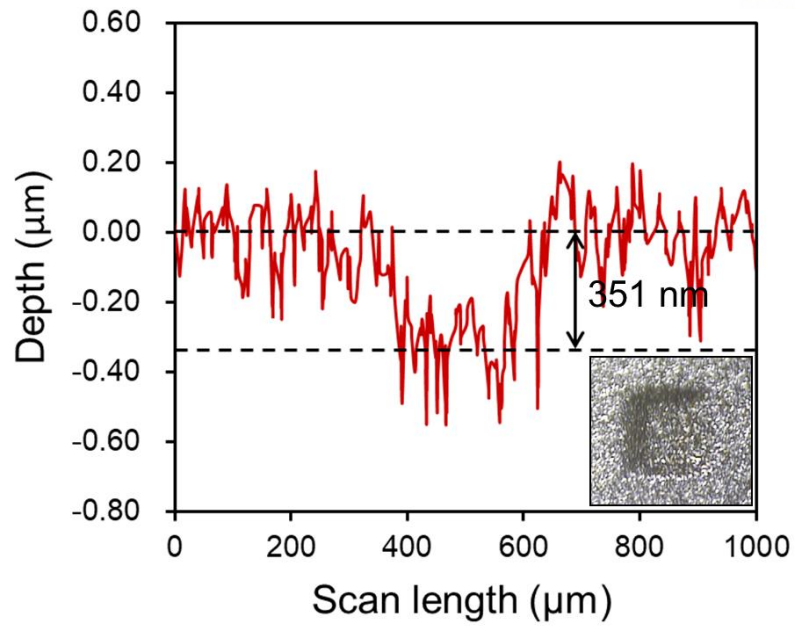


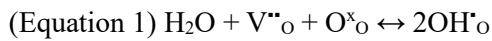
Figure 42 Surface profile data of the PBSCF pellet after ToF-SIMS measurement. Inset image shows the crater on the PBSCF surface after Cs^+ beam sputtering.

Thermogravimetric analysis: The concentration of protonic defects was determined by thermogravimetric analysis (TGA). The sintered powders were heated to 800 °C and held until it reached a thermal equilibrium state to remove water from the structure. The weight changes of samples between under dry and wet air ($P_{\text{H}_2\text{O}}=0.023$ atm) were collected every 100 °C from 800 °C to 500 °C with a 2 h stabilization time at each temperature. Thermogravimetric analysis (TGA) data were logged on the SDT-Q600 device from TA. Measurements were carried out on samples in platinum crucibles under dry-air and wet-air saturated by bubbling in water at 25 °C

Electrochemical performances: For the single cell tests, Ag wires were attached at the cathode and anode side using Ag paste as a current collector. The NiO-BZCYYb anode-supported single cell was sealed fully onto one end of the alumina tube using a ceramic adhesive (Aremco, Ceramabond 552). Humidified H_2 (3% H_2O) was applied to the anode side as a fuel through a water bubbler with a flow rate of 100 mL min^{-1} , while air was supplied as an oxidant to the cathode during the single cell test. The impedance spectra and I - V curves were acquired with a BioLogic Potentiostat and analyzed with EC-lab software.

6.3. Results and Discussion

To determine the surface adsorption and diffusion behavior of the proton for the PBSCF, the isotope-exchange treatment was performed under precise control of temperature and D₂O vapor pressure. As schematically shown in Figure 43, the dense PBSCF pellet (98.5% theoretical density) was polished for uniform D₂O adsorption onto the surface, followed by heat-treatment under 10 vol% D₂O-containing air in the range of 250 ~ 650 °C. When D₂O-containing air was supplied, proton uptake reaction is occurred due to the D₂O uptake reaction of PBSCF, as shown below:⁵⁸



Surface analysis and depth profiling measurements were performed after the D₂O-exchange treatment by the time of flight secondary ion mass spectrometry (ToF-SIMS) for the protonic behavior evaluation on the PBSCF surface and bulk.

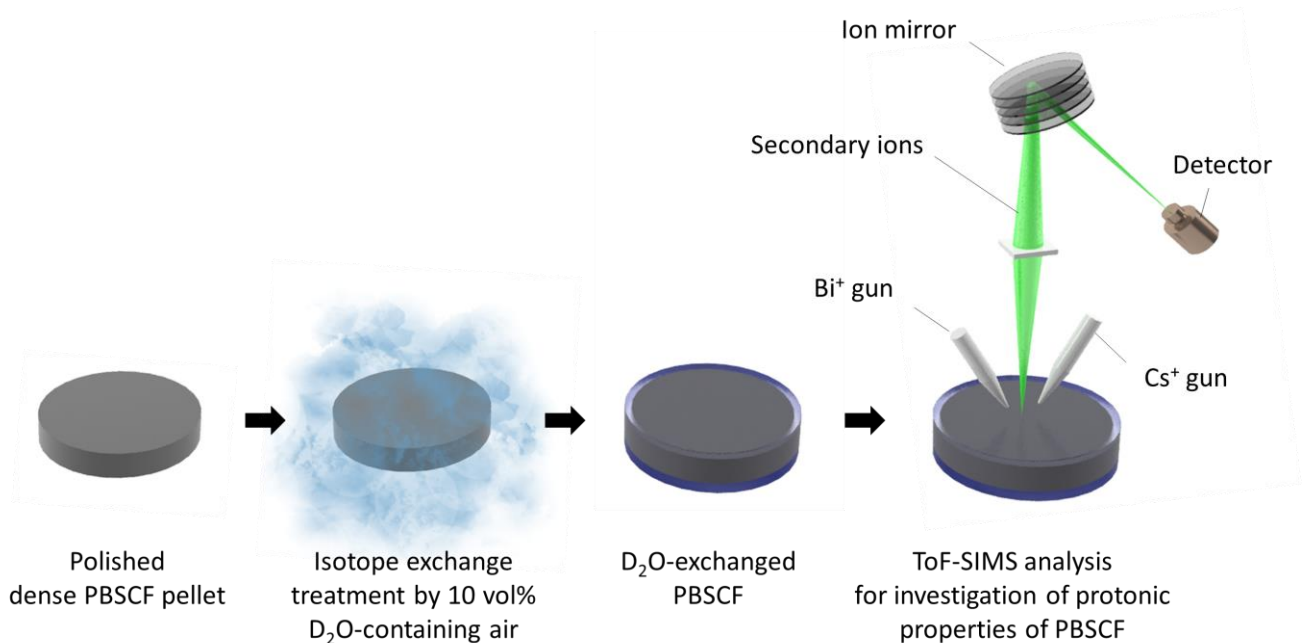


Figure 43 Schematic illustration of preparation of the D₂O-exchanged PBSCF for the ToF-SIMS measurement.

Figure 44a presents the surface analysis results obtained by the ToF-SIMS for the investigation of protonic behavior on the PBSCF surface. As shown in the ToF-SIMS mass spectrum data, the D⁻ (m/z=2.014) and OD⁻ (m/z=18.009) signals are successfully detected from the surface of D₂O-exchanged PBSCF, and the mass resolution is sufficient to separate between the OD⁻ and ¹⁸O⁻ (m/z =

17.999). Only D^- and OD^- peaks are observed after the D_2O -exchange treatment, indicating that the exchange process forms D^- and OD^- ions on the surface. The protonic reaction on the surface of PBSCF is also revealed on the secondary ion mapping images, as shown in Figure 44b-e. In the ToF-SIMS images (see Figure 44b-e), bright yellow and dark red colors represent the high and low concentration of observed ion species, respectively. The D^- and OD^- species are clearly observed over the entire surface of the PBSCF sample as presented in Figure 1c and e, indicating that the proton defect formation reaction (eq. 1) homogeneously occurs on the surface.

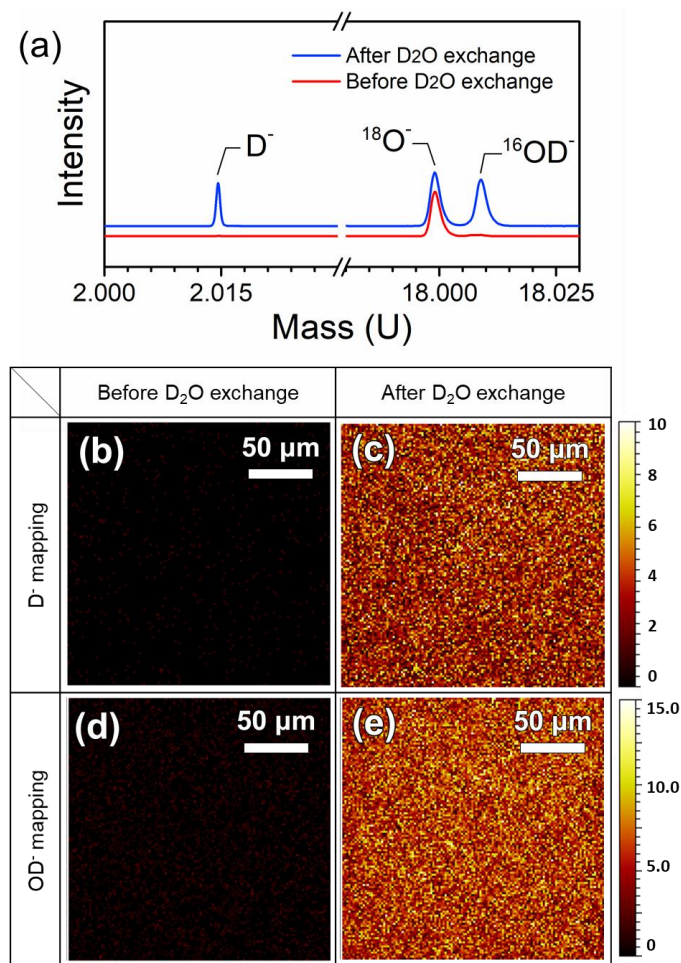


Figure 44 Protonic properties of the surface of PBSCF pellet measured by ToF-SIMS. (a) Mass spectrum analysis of a D_2O -exchanged PBSCF around $U = 2$ and 18. (b-e) Secondary ion mapping images of D^- and OD^- for the surface of PBSCF pellet before (b, d) and after D_2O (c, e) exchange.

In order to analyze the bulk diffusion kinetics of the proton at TCO, the isotope exchange depth profile (IEDP) of deuterium for the D_2O -exchanged PBSCF was measured. The 3D-mapping image of

OD⁻ (Figure 45a) clearly shows that the protons are uniformly diffused in the depth direction of the PBSCF. Figure 45b and c show the normalized OD⁻ tracer diffusion profiles, and these experimental data can be fitted to Fick's second law with the semi-infinite model since the in-diffusion of deuterium was shorter than half of the PBSCF sample thickness:¹¹⁵

$$\text{(Equation 2) } C'(x) = \operatorname{erfc}\left(\frac{x}{2\sqrt{D^*t}}\right) - \exp(hx + h^2D^*t) \times \operatorname{erf}\left\{\left(\frac{x}{2\sqrt{D^*t}}\right) + (h\sqrt{D^*t})\right\}$$

where h is the ratio of the surface exchange coefficient (k^*) to the diffusion coefficient (D^*) and t is the anneal time. The $C'(x)$ is the normalized deuterium isotopic concentration calculated from:

$$\text{(Equation 3) } C'(x) = \frac{C(x) - C_{bg}}{C_g + C_{bg}}$$

where $C(x)$, C_g , and C_{bg} are deuterium fraction, deuterium concentration in air, and background isotope fraction, respectively. The calculated D^* and k^* values are presented in Figure 45d, e. Diffusion coefficient value of proton (D^*_H) increases with increasing temperature due to thermally activated motion of the proton (Figure 45d). Meanwhile, unlike the surface exchange behavior of O²⁻ for general MIEC materials, the surface exchange coefficient value of the proton (k^*_H) is reduced with increasing temperature (Figure 45e) because the proton uptake at the surface is an exothermic reaction.¹¹⁶ The proton diffusion coefficient (D^*_H) of PBSCF shows excellent value of $1.04 \times 10^{-6} \text{ cm}^2/\text{s}$ at 550 °C which is much higher than the O²⁻ diffusion coefficients (D^*_O) of other representative SOFC cathode materials (Figure 45f), such as Ba_{0.5}Sr_{0.5}Co_{0.8}Fe_{0.2}O_{3- δ} (BSCF), La_{0.6}Sr_{0.4}Co_{0.2}Fe_{0.8}O_{3- δ} (LSCF), and La_{0.6}Sr_{0.4}CoO_{3- δ} (LSC) ($1.63 \times 10^{-9} \sim 3.01 \times 10^{-11} \text{ cm}^2/\text{s}$).^{22,117-120}

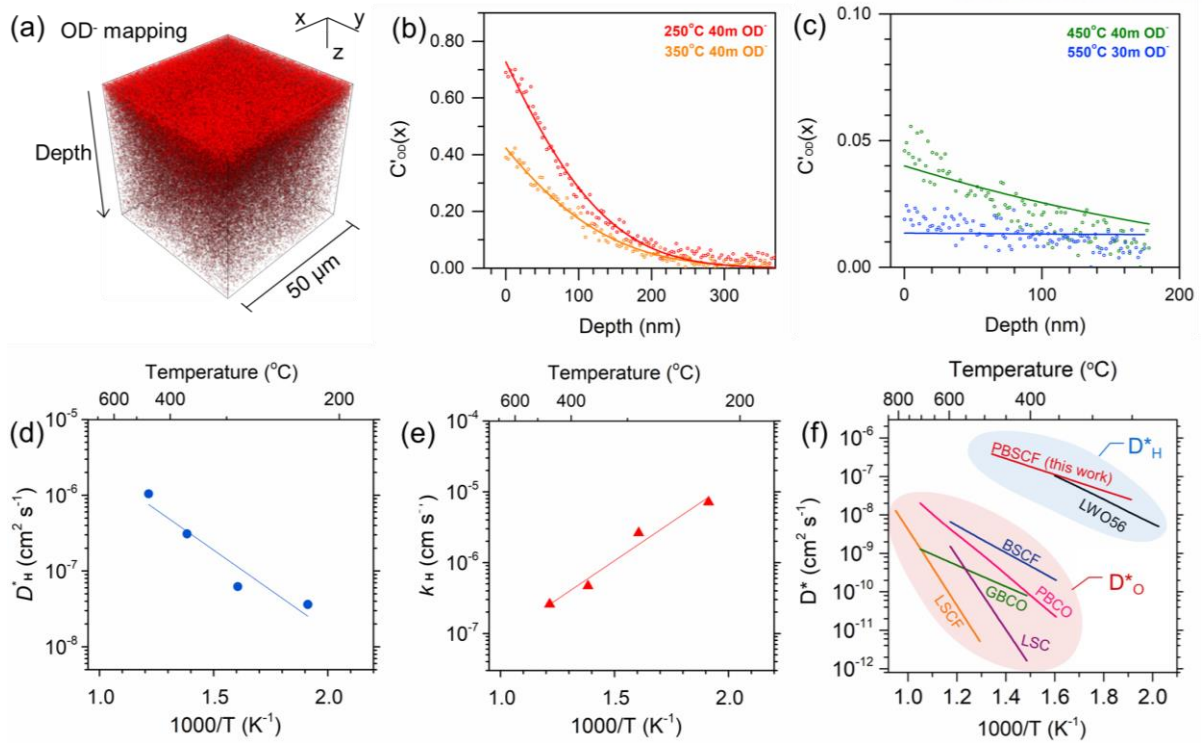


Figure 45 (a) 3D-mapping image of OD⁻ ion intensity in the 50 × 50 μm of the analysis area for D₂O-exchanged PBSCF sample annealed at 350 °C. (b) and (c) Normalized OD⁻ depth profile obtained from D₂O-exchanged PBSCF annealed at a temperature range of 250 ~ 550 °C. The solid lines represent the best fit to the Fick's second law. (d) and (e) Diffusion and kinetics coefficient of proton (D_{H}^* and k_{H}^*) values of the PBSCF sample. (f) Comparison of diffusion coefficients (D_{H}^*) of the PBSCF with other representative MIEC materials: Ba_{0.5}Sr_{0.5}Co_{0.8}Fe_{0.2}O_{3-δ} (BSCF), PrBaCo_{2.0}O_{5+δ} (PBCO), GdBaCo_{2.0}O_{5+δ} (GBCO), La_{0.6}Sr_{0.4}CoO_{3-δ} (LSC), La_{0.6}Sr_{0.4}Co_{0.2}Fe_{0.8}O_{3-δ} (LSCF), and La_{27.15}W_{4.85}O_{55.28}V_{0.73} (LWO). Solid lines in the red and blue circle represent D^* values for oxygen ion and proton, respectively.

For thermodynamic study of the protonics in PBSCF, thermogravimetric analysis (TGA) was performed in the temperature range of 500 ~ 800 °C. When humidified air (3 vol% H₂O) is supplied onto the sample under an isothermal condition, weight increase of the PBSCF is observed due to the hydration reaction (Equation 1, Figure 46), so that the equilibrium constant (K_{OH}) for the hydration reaction can be obtained as shown below,

$$\text{(Equation 4) } K_{\text{OH}} = [\text{OH}^*_{\text{o}}]^2 / (p\text{H}_2\text{O}[\text{V}^{*}_{\text{o}}][\text{O}^{\times}_{\text{o}}])$$

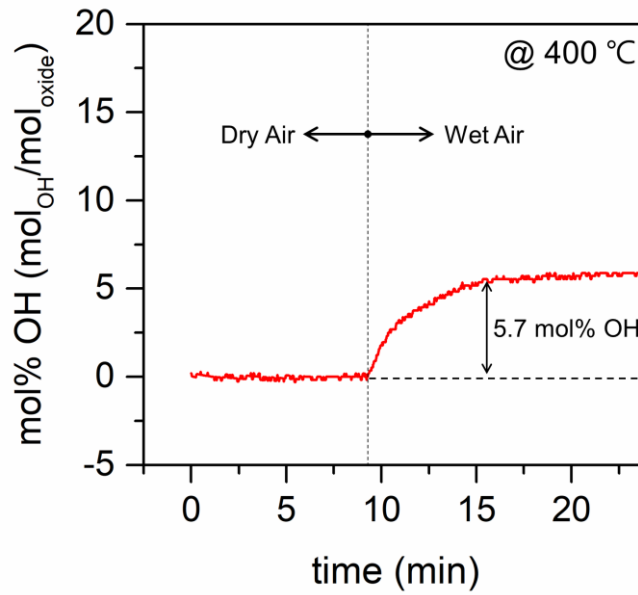


Figure 46 Proton defect formation of PBSCF measured by the water-uptake properties of TCOs through thermogravimetric analysis (TGA) at 400 °C under dry air and 3 vol% H₂O air. Concentrations are given in unit of [(OH mol concentration)/(PBSCF mol concentration)]

The equilibrium constants (K_{OH}) for the proton uptake reaction show the Arrhenius behavior, so the enthalpy of the proton defect formation (ΔH) for the PBSCF was evaluated from the hydration isobars (Figure 47a) using the following Van't Hoff equation,¹²¹

$$\text{(Equation 5)} \quad \ln(K_{OH}) = -\frac{\Delta H}{RT} + \frac{\Delta S}{R}$$

where R and T are the universal gas constant and temperature (K), respectively. For comparison, ΔH values of the representative PCOs are presented in Figure 47b. The lower negative values of ΔH (i.e., more exothermic) could indicate that the hydration reaction is more favorable because of the exothermic hydration reaction and the relationship between the dissolved hydroxyl group and the lattice oxygen.¹²² In the temperature range of 500~800 °C, the ΔH of proton defect formation for the PBSCF is -52.53 kJ/mol, indicating that the PBSCF has favorable proton uptake properties compared to other barium-zirconates (-65~-25 kJ/mol).^{121,123,124}

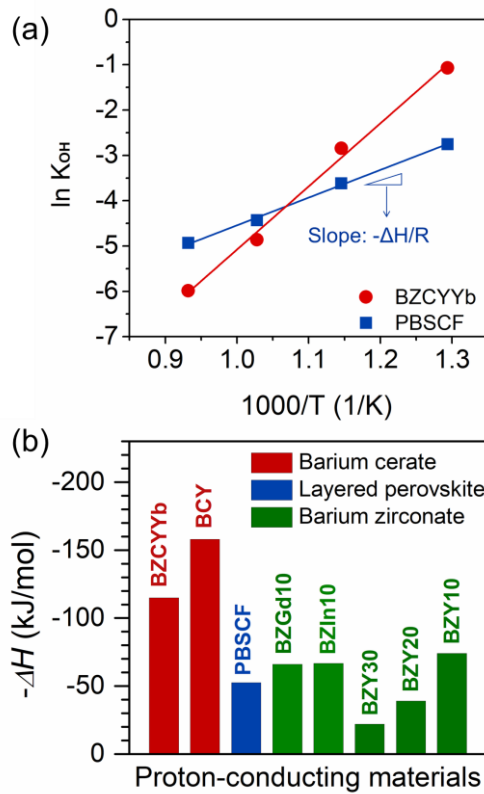


Figure 47 (a) Equilibrium constant of hydration reaction presented in the Arrhenius plot. The slope yields hydration enthalpy (ΔH). (b) ΔH values of various proton-conducting oxides for comparison.

Figure 48 presents the electrochemical performance of the single cell using a PBSCF/BZCYYb/NiO-BZCYYb configuration. As can be expected from the favorable protonic kinetic and thermodynamic properties of the PBSCF obtained from our experimental results, an excellent non-ohmic resistance of $0.088 \Omega \text{ cm}^2$ and a maximum power density (MPD) value of 1.23 W/cm^2 were obtained at $650 \text{ }^\circ\text{C}$ (Figure 48 4a and b). Notably, the PBSCF single cell shows a power density of 0.42 W/cm^2 even at $500 \text{ }^\circ\text{C}$, which is higher than the required power density of 0.25 W/cm^2 for efficient operation.¹²⁵ As shown in Figure 48 4c, this efficient performance at low temperatures ($\sim 600 \text{ }^\circ\text{C}$) enable cost-efficient manufacturing by widening material choices (e.g., metallic interconnects, non-ceramic seals) and eliminating major performance degradation.⁵³

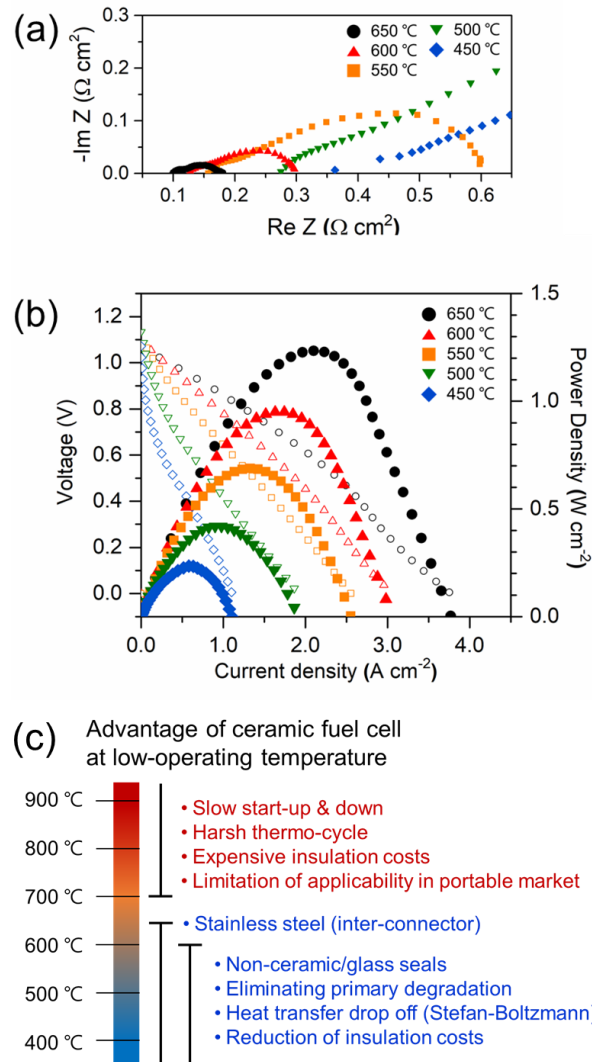


Figure 48 (a) Impedance spectra of the single cell (PBSCF/BZCYYb/NiO-BZCYYb) measured under open-circuit condition. (b) I-V curve and corresponding power density curves of the single cell at various temperatures. (c) Advantages and disadvantages of ceramic fuel cells by operating temperature.

6.4. Conclusion

In the present study, both kinetic and thermodynamic properties for the protonics of triple conducting oxide (TCO) were comprehensively investigated using the ToF-SIMS and TGA. Interestingly, we found that the proton formation and transport properties were observed on both surface and bulk of the layered perovskite, PBSCF. This layered perovskite presents an excellent D_{H}^* value of $1.04 \times 10^{-6} \text{ cm}^2/\text{s}$ at 550°C which is two orders of magnitude higher than oxygen diffusion coefficient (D_{O}^*) values of other representative MIEC perovskite materials. Thermodynamically, the PBSCF has a favorable enthalpy value (ΔH) of proton defect formation (-52.53 kJ/mol) compared to other proton-conducting oxide materials, such as barium-zirconates ($-65 \sim -25 \text{ kJ/mol}$). Based on these protonic properties, an efficient operation was possible even at the low-temperature (500°C). We believe that this first study on the kinetics and thermodynamics of TCO, could provide a useful guideline for methodology to understand the protonics and development of PCFCs.

List of Publications

16. Hybrid-Solid Oxide Electrolysis Cell: A New Strategy for Efficient Hydrogen Production

Junyoung Kim[†], Areum Jun[†], Ohhun Gwon, Seonyoung Yoo, Meilin Liu, Jeeyoung Shin, Tak-Hyoung Lim*, and Guntae Kim*

Nano Energy (2017) DOI: 10.1016/j.nanoen.2017.11.074

15. Achieving High Efficiency and Eliminating Degradation in Solid Oxide Electrochemical Cells using High Oxygen-Capacity Perovskite

Areum Jun, **Junyoung Kim**, Jeeyoung Shin, and Guntae Kim*

Angewandte Chemie International Edition (2016) DOI: 10.1002/anie.201606972

14. A Robust Symmetrical Electrode with Layered Perovskite Structure for Direct Hydrocarbon Solid Oxide Fuel Cells: $\text{PrBa}_{0.8}\text{Ca}_{0.2}\text{Mn}_2\text{O}_{5+\delta}$

Sihyuk Choi, Sivaprakash Sengodan, Seonhye Park, Young-wan Ju, **Junyoung Kim**, Junji Hyodo, HuYoung Jeong, Tatsumi Ishihara, Jeeyoung shin* and Guntae Kim*

Journal of Materials Chemistry A (2016) DOI: 10.1039/C5TA08878J

13. Investigation of a Layered Perovskite for IT-SOFC Cathodes: B-Site Fe-Doped $\text{YBa}_{0.5}\text{Sr}_{0.5}\text{Co}_{2-x}\text{Fe}_x\text{O}_{5+\delta}$

Sangwook Joo, **Junyoung Kim**, Jeeyoung Shin*, Tak-Hyoung Lim*, and Guntae Kim*

Journal of Electrochemical Society, (2016) DOI: 10.1149/2.0371614jes

12. (Review paper) Perovskite as a Cathode Material: A Review of its Role in the Highly Reliable SOFC Technology

Areum Jun, **Junyoung Kim**, Jeeyoung Shin*, and Guntae Kim*

ChemElectroChem (2016) DOI: 10.1002/celc.201500382

11. Nanostructured Double Perovskite Cathode with Low Sintering Temperature for Intermediate Temperature Solid Oxide Fuel Cells

Seona Kim, Areum Jun, Ohhun Kwon, **Junyoung Kim**, Seonyoung Yoo, Hu Young Jeong, Jeeyoung Shin, and Guntae Kim*

ChemSusChem (2015) DOI: 10.1002/cssc.201500509/

10. Effects of composite cathode on electrochemical and redox properties for intermediate-temperature solid oxide fuel cells

Changmin Kim, **Junyoung Kim**, Jeeyoung Shin, Guntae Kim*

International Journal of Hydrogen Energy (2014) 39(35):20812-20818.

9. Triple-Conducting Layered Perovskites as Cathode Materials for Proton-Conducting Solid Oxide Fuel Cells

Junyoung Kim, Sivaprakash Sengodan, Goeun Kwon, Dong Ding, Jeeyoung Shin, Meilin Liu, Guntae Kim*

ChemSusChem (2014) DOI: 10.1002/cssc.201402351

8. Decreasing Interfacial Losses with Catalysts in $\text{La}_{0.9}\text{Ca}_{0.1}\text{FeO}_{3-\delta}$ Membranes for Syngas Production

Anthony S. Yu, **Junyoung Kim**, Tae-Sik Oh, Guntae Kim, Raymond J. Gorte*, John M. Vohs*

Applied Catalysis A: General (2014) DOI: 10.1016/j.apcata.2014.08.028

7. Chemically Stable Perovskites as Cathode Materials for Solid Oxide Fuel Cells: La-Doped $\text{Ba}_{0.5}\text{Sr}_{0.5}\text{Co}_{0.8}\text{Fe}_{0.2}\text{O}_{3-\delta}$

Junyoung Kim, Sihyuk Choi, Areum Jun, Hu Young Jeong, Jeeyoung Shin, Guntae Kim*

ChemSusChem (2014) DOI: 10.1002/cssc.201301401

6. Effect of Fe Doping on Layered $\text{GdBa}_{0.5}\text{Sr}_{0.5}\text{Co}_2\text{O}_{5+\delta}$ Perovskite Cathodes for Intermediate Temperature Solid Oxide Fuel Cells

Junyoung Kim, Areum Jun, Jeeyoung Shin, Guntae Kim*

Journal of the American Ceramic Society (2013) DOI: 10.1111/jace.12692

5. Electrochemical properties of an ordered perovskite $\text{LaBaCo}_2\text{O}_{5+\delta}-\text{Ce}_{0.9}\text{Gd}_{0.1}\text{O}_{2-\delta}$ composite cathode with strontium doping for intermediate-temperature solid oxide fuel cells

Sihyuk Choi, Seonhye Park, **Junyoung Kim**, Tak-Hyoung Lim, Jeeyoung Shin, Guntae Kim*

Electrochemistry Communications (2013) DOI: 10.1016/j.elecom.2013.04.016

4. Highly efficient and robust cathode materials for low-temperature solid oxide fuel cells: $\text{PrBa}_{0.5}\text{Sr}_{0.5}\text{Co}_{2-x}\text{Fe}_x\text{O}_{5+\delta}$

Sihyuk Choi, Seonyoung Yoo, Jiyoun Kim, Seonhye Park, Areum Jun, Sivaprakash Sengodan, **Junyoung Kim**, Jeeyoung Shin, Hu Young Jeong, Yongman Choi, Guntae Kim*, Meilin Liu*

Scientific Reports (2013) DOI: 10.1038/srep02426

3. Investigation of layered perovskite type $\text{NdBa}_{1-x}\text{Sr}_x\text{Co}_2\text{O}_{5+\delta}$ ($x = 0, 0.25, 0.5, 0.75, \text{ and } 1.0$) cathodes for intermediate-temperature solid oxide fuel cells

Seonyoung Yoo, Sihyuk Choi, **Junyoung Kim**, Jeeyoung Shin, Guntae Kim*

Electrochimica Acta (2013) DOI: 10.1016/j.electacta.2013.03.041

2. Optimization of Sr content in layered $\text{SmBa}_{1-x}\text{Sr}_x\text{Co}_2\text{O}_{5+\delta}$ perovskite cathodes for intermediate-temperature solid oxide fuel cells

Areum Jun, **Junyoung Kim**, Jeeyoung Shin, Guntae Kim*

International Journal of Hydrogen Energy (2012) DOI: 10.1016/j.ijhydene.2012.09.048

1. Strontium Doping Effect on High-Performance $\text{PrBa}_{1-x}\text{Sr}_x\text{Co}_2\text{O}_{5+\delta}$ as a Cathode Material for IT-SOFCs

Seonhye Park, Sihyuk Choi, **Junyoung Kim**, Jeeyoung Shin, Guntae Kim*

ECS Electrochemistry Letters (2012) DOI: 10.1149/2.007205eel

Acknowledgements

I would like to thank all the people who made this dissertation possible, unforgettable experiences and memories for me. Although there is only my name is on the cover, many people have contributed to the research and supported my life in their own way and for that I want to give them special thanks.

Foremost, I would like to express my sincere gratitude to my advisor Prof. Guntae Kim for the continuous support of my Ph.D study and research, for his patience, motivation, enthusiasm and immense knowledge. His guidance helped me in all the time of research and writing of this dissertation I could not have imagined having a better advisor and mentor for my Ph.D study.

Besides my advisor, I would like to thank the all my committee members: Prof. Jong-Beom Baek, Prof. Sang-Young Lee, Prof. Hu Young Jeong, and Prof. Jeeyoung Shin for very gracious and generous with their time, ideas, their encouragement, and insightful comments.

My great co-advisor, Professor Jeeyoung Shin has been always there to listen and give advice. I am deeply grateful to him for the long discussions that helped me sort out the technical details of my research.

I am also grateful to my gunslab members for their many helps and great memories: Dr. Sivaprakash Sengodan, Dr. Yunfei Bu, Dr. Arunchander Asokan, Seonna Kim, Ohhun Gwon, Chaehyun Lim, Ohhun Kwon, Changmin Kim, Donghwi Jeong, Sangwook Joo, Jeongwon Kim, Hyunmin Kim, Seongtae Lee, Hansol Lee, Arim Seong, Yejin Yang, and Daeun Lee.

I appreciate my friends for always standing by my side and for always making me feel happy. They gave me the belief that I can overcome difficulties even when I am in the darkest time. Special thanks to my friends (Taekyoung Woo, Seongheon Kang, Ohkyun Kwon, Miyoung Bae, Kyungryeol Ha), UNIST friends (Yoonkyo Cho, Sehee Kim, Joomyoung Kim, Hyoki Hong), KNU friends (Hyejin Kim, Hoyoung Yoon, Seongchang Shin, Jeongha Lee Juhyun Bae, Hochang Lee), and UNIST graduate student football team, FC SIGMA.

Nobody has been more important to me in pursuing my Ph.D research than my family. I would like to thank my parents, whose love and guidance are with me in whatever I pursue. Mom, for constant love and immeasurable sacrifice. Dad, for perspective and the will to strive. Jaeyoung, for unstinting support and brotherhood. Tako, for keeping my mind calm and always being there.

References

- (1) Kreuer, K.-D. Proton Conductivity: Materials and Applications. *Chem. Mater.* **1996**, *8* (3), 610–641.
- (2) Medvedev, D. a.; Lyagaeva, J. G.; Gorbova, E. V.; Demin, a. K.; Tsiakaras, P. Advanced Materials for SOFC Application: Strategies for the Development of Highly Conductive and Stable Solid Oxide Proton Electrolytes. *Prog. Mater. Sci.* **2016**, *75*, 38–79.
- (3) Yang, L.; Wang, S.; Blinn, K.; Liu, M.; Liu, Z.; Cheng, Z.; Liu, M. Enhanced Sulfur and Coking Tolerance of a Mixed Ion Conductor for SOFCs: BaZr_{0.1}Ce_{0.7}Y_{0.2}-XYbxO_{3-δ}. *Science (80-)*. **2009**, *326* (5949), 126–129.
- (4) Hossain, S.; Abdalla, A. M.; Jamain, S. N. B.; Zaini, J. H.; Azad, A. K. A Review on Proton Conducting Electrolytes for Clean Energy and Intermediate Temperature-Solid Oxide Fuel Cells. *Renew. Sustain. Energy Rev.* **2017**, *79* (May), 750–764.
- (5) Duan, C.; Tong, J.; Shang, M.; Nikodemski, S.; Sanders, M.; Ricote, S.; Almansoori, a.; O’Hayre, R. Readily Processed Protonic Ceramic Fuel Cells with High Performance at Low Temperatures. *Science (80-)*. **2015**, *349* (6254).
- (6) Kim, J.; Sengodan, S.; Kwon, G.; Ding, D.; Shin, J.; Liu, M.; Kim, G. Triple-Conducting Layered Perovskites as Cathode Materials for Proton-Conducting Solid Oxide Fuel Cells. *ChemSusChem* **2014**, *7*, 2811–2815.
- (7) Kim, J.; Jun, A.; Gwon, O.; Yoo, S.; Liu, M.; Shin, J.; Lim, T.-H.; Kim, G. Hybrid-Solid Oxide Electrolysis Cell: A New Strategy for Efficient Hydrogen Production. *Nano Energy* **2017**, *44* (July 2017), 121–126.
- (8) O’Hayre, R. P. Fuel Cell Fundamentals. **2006**, 409.
- (9) Jun, A.; Kim, J.; Shin, J.; Kim, G. Perovskite as a Cathode Material: A Review of Its Role in Solid-Oxide Fuel Cell Technology. *ChemElectroChem* **2016**, *3* (4), 511–530.
- (10) Kim, J.; Choi, S.; Jun, A.; Jeong, H. Y.; Shin, J.; Kim, G. Chemically Stable Perovskites as Cathode Materials for Solid Oxide Fuel Cells: La-Doped Ba_{0.5} Sr_{0.5} Co_{0.8} Fe_{0.2} O_{3-δ}. *ChemSusChem* **2014**, *7* (6), 1669–1675.
- (11) Jun, A.; Kim, J.; Shin, J.; Kim, G. Perovskite as a Cathode Material: A Review of Its Role in Solid-Oxide Fuel Cell Technology. *ChemElectroChem* **2016**, *3* (4), 511–530.
- (12) Kim, J.; Jun, A.; Shin, J.; Kim, G. Effect of Fe Doping on Layered GdBa_{0.5} Sr_{0.5} Co₂ O_{5+δ} Perovskite Cathodes for Intermediate Temperature Solid Oxide Fuel Cells. *J. Am. Ceram. Soc.* **2014**, *97* (2), 651–656.
- (13) Minh, N. Q. Ceramic Fuel Cells. *J. Am. Ceram. Soc.* **1993**, *76*, 563–588.
- (14) Skinner, S. J. Recent Advances in Perovskite-Type Materials for Solid Oxide Fuel Cell Cathodes. *Int. J. Inorg. Mater.* **2001**, *3* (2), 113–121.
- (15) Jacobson, A. J. Materials for Solid Oxide Fuel Cells. *Chem. Mater.* **2010**, *22* (3), 660–674.
- (16) Adler, S. B. Electrode Kinetics of Porous Mixed-Conducting Oxygen Electrodes. *J. Electrochem. Soc.* **1996**, *143* (11), 3554.
- (17) Dusastre, V.; Kilner, J. A. Optimisation of Composite Cathodes for Intermediate Temperature SOFC Applications. *Solid State Ionics* **1999**, *126*, 163–174.
- (18) Kim, J.-H.; Manthiram, a. LnBaCo[Sub 2]O[Sub 5+δ] Oxides as Cathodes for Intermediate-Temperature Solid Oxide Fuel Cells. *J. Electrochem. Soc.* **2008**, *155* (4), B385.
- (19) Kim, G.; Wang, S.; Jacobson, a. J.; Reimus, L.; Brodersen, P.; Mims, C. a. Rapid Oxygen Ion Diffusion and Surface Exchange Kinetics in PrBaCo₂O_{5+x} with a Perovskite Related Structure

- and Ordered A Cations. *J. Mater. Chem.* **2007**, *17* (24), 2500.
- (20) Taskin, a. a.; Lavrov, a. N.; Ando, Y. Achieving Fast Oxygen Diffusion in Perovskites by Cation Ordering. *Appl. Phys. Lett.* **2005**, *86* (9), 091910.
 - (21) Pissas, M.; Mitros, C.; Kallias, G.; Psycharis, V. Synthesis, Thermogravimetric and Fe Mossbauer Studies of Oxygen Deficient Perovskite REBaCuFeO_{5-d} Series. *physica c* **1992**, *192*, 35–40.
 - (22) Tarancón, A.; Skinner, S. J.; Chater, R. J.; Hernández-Ramírez, F.; Kilner, J. a. Layered Perovskites as Promising Cathodes for Intermediate Temperature Solid Oxide Fuel Cells. *J. Mater. Chem.* **2007**, *17* (30), 3175.
 - (23) Zhou, W.; Ran, R.; Shao, Z. Progress in Understanding and Development of Ba_{0.5}Sr_{0.5}Co_{0.8}Fe_{0.2}O_{3-δ}-Based Cathodes for Intermediate-Temperature Solid-Oxide Fuel Cells: A Review. *J. Power Sources* **2009**, *192* (2), 231–246.
 - (24) Kim, J. H.; Cassidy, M.; Irvine, J. T. S.; Bae, J. Advanced Electrochemical Properties of LnBa[Sub 0.5]Sr[Sub 0.5]Co[Sub 2]O[Sub 5+δ] (Ln=Pr, Sm, and Gd) as Cathode Materials for IT-SOFC. *J. Electrochem. Soc.* **2009**, *156* (6), B682.
 - (25) Park, S.; Choi, S.; Kim, J.; Shin, J.; Kim, G. Strontium Doping Effect on High-Performance PrBa_{1-x}Sr_xCo₂O_{5+δ} as a Cathode Material for IT-SOFCs. *ECS Electrochem. Lett.* **2012**, *1* (5), F29–F32.
 - (26) Jun, A.; Kim, J.; Shin, J.; Kim, G. Optimization of Sr Content in Layered SmBa_{1-x}Sr_xCo₂O_{5+δ} Perovskite Cathodes for Intermediate-Temperature Solid Oxide Fuel Cells. *Int. J. Hydrogen Energy* **2012**, *37* (23), 18381–18388.
 - (27) Kim, Y. N. Effect of Fe Substitution on the Structure and Properties of LnBaCo_{2-x}Fe_xO_{5+δ} (Ln=Nd and Gd) Cathodes. *J. Power Sources* **2010**, *195* (19), 6411–6419.
 - (28) Yoo, S.; Shin, J. Y.; Kim, G. Thermodynamic and Electrical Properties of Layered Perovskite NdBaCo_{2-x}Fe_xO_{5+δ}-YSZ (x=0, 1) Composites for Intermediate Temperature SOFC Cathodes. *J. Electrochem. Soc.* **2011**, *158* (6), B632.
 - (29) Choi, S.; Shin, J.; Kim, G. The Electrochemical and Thermodynamic Characterization of PrBaCo_{2-x}Fe_xO_{5+δ} (X=0, 0.5, 1) Infiltrated into Ytria-Stabilized Zirconia Scaffold as Cathodes for Solid Oxide Fuel Cells. *J. Power Sources* **2012**, *201*, 10–17.
 - (30) Andersson, M.; Yuan, J.; Sundén, B. Review on Modeling Development for Multiscale Chemical Reactions Coupled Transport Phenomena in Solid Oxide Fuel Cells. *Applied Energy*. 2010, pp 1461–1476.
 - (31) Nam, J. H.; Jeon, D. H. A Comprehensive Micro-Scale Model for Transport and Reaction in Intermediate Temperature Solid Oxide Fuel Cells. *Electrochim. Acta* **2006**, *51* (17), 3446–3460.
 - (32) Lee, K. T.; Manthiram, A. Effect of Cation Doping on the Physical Properties and Electrochemical Performance of Nd_{0.6}Sr_{0.4}Co_{0.8}M_{0.2}O_{3-??} (M = Ti, Cr, Mn, Fe, Co, and Cu) Cathodes. *Solid State Ionics* **2007**, *178* (13–14), 995–1000.
 - (33) Moritomo, Y.; Takeo, M.; Liu, X. J.; Akimoto, T.; Nakamura, A. Metal-Insulator Transition Due to Charge Ordering in R_{1/2}Ba_{1/2}CoO₃. *Phys. Rev. B* **1998**, *58* (20), 334–337.
 - (34) Chroneos, A.; Yildiz, B.; Tarancón, A.; Parfitt, D.; Kilner, J. a. Oxygen Diffusion in Solid Oxide Fuel Cell Cathode and Electrolyte Materials: Mechanistic Insights from Atomistic Simulations. *Energy Environ. Sci.* **2011**, *4* (8), 2774.
 - (35) Shao, Z.; Haile, S. M. A High-Performance Cathode for the next Generation of Solid-Oxide Fuel Cells. *Nature* **2004**, *431* (7005), 170–173.
 - (36) Zeng, P.; Chen, Z.; Zhou, W.; Gu, H.; Shao, Z.; Liu, S. Re-Evaluation of Ba_{0.5}Sr_{0.5}Co_{0.8}Fe_{0.2}O_{3-δ} Perovskite as Oxygen Semi-Permeable Membrane. *J. Memb. Sci.*

- 2007, 291 (1–2), 148–156.
- (37) Shao, Z. Investigation of the Permeation Behavior and Stability of a BSCF Oxygen Membrane. *J. Memb. Sci.* **2000**, 172, 177–188.
- (38) Efimov, K.; Xu, Q.; Feldhoff, A. Transmission Electron Microscopy Study of Ba_{0.5}Sr_{0.5}Co_{0.8}Fe_{0.2}O_{3-δ} Perovskite Decomposition at Intermediate Temperatures. *Chem. Mater.* **2010**, 22 (21), 5866–5875.
- (39) Arnold, M.; Gesing, T. M.; Martynczuk, J.; Feldhoff, A. Correlation of the Formation and the Decomposition Process of the BSCF Perovskite at Intermediate Temperatures. **2008**, No. 12, 5851–5858.
- (40) Svarcova, S.; Wiik, K.; Tolchard, J.; Bouwmeester, H. J. M.; Grande, T. Structural Instability of Cubic Perovskite Ba_xSr_{1-x}Co_{1-y}Fe_yO_{3-δ}. *Solid State Ionics* **2008**, 178 (35–36), 1787–1791.
- (41) Jung, J.-I.; Edwards, D. D. X-Ray Photoelectron (XPS) and Diffuse Reflectance Infra Fourier Transformation (DRIFT) Study of Ba_{0.5}Sr_{0.5}Co_xFe_{1-x}O_{3-δ} (BSCF: X=0–0.8) Ceramics. *J. Solid State Chem.* **2011**, 184 (8), 2238–2243.
- (42) Hayashi, H.; Inaba, H.; Matsuyama, M.; Lan, N. G.; Dokiya, M.; Tagawa, H. Structural Consideration on the Ionic Conductivity of Perovskite-Type Oxides. *Solid State Ionics* **1999**, 122, 1–15.
- (43) Yoo, S.; Choi, S.; Kim, J.; Shin, J.; Kim, G. Investigation of Layered Perovskite Type NdBa_{1-x}Sr_xXCo₂O_{5+δ} (x = 0, 0.25, 0.5, 0.75, and 1.0) Cathodes for Intermediate-Temperature Solid Oxide Fuel Cells. *Electrochim. Acta* **2013**, 100, 44–50.
- (44) Ovenstone, J.; Jung, J.-I.; White, J. S.; Edwards, D. D.; Mixture, S. T. Phase Stability of BSCF in Low Oxygen Partial Pressures. *J. Solid State Chem.* **2008**, 181 (3), 576–586.
- (45) Mcintosh, S.; Vente, J. F.; Haije, W. G.; Blank, D. H. A.; Bouwmeester, H. J. M. Oxygen Stoichiometry and Chemical Expansion of BSCF Measured by in Situ Neutron Diffraction. *Chem. Mater.* **2006**, No. 18, 2187–2193.
- (46) Kröger, F. A.; Vink, H. J. Relations between the Concentrations of Imperfections in Crystalline Solids. *solid state Phys.* **1956**, 3, 307–435.
- (47) Wei, B.; Lü, Z.; Li, S.; Liu, Y.; Liu, K.; Su, W. Thermal and Electrical Properties of New Cathode Material Ba_[Sub 0.5]Sr_[Sub 0.5]Co_[Sub 0.8]Fe_[Sub 0.2]O_[Sub 3-δ] for Solid Oxide Fuel Cells. *Electrochem. Solid-State Lett.* **2005**, 8 (8), A428.
- (48) Baumann, S.; Schulze-Küppers, F.; Roitsch, S.; Betz, M.; Zwick, M.; Pfaff, E. M.; Meulenber, W. a.; Mayer, J.; Stöver, D. Influence of Sintering Conditions on Microstructure and Oxygen Permeation of Ba_{0.5}Sr_{0.5}Co_{0.8}Fe_{0.2}O_{3-δ} (BSCF) Oxygen Transport Membranes. *J. Memb. Sci.* **2010**, 359 (1–2), 102–109.
- (49) Wu, Z.; Liu, M. Modelling of Ambipolar Transport Properties of Composite Mixed Ionic-Electronic Conductors. *Solid State Ionics* **1997**, 93, 65–84.
- (50) Yan, A.; Cheng, M.; Dong, Y.; Yang, W.; Maragou, V.; Song, S.; Tsiakaras, P. Investigation of a Ba_{0.5}Sr_{0.5}Co_{0.8}Fe_{0.2}O_{3-δ} Based Cathode IT-SOFC. *Appl. Catal. B Environ.* **2006**, 66 (1–2), 64–71.
- (51) ARNOLD, M.; WANG, H.; FELDHOF, A. Influence of CO₂ on the Oxygen Permeation Performance and the Microstructure of Perovskite-Type (Ba_{0.5}Sr_{0.5}) (Co_{0.8}Fe_{0.2})O_{3-δ} Membranes. *J. Memb. Sci.* **2007**, 293 (1–2), 44–52.
- (52) Niedrig, C.; Taufall, S.; Burriel, M.; Menesklu, W.; Wagner, S. F.; Baumann, S.; Ivers-Tiffée, E. Thermal Stability of the Cubic Phase in Ba_{0.5}Sr_{0.5}Co_{0.8}Fe_{0.2}O_{3-δ} (BSCF)1. *Solid State Ionics* **2011**, 197 (1), 25–31.
- (53) Wachsman, E. D.; Lee, K. T. Lowering the Temperature of Solid Oxide Fuel Cells. *Science*

- (80-). **2011**, 334 (6058), 935–939.
- (54) Steele, B. C. H.; Heinzl, A. Materials for Fuel-Cell Technologies. *Nature* **2001**, 414 (November), 345–352.
- (55) Chu, S.; Majumdar, A. Opportunities and Challenges for a Sustainable Energy Future. *Nature* **2012**, 488 (7411), 294–303.
- (56) Ding, D.; Li, X.; Lai, S. Y.; Gerdes, K.; Liu, M. Enhancing SOFC Cathode Performance by Surface Modification through Infiltration. *Energy Environ. Sci.* **2013**, 7, 552–575.
- (57) Iwahara, H. Proton Conducting Ceramics and Their Applications. *Solid State Ionics* **1996**, 86–88, 9–15.
- (58) Kreuer, K. Aspects of the Formation and Mobility of Protonic Charge Carriers and the Stability of Perovskite-Type Oxides. *Solid State Ionics* **1999**, 125 (1–4), 285–302.
- (59) Haile, S. M. Fuel Cell Materials and Components. *Acta Mater.* **2003**, 51 (19), 5981–6000.
- (60) Fabbri, E.; Pergolesi, D.; Traversa, E. Materials Challenges toward Proton-Conducting Oxide Fuel Cells: A Critical Review. *Chem. Soc. Rev.* **2010**, 39 (11), 4355.
- (61) Norby, T. The Promise of Protonics. *Nature* **2001**, 410 (6831), 877–878.
- (62) Uchida, H.; Tanaka, S.; Iwahara, H. Polarization at Pt Electrodes of a Fuel Cell with a High Temperature-Type Proton Conductive Solid Electrolyte. *J. Appl. Electrochem.* **1985**, 15, 93–97.
- (63) Malavasi, L.; Fisher, C. a J.; Islam, M. S. Oxide-Ion and Proton Conducting Electrolyte Materials for Clean Energy Applications: Structural and Mechanistic Features. *Chem. Soc. Rev.* **2010**, 39 (11), 4370–4387.
- (64) Phair, J. W.; Badwal, S. P. S. Review of Proton Conductors for Hydrogen Separation. *Ionics (Kiel)*. **2006**, 12 (2), 103–115.
- (65) Kreuer, K. D. Proton-Conducting Oxides. *Annu. Rev. Mater. Res.* **2003**, 33 (1), 333–359.
- (66) Serra, J. M.; Meulenberg, W. a. Thin-Film Proton BaZr_{0.85}Y_{0.15}O₃ Conducting Electrolytes: Toward an Intermediate-Temperature Solid Oxide Fuel Cell Alternative. *J. Am. Ceram. Soc.* **2007**, 90 (7), 2082–2089.
- (67) Norby, T. Solid-State Protonic Conductors: Principles, Properties, Progress and Prospects. *Solid State Ionics* **1999**, 125 (August 1998), 1–11.
- (68) Zuo, C.; Zha, S.; Liu, M.; Hatano, M.; Uchiyama, M. Ba(Zr_{0.1}Ce_{0.7}Y_{0.2})O_{3-δ} as an Electrolyte for Low-Temperature Solid-Oxide Fuel Cells. *Adv. Mater.* **2006**, 18 (24), 3318–3320.
- (69) Yang, L.; Wang, S.; Blinn, K.; Liu, M. M.; Liu, Z.; Cheng, Z.; Liu, M. M. Enhanced Sulfur and Coking Tolerance of a Mixed Ion Conductor for SOFCs: BaZr_(0.1)Ce_(0.7)Y_(0.2-x)Yb_(x)O_(3-Delta). *Science (80-)*. **2009**, 326 (5949), 126–129.
- (70) Ni, M. The Effect of Electrolyte Type on Performance of Solid Oxide Fuel Cells Running on Hydrocarbon Fuels. *Int. J. Hydrogen Energy* **2013**, 38 (6), 2846–2858.
- (71) Adler, S. B. Factors Governing Oxygen Reduction in Solid Oxide Fuel Cell Cathodes †. *Chem. Rev.* **2004**, 104 (10), 4791–4844.
- (72) Kim, J.; Seo, W.; Shin, J.; Liu, M.; Kim, G. Composite Cathodes Composed of NdBa_{0.5}Sr_{0.5}Co₂O_{5+δ} and Ce_{0.9}Gd_{0.1}O_{1.95} for Intermediate-Temperature Solid Oxide Fuel Cells. *J. Mater. Chem. A* **2013**, 1 (3), 515.
- (73) Fabbri, E.; Licoccia, S.; Traversa, E.; Wachsman, E. D. Composite Cathodes for Proton Conducting Electrolytes. *Fuel Cells* **2009**, 9 (2), 128–138.
- (74) Kim, J.-H.; Prado, F.; Manthiram, a. Characterization of GdBa_[Sub 1-x]Sr_[Sub x]Co_[Sub 2]O_[Sub 5+δ] (0≤x≤1.0) Double Perovskites as Cathodes for Solid Oxide Fuel Cells. *J. Electrochem. Soc.* **2008**, 155 (10), B1023.

- (75) Kim, G.; Wang, S.; Jacobson, A. J.; Reimus, L.; Brodersen, P.; Mims, C. a. Rapid Oxygen Ion Diffusion and Surface Exchange Kinetics in $\text{PrBaCo}_2\text{O}_{5+x}$ with a Perovskite Related Structure and Ordered A Cations. *J. Mater. Chem.* **2007**, *17* (24), 2500.
- (76) Choi, S.; Yoo, S.; Kim, J.; Park, S.; Jun, A.; Sengodan, S.; Kim, J.; Shin, J.; Jeong, H. Y.; Choi, Y.; et al. Highly Efficient and Robust Cathode Materials for Low-Temperature Solid Oxide Fuel Cells: $\text{PrBa}_{0.5}\text{Sr}_{0.5}\text{Co}_{2-x}\text{Fe}_x\text{O}_{5+\delta}$. *Sci. Rep.* **2013**, *3*, 2426.
- (77) Kim, J.; Jun, A.; Shin, J.; Kim, G. Effect of Fe Doping on Layered $\text{GdBa}_{0.5}\text{Sr}_{0.5}\text{Co}_{2-x}\text{O}_{5+\delta}$ Perovskite Cathodes for Intermediate Temperature Solid Oxide Fuel Cells. *J. Am. Ceram. Soc.* **2014**, *6*.
- (78) Jun, A.; Shin, J.; Kim, G. High Redox and Performance Stability of Layered $\text{SmBa}_{0.5}\text{Sr}_{0.5}\text{Co}_{1.5}\text{Cu}_{0.5}\text{O}_{5+d}$ Perovskite Cathodes for Intermediate-Temperature Solid Oxide Fuel Cells. *Phys. Chem. Chem. Phys.* **2013**.
- (79) Yoo, S.; Choi, S.; Kim, J.; Shin, J.; Kim, G. Investigation of Layered Perovskite Type $\text{NdBa}_{1-x}\text{Sr}_x\text{Co}_2\text{O}_{5+d}$ ($x = 0, 0.25, 0.5, 0.75, \text{ and } 1.0$) Cathodes for Intermediate-Temperature Solid Oxide Fuel Cells. *Electrochim. Acta* **2013**, *100*, 44–50.
- (80) Grimaud, A.; Mauvy, F.; Bassat, J. M.; Fourcade, S.; Rocheron, L.; Marrony, M.; Grenier, J. C. Hydration Properties and Rate Determining Steps of the Oxygen Reduction Reaction of Perovskite-Related Oxides as H^+ -SOFC Cathodes. *J. Electrochem. Soc.* **2012**, *159* (6), B683.
- (81) Jiang, S. P. Activation, Microstructure, and Polarization of Solid Oxide Fuel Cell Cathodes. *J. Solid State Electrochem.* **2005**, *11* (1), 93–102.
- (82) Ding, D.; Liu, M.; Liu, Z.; Li, X.; Blinn, K.; Zhu, X.; Liu, M. Efficient Electro-Catalysts for Enhancing Surface Activity and Stability of SOFC Cathodes. *Adv. Energy Mater.* **2013**, *3* (9), 1149–1154.
- (83) Zhu, B.; Liu, X.; Sun, M.; Ji, S.; Sun, J. Calcium Doped Ceria-Based Materials for Cost-Effective Intermediate Temperature Solid Oxide Fuel Cells. *Solid State Sci.* **2003**, *5* (8), 1127–1134.
- (84) Sun, W.; Liu, M.; Liu, W. Chemically Stable Yttrium and Tin Co-Doped Barium Zirconate Electrolyte for Next Generation High Performance Proton-Conducting Solid Oxide Fuel Cells. *Adv. Energy Mater.* **2013**.
- (85) Yang, L.; Zuo, C.; Wang, S.; Cheng, Z.; Liu, M. A Novel Composite Cathode for Low-Temperature SOFCs Based on Oxide Proton Conductors. *Adv. Mater.* **2008**, *20* (17), 3280–3283.
- (86) Fabbri, E.; Bi, L.; Tanaka, H.; Pergolesi, D.; Traversa, E. Chemically Stable Pr and Y Co-Doped Barium Zirconate Electrolytes with High Proton Conductivity for Intermediate-Temperature Solid Oxide Fuel Cells. *Adv. Funct. Mater.* **2011**, *21* (1), 158–166.
- (87) Bi, L.; Fabbri, E.; Sun, Z.; Traversa, E. A Novel Ionic Diffusion Strategy to Fabricate High-Performance Anode-Supported Solid Oxide Fuel Cells (SOFCs) with Proton-Conducting Y-Doped BaZrO_3 Films. *Energy Environ. Sci.* **2011**, *4* (2), 409.
- (88) Minh, N. Q. Reversible Solid Oxide Fuel Cell Technology for Hydrogen/Syngas and Power Production. In *Hydrogen Science and Engineering: Materials, Processes, Systems and Technology*; Prof. Dr. D. Stolten and Dr. B. Emonts, Ed.; Wiley-VCH Verlag GmbH & Co. KGaA: Weinheim, Germany, 2016; pp 359–390.
- (89) Han, L.; Dong, S.; Wang, E. Transition-Metal (Co, Ni, and Fe)-Based Electrocatalysts for the Water Oxidation Reaction. *Adv. Mater.* **2016**, *28* (42), 9266–9291.
- (90) Liu, W.; Cui, Y.; Du, X.; Zhang, Z.; Chao, Z.; Deng, Y. High Efficiency Hydrogen Evolution from Native Biomass Electrolysis. *Energy Environ. Sci.* **2016**, *9* (2), 467–472.
- (91) Yu, A. S.; Vohs, J. M.; Gorte, R. J. Interfacial Reactions in Ceramic Membrane Reactors for Syngas Production. *Energy Environ. Sci.* **2014**, *7* (3), 944.

- (92) Hauch, A.; Ebbesen, S. D.; Jensen, S. H.; Mogensen, M. Highly Efficient High Temperature Electrolysis. *J. Mater. Chem.* **2008**, *18* (20), 2331–2340.
- (93) Chen, L.; Chen, F.; Xia, C. Direct Synthesis of Methane from CO₂–H₂O Co-Electrolysis in Tubular Solid Oxide Electrolysis Cells. *Energy Environ. Sci.* **2014**, *7* (12), 4018–4022.
- (94) Laguna-Bercero, M. A. Recent Advances in High Temperature Electrolysis Using Solid Oxide Fuel Cells: A Review. *J. Power Sources* **2012**, *203*, 4–16.
- (95) Zhou, W.; Shi, H.; Ran, R.; Cai, R.; Shao, Z.; Jin, W. Fabrication of an Anode-Supported Ytria-Stabilized Zirconia Thin Film for Solid-Oxide Fuel Cells via Wet Powder Spraying. *J. Power Sources* **2008**, *184* (1), 229–237.
- (96) Lin, Y.; Fang, S.; Su, D.; Brinkman, K. S.; Chen, F. Enhancing Grain Boundary Ionic Conductivity in Mixed Ionic-Electronic Conductors. *Nat. Commun.* **2015**, *6*, 6824.
- (97) Sengodan, S.; Choi, S.; Jun, A.; Shin, T. H.; Ju, Y.-W.; Jeong, H. Y.; Shin, J.; Irvine, J. T. S.; Kim, G. Layered Oxygen-Deficient Double Perovskite as an Efficient and Stable Anode for Direct Hydrocarbon Solid Oxide Fuel Cells. *Nat. Mater.* **2014**, *14* (2), 205–209.
- (98) Jun, A.; Kim, J.; Shin, J.; Kim, G. Achieving High Efficiency and Eliminating Degradation in Solid Oxide Electrochemical Cells Using High Oxygen-Capacity Perovskite. *Angew. Chemie Int. Ed.* **2016**, 1–5.
- (99) Bi, L.; Boulfrad, S.; Traversa, E. Steam Electrolysis by Solid Oxide Electrolysis Cells (SOECs) with Proton-Conducting Oxides. *Chem. Soc. Rev.* **2014**, *43* (24), 8255–8270.
- (100) Kreuer, K. D. Proton-Conducting Oxides. *Annu. Rev. Mater. Res.* **2003**, *33* (1), 333–359.
- (101) Yang, L.; Wang, S.; Blinn, K.; Liu, M.; Liu, Z.; Cheng, Z.; Liu, M. Enhanced Sulfur and Coking Tolerance of a Mixed Ion Conductor for SOFCs: BaZr_{0.1}Ce_{0.7}Y_{0.2}XYb_xO_{3-δ}. *Science* (80-.). **2009**, *326* (5949), 126–129.
- (102) Nechache, A.; Cassir, M.; Ringuedé, A. Solid Oxide Electrolysis Cell Analysis by Means of Electrochemical Impedance Spectroscopy: A Review. *J. Power Sources* **2014**, *258*, 164–181.
- (103) Rossignol, C.; Ralph, J. M.; Bae, J. M.; Vaughey, J. T. Ln_{1-x}Sr_xCoO₃ (Ln=Gd, Pr) as a Cathode for Intermediate-Temperature Solid Oxide Fuel Cells. *Solid State Ionics* **2004**, *175* (1–4), 59–61.
- (104) Jun, A.; Yoo, S.; Ju, Y.-W.; Hyodo, J.; Choi, S.; Jeong, H. Y.; Shin, J.; Ishihara, T.; Lim, T.; Kim, G. Correlation between Fast Oxygen Kinetics and Enhanced Performance in Fe Doped Layered Perovskite Cathodes for Solid Oxide Fuel Cells. *J. Mater. Chem. A* **2015**, *3*, 15082–15090.
- (105) Bi, L.; Shafi, S. P.; Traversa, E. Y-Doped BaZrO₃ as a Chemically Stable Electrolyte for Proton-Conducting Solid Oxide Electrolysis Cells (SOECs). *J. Mater. Chem. A* **2015**, *3* (11), 5815–5819.
- (106) Chen, T.; Liu, M.; Yuan, C.; Zhou, Y.; Ye, X.; Zhan, Z.; Xia, C.; Wang, S. High Performance of Intermediate Temperature Solid Oxide Electrolysis Cells Using Nd₂NiO_{4+δ} Impregnated Scandia Stabilized Zirconia Oxygen Electrode. *J. Power Sources* **2015**, *276*, 1–6.
- (107) Gan, Y.; Zhang, J.; Li, Y.; Li, S.; Xie, K.; Irvine, J. T. S. Composite Oxygen Electrode Based on LSCM for Steam Electrolysis in a Proton Conducting Solid Oxide Electrolyzer. *J. Electrochem. Soc.* **2012**, *159* (11), F763–F767.
- (108) He, F.; Song, D.; Peng, R.; Meng, G.; Yang, S. Electrode Performance and Analysis of Reversible Solid Oxide Fuel Cells with Proton Conducting Electrolyte of BaCe_{0.5}Zr_{0.3}Y_{0.2}O_{3-δ}. *J. Power Sources* **2010**, *195* (11), 3359–3364.
- (109) Bidrawn, F.; Kim, G.; Corre, G.; Irvine, J. T. S.; Vohs, J. M.; Gorte, R. J. Efficient Reduction of CO[Sub 2] in a Solid Oxide Electrolyzer. *Electrochem. Solid-State Lett.* **2008**, *11* (9), B167.

- (110) Carmo, M.; Fritz, D. L.; Mergel, J.; Stolten, D. A Comprehensive Review on PEM Water Electrolysis. *Int. J. Hydrogen Energy* **2013**, *38* (12), 4901–4934.
- (111) Callejas, J. F.; Read, C. G.; Popczun, E. J.; McEnaney, J. M.; Schaak, R. E. Nanostructured Co₂P Electrocatalyst for the Hydrogen Evolution Reaction and Direct Comparison with Morphologically Equivalent CoP. *Chem. Mater.* **2015**, *27* (10), 3769–3774.
- (112) Wang, T.; Zhuo, J.; Du, K.; Chen, B.; Zhu, Z.; Shao, Y.; Li, M. Electrochemically Fabricated Polypyrrole and MoS_x Copolymer Films as a Highly Active Hydrogen Evolution Electrocatalyst. *Adv. Mater.* **2014**, *26* (22), 3761–3766.
- (113) Kibsgaard, J.; Jaramillo, T. F. Molybdenum Phosphosulfide: An Active, Acid-Stable, Earth-Abundant Catalyst for the Hydrogen Evolution Reaction. *Angew. Chemie Int. Ed.* **2014**, *53* (52), 14433–14437.
- (114) Li, Y.; Wang, H.; Xie, L.; Liang, Y.; Hong, G.; Dai, H. MoS₂ Nanoparticles Grown on Graphene: An Advanced Catalyst for the Hydrogen Evolution Reaction. *J. Am. Chem. Soc.* **2011**, *133* (19), 7296–7299.
- (115) Burriel, M.; Peña-Martínez, J.; Chater, R. J.; Fearn, S.; Berenov, A. V.; Skinner, S. J.; Kilner, J. a. Anisotropic Oxygen Ion Diffusion in Layered PrBaCo₂O_{5+δ}. *Chem. Mater.* **2012**, *24* (3), 613–621.
- (116) Norby, T. Solid-State Protonic Conductors: Principles, Properties, Progress and Prospects. *Solid State Ionics* **1999**, *125* (August 1998), 1–11.
- (117) Vert, V. B.; Serra, J. M.; Kilner, J. A.; Burriel, M. Enhanced Oxygen Diffusion in Low Barium-Containing La_{0.2175}Pr_{0.2175}Ba_{0.145}Sr_{0.4}Fe_{0.8}Co_{0.2}O_{3-δ} Intermediate Temperature Solid Oxide Fuel Cell Cathodes. *J. Power Sources* **2012**, *213*, 270–274.
- (118) Hancke, R.; Fearn, S.; Kilner, J. a.; Haugsrud, R. Determination of Proton- and Oxide Ion Tracer Diffusion in Lanthanum Tungstate (La/W = 5.6) by Means of ToF-SIMS. *Phys. Chem. Chem. Phys.* **2012**, *14*, 13971.
- (119) Berenov, A. V.; Atkinson, A.; Kilner, J. A.; Bucher, E.; Sitte, W. Oxygen Tracer Diffusion and Surface Exchange Kinetics in La_{0.6}Sr_{0.4}CoO_{3-δ}. *Solid State Ionics* **2010**, *181* (17–18), 819–826.
- (120) Leonide, A.; Rüger, B.; Weber, A.; Meulenberg, W. A.; Ivers-Tiffée, E. Impedance Study of Alternative (La,Sr)FeO_[Sub 3-δ] and (La,Sr)(Co,Fe)O_[Sub 3-δ] MIEC Cathode Compositions. *J. Electrochem. Soc.* **2010**, *157* (2), B234.
- (121) Kreuer, K. D.; Adams, S.; Münch, W.; Fuchs, A.; Klock, U.; Maier, J. Proton Conducting Alkaline Earth Zirconates and Titanates for High Drain Electrochemical Applications. *Solid State Ionics* **2001**, *145* (1–4), 295–306.
- (122) Haugsrud, R.; Norby, T. Proton Conduction in Rare-Earth Ortho-Niobates and Ortho-Tantalates. *Nat. Mater.* **2006**, *5* (3), 193–196.
- (123) Yamazaki, Y.; Babilo, P.; Haile, S. M. Defect Chemistry of Yttrium-Doped Barium Zirconate : A Thermodynamic Analysis of Water Uptake. *Chem. Mater.* **2008**, *125* (2), 6352–6357.
- (124) Kreuer, K. D.; Dippel, T.; Baikov, Y. M.; Maier, J. Water Solubility, Proton and Oxygen Diffusion in Acceptor Doped BaCeO₃: A Single Crystal Analysis. *Solid State Ionics* **1996**, *86–88* (PART 1), 613–620.
- (125) Weber, A.; Ivers-Tiffée, E. Materials and Concepts for Solid Oxide Fuel Cells (SOFCs) in Stationary and Mobile Applications. *J. Power Sources* **2004**, *127* (1–2), 273–283.